

NORTHWESTERN UNIVERSITY

Electrostatic Interactions in Self-assembly Systems

A DISSERTATION

SUBMITTED TO THE GRADUATE SCHOOL  
IN PARTIAL FULFILLMENT OF THE REQUIREMENTS

for the degree

DOCTOR OF PHILOSOPHY

Field of Applied Physics

By

Honghao Li

EVANSTON, ILLINOIS

September 2018

© Copyright by Honghao Li 2018

All Rights Reserved

## ABSTRACT

Electrostatic Interactions in Self-assembly Systems

Honghao Li

Many phenomena that occur in the nanoscale, such as the self-assembly of charged amphiphiles, the metal extraction for recovering rare earth elements and nuclear waste as well as water purification, are driven by the electrostatic forces. Although current simulation techniques can handle the long-range Coulomb potential efficiently, the inhomogeneity in materials of such systems often gives rise to significant polarization charges that have to be determined by solving the non-trivial Poissons equation at each time step of molecular simulation. Thus, dielectric effects are often ignored in previous simulation studies despite their potential importance. Meanwhile, molecules can dynamically change their charges (dissociation state) according to the environment around. Current molecular simulation framework is unable to handle this efficiently. This dissertation presents various techniques that can resolve the simulation challenges in charged systems and applies them to uncover the significance of electrostatic interactions in those systems.

We first present the mathematical formulations for the variational approach that solves the polarization in dielectric heterogeneous systems. We use this method to compute

the surface polarization of ion-containing droplets. For water droplets immersed in oil, the interdroplet interaction is attractive, and the surface polarization makes the major contribution. By contrast, for oil droplets in water, the ion-surface induced charge interaction is repulsive and counteracts the attraction between the ions, leading to a small attractive interaction between the droplets. This research improves our understanding of self-assembly in mixed phases such as metal extraction for recovering rare earth elements and nuclear waste as well as water purification. Then we consider asymmetric 2:1 and 3:1 electrolyte bounded by a sinusoidally deformed solid surface. We demonstrate that even when the surface is neutral, the electrolyte acquires a non-uniform ion density profile near the surface. The profile is asymmetric and leads to the effective charging of the surface. We furthermore show that the charge is modulated by the local curvature. The effective charge is opposite to that of the multivalent ion and is negative at concave regions of the surface. The ion distribution could be altered if there are charged molecules at the interface.

Later, we develop the Monte-Carlo method that self-consistently solves the dynamical dissociation state of amphiphile molecules. Together with a theoretical model, we find that electrostatic effects arising from the inhomogeneity of the interfacial medium are responsible for this strong selectivity between two chemically similar lanthanide ions. Our results show that the interface plays an essential role in separating lanthanides during solvent extraction. We also use the Monte-Carlo simulations and pH titration measurements reveal that ionic correlations in the peptide amphiphile (PA) assemblies shift the ionizable amine  $pK \sim 8$  from  $pK \sim 10$  in the lysine headgroup. Our studies correlate the molecular charge and the morphology for a pH-responsive PA system and provide insights into the

Å-scale molecular packing in such assemblies. In another project, we use simplified theoretical models based on the interplay between electrostatic, bending, van-der Waals and surface energies qualitatively reproduce the experimental observations of the increase in bilayer aspect ratio, membrane rolling and the changes in the inter-bilayer spacing as a function of NaCl concentration. We find the narrow ribbon to sheet transition is a first order phase transition. Overall, our studies correlate electrostatic interaction with the morphological changes of the membrane, and provide a means for attaining and controlling the cochleate morphology. In particular, we speculate that the tunable inter-bilayer spacing can be used for controlled encapsulation and release of macromolecules of different sizes for drug-delivery applications.

Last, we further extend our studies to the ion dynamics in charged system. Transport of ionic species in heterogeneous polymeric media is highly dependent on the charge distributions and interactions between mobile and immobile groups. Here we perform coarse-grained molecular dynamics simulations to study the ion dynamics in swollen polyelectrolyte gels under external electric fields. A nonlinear response of the ionic conductivity to an applied electric field, for field strengths that are comparable to the ionic coupling strength, is observed. This behavior correlates to a broadening of the ionic distribution around the polymer backbone under an increasing electric field. Also, we find that the weak-field ionic mobility in gels increases with density, which is opposite to the behavior of simple electrolytes. This relates to the mean coupling between charges that decreases in gels, but increases in simple electrolytes, with increasing density. These results provide more insights into the electric response of polyelectrolyte gels to support the development

of applications that combine electric and mechanical properties of polyelectrolyte gels for energy storage, sensing, selective transport, and signal transfer.

## Acknowledgements

The Ph.D. life has been challenging yet rewarding. I feel so grateful to those people who have mentored me, helped me and supported me during the past five years.

First and foremost, I would like to express my sincere gratitude to my advisor Prof. Monica Olvera de la Cruz for the continuous support of my Ph.D study. Her guidance, together with her intellectual curiosity and visionary perspective, helped me a lot during my research. Inspired by her immense knowledge and passion for science, I was encouraged to explore my own interests in diverse research projects. She has a deep insight in physics and a great taste for important problems. I could not have imagined having a better advisor and mentor.

Besides my advisor, I would like to thank the rest of my thesis committee, Prof. Michael J. Bedzyk and Prof. Pulak Dutta, for their insightful comments and encouragement. The advices they offered at my thesis proposal and later meetings are essential for me to improve this research. I also had the chance to collaborate with both of them on several projects. Those were great experiences and I learned so much from them.

During my PhD studies, I feel truly blessed to work with all the brilliant Olvera group members. I would like to thank Prof. Jos Zwanikken and Dr. Aykut Erbas for mentoring me in the first few years. Jos is a very knowledgeable theorist yet a humble and patient person with great compassion. Aykut is a great tutor as well as a good friend. I also thank Dr. Yufei Jing for introducing me into the dielectric project, through which I found

my talent and passion in programming, and it eventually led me to the new endeavor in my life. Additionally, I would like to thank my collaborators Dr. Trung D. Nguyen and Dr. Meng Shen. Trung is an excellent programmer and is very experienced in molecular dynamics. I learned a lot from the wonderful experience when we implemented our method into LAMMPS. Meng is an ambitious scientist with deep love in physics. I thank her for those daily discussion either about research or about life. Also, I thank Changrui Gao and Sumit Kewalramani for several interesting and challenging collaborating projects. Thank Prof. Francisco Solis for valuable discussions on the variational method. Thank Dr. Baofu Qiao and Dongxu Huang for helping me learning full-atom simulations. Last, I feel really grateful to have so many wonderful group member around, they make my daily life delightful.

Finally, I would like to thank my family and my friends for supporting me spiritually throughout the Ph.D. life. I feel very fortunate to have their endless love and understanding.

## Table of Contents

ABSTRACT	3
Acknowledgements	7
Table of Contents	9
List of Tables	12
List of Figures	13
Chapter 1. Introduction	24
Chapter 2. Method	28
2.1. Variational approach for dielectric response	28
2.2. General functional for multiple interfaces	30
2.3. Numerical Implementation	32
Chapter 3. Surface Polarization Effects on Ion-Containing Emulsions	49
Abstract	49
3.1. Introduction	50
3.2. Model	52
3.3. Results and Discussion	54
3.4. Conclusion	60

	10
3.5. Appendix	60
Chapter 4. Asymmetric Electrolytes Near Structured Dielectric Interfaces	64
Abstract	64
4.1. Introduction	65
4.2. Asymmetric 2:1 electrolytes near solid neutral interface	67
4.3. Asymmetric 3:1 electrolytes near neutral/charged interface	76
4.4. Conclusion	83
Chapter 5. Interfacial origin of intra-lanthanide selectivity during solvent extraction	85
Abstract	85
5.1. Introduction	86
5.2. Results and Discussion	88
5.3. Conclusions	98
5.4. Appendix: Simulation Parameters	99
Chapter 6. Electrostatic Control of Polymorphism in Charged Amphiphile Assemblies	100
6.1. Introduction	100
6.2. Polymorphism of peptide amphiphile assembly induced by headgroup charge and size regulation	104
6.3. Electrostatic control of nanoribbon-to-cochleate transition in a charged peptide amphiphile assembly	111
6.4. Appendix: Theoretical models for ribbon-to-cochleate transition	121
Chapter 7. Ion dynamics in polyelectrolyte gels	128

	11
Abstract	128
7.1. Introduction	129
7.2. Model	130
7.3. Results and Discussion	134
7.4. Conclusion	147
Chapter 8. Summary and Outlook	149
8.1. Summary	149
8.2. Ongoing project: Comparison of different polarization solvers	152
8.3. Promising project: Ion dynamics in dielectric media	153
References	157

## List of Tables

3.1	Four cases with different permittivity contrast.	51
6.1	Numerical values for the membrane model parameters in (6.21) and (6.22).	124
6.2	Numerical values for the membrane model parameters in Eq. 6.20 and 6.21.	126
6.3	Numerical values for the membrane model parameters in (6.6) and (6.8).	126

## List of Figures

- 3.1 Ion-ion (blue circles, fit in blue dotted lines), ion-induced charge (red triangles, fit in red dashed lines) and total (black squares, fit in solid black lines) inter-droplet interactions as a function of inter-droplet distance (a) between water droplets immersed in oil and (b) between oil droplets immersed in water. Inter-droplet interaction with uniform water permittivity (green crosses and fit in green solid lines in (a)) and with uniform oil permittivity (green pluses and fit in solid lines in (b)). Insets are snapshots of the simulations. Red means positive charges, and blue means negative charges. 54
- 3.2 (a) the average magnitude of dipole moment, (b) the orientation factor between dipoles and (c) the distance between the center of dipoles formed by ions in each droplet for water droplets in oil (black squares), oil droplets in water (red circles), uniform water permittivity (blue triangles) and uniform oil permittivity (green diamonds). Color online. 58
- 3.3 Ion-ion (blue circles, fit in blue dotted lines), ion-induced charge (red triangles, fit in red dashed lines) and total (black squares, fit in solid black lines) inter-droplet interactions as a function of inter-droplet distance between the water droplets immersed in oil (a) for ion diameters

of 0.2 nm and (b) for cation diameters of 0.5 nm and anion diameters of 0.3 nm.

62

3.4 Ion-ion (blue circles, fit in blue dotted lines), ion-surface induced charge (red triangles, fit in red dashed lines) and total (black squares, fit in solid black lines) inter-droplet interactions as a function of inter-droplet distance for (a) monovalent ions in the water droplets immersed in oil, (b) monovalent ions in the oil droplets immersed in water, (c) trivalent ions in the water droplets immersed in oil, and (d) trivalent ions in the oil droplets immersed in water for ion diameters of 0.4 nm.

63

4.1 Primitive model of an asymmetric electrolyte near a neutral sinusoidal dielectric interface. The positive divalent (red) ions the negative monovalent (blue) ions are immersed in continuum water with relative permittivity  $\epsilon_m = 80$ . The medium below the interface has relative permittivity  $\epsilon_s = 2$ . Apart from the polarization charges, the ions also interact with the surface via the shifted-truncated Lenard-Jones potential.

68

4.2 Density distributions of a 50 mM 2:1 electrolyte above a structured interface. Left: (a) Divalent and (b) monovalent ion density distributions for a surface *without* dielectric mismatch. Right: (c) Divalent and (d) monovalent ion density distributions for a surface *with* permittivity mismatch 80/2. The polarization charges significantly enhance the surface depletion, in particular for the divalent ions.

72

- 4.3 Net ionic charge distribution formed by 50 mM 2:1 electrolyte above a neutral structured interface with (a) permittivity mismatch 80/2 and (b) no dielectric mismatch. The net ionic charge density is significantly enhanced by dielectric effects. In addition, the lateral position above the surface also affects the net charge density, as confirmed in panels (c) and (d), with and without permittivity mismatch, respectively. The magnitude of the net charge density is largest above the concave regions (troughs) of the surface. The bin width is  $0.5\sigma$  along the  $x$  direction and  $dz = 0.02\sigma$  in the  $z$  direction. Panels (c) and (d) were obtained using simulations based upon the variational approach of Ref[1]. 74
- 4.4 (a) Time-averaged surface polarization charge density induced by the spatially modulated ion distribution. (b) Surface polarization charge profile for various amplitudes of the profile. 75
- 4.5 Induced surface charge density at a structured dielectric interface that is modulated along both the  $x$  and  $y$  directions. As in the sinusoidal case [Fig. 4.4(a)], the dielectric mismatch is 80/2 with a 50 mM 2:1 electrolyte placed above the surface. 76
- 4.6 The sketch of the studied system. (a) A sinusoidal interface between two different dielectric constants regions ( $\epsilon_1 = 80$  and  $\epsilon_2 = 2$ ). Ions are all in the 1st region. When they approach the interface, the interface will have induced charge thus affect the ions distribution. (b) Another layer of amphiphile molecules are considered. They can move freely along the interface and some of them are negative charged. 77

4.7 (a) A single positive charge is placed  $1\sigma$  above the convex/concave point, the induced charge density along x direction is plotted. When the charge is placed above the concave point, the induced charge has higher peak, wider shape, and a compensated negative value at convex region. (b) When two layers of uniform charges ( $10 \times 10$  point ions each layer) are placed above the interface with negative layer closer and positive layer further away. (c) the polarization charge is negative at concave region while positive at convex region.

78

4.8 Ion distribution. (a) Charge density of positive ions. The interface is denoted by black color, the dashed line represents the closest distance an ion can reach due to the hard-core LJ potential. (b) Charge density of positive ions in the narrow bin (width  $dx = 0.5\sigma$ ) above the convex/concave region. (c) Charge density of positive ions in the narrow bin (width  $dx = 0.5\sigma$ ) above the convex/concave region (system without dielectric mismatch). (a) Charge density of negative ions. (b) Charge density of negative ions in the narrow bin (width  $dx = 0.5\sigma$ ) above the convex/concave region. (c) Charge density of negative ions in the narrow bin (width  $dx = 0.5\sigma$ ) above the convex/concave region (system without dielectric mismatch). To summarize, (a), (b), (d) and (e) are for system with dielectric mismatch while (c) and (f) are for system without dielectric mismatch.

80

4.9 Net charge density. (a) Net charge density. (b) Net charge density in the narrow bin (width  $dx = 0.5\sigma$ ) above the convex/concave region. (c) Net

- charge density in system without dielectric mismatch. (d) Net charge density in the narrow bin (width  $dx = 0.5\sigma$ ) above the convex/concave region (system without dielectric mismatch). 81
- 4.10 Induced charge density on the interface when the dielectric mismatch is present. 82
- 4.11 Charge density of positive ions in the narrow region above the convex/concave region when the molecular layer is present. (a) None of the 70 molecules is charged. (b) 1 out of 70 molecules is negative charged. (c) 3 out of 70 molecules are negative charged. (d) 5 out of 70 molecules are negative charged. 83
- 4.12 Charge distribution for planar case with molecular layer. 84
- 5.1 Surface density of Er (red error bars) vs. bulk concentration in the aqueous phase. The line connects theoretically calculated values (blue dots) using simulation parameters:  $l_B^+ = 1.769l_B^{water}$ ,  $l_B^- = 1.963l_B^{water}$ , with interlayer distance  $d = \sigma = 0.5nm$ . See Simulations and Theory Results section for an explanation of these variables, and other details. 89
- 5.2 Surface density of Nd (red error bars) vs. bulk concentration in the aqueous phase. The line connects theoretically calculated values (blue dots) using simulation parameters:  $l_B^+ = 1.769l_B^{water}$ ,  $l_B^- = 1.963l_B^{water}$ , with interlayer distance  $d = 1.07\sigma = 0.535nm$ . See Simulations and Theory Results section for an explanation of these variables, and other details. 90

- 5.3 Surface densities of  $\text{Er}^{3+}$  and  $\text{Nd}^{3+}$  when the bulk Er concentration is varied (Nd concentration fixed at  $10^{-4}\text{M}$ ). The lines are guides to eye. 91
- 5.4 (a) Schematic diagram of the system being simulated. (b) Sample Monte-Carlo simulation setup (smaller system  $20 \times 20$  here for clarity), upper(lower) hexagonal lattice layer is molecules(lanthanides), red is charged molecules, blue is absorbed lanthanides; white is neutral molecules or empty sites of lanthanides. The separation in the z direction is exaggerated here for clarity. 93
- 6.1 Molecular structures of positively charged  $C_{16}K_4$ ,  $C_{16}K_3$ ,  $C_{16}K_2$ , and  $C_{16}K_1$  peptide amphiphiles. 104
- 6.2 Phase diagram showing the formation and transition of self-assembly morphology of  $C_{16}K_n$  peptide amphiphile as a function of headgroup size and pH. 105
- 6.3 Phase diagram showing the formation and transition of self-assembly morphology (the headgroup charge) of  $C_{16}K_2$  peptide amphiphile as a function pH. 106
- 6.4 (a) Molecular structure of +2 charged  $C_{16}K_2$  peptide with estimates for the hydrophobic tail length and hydrophilic headgroup length and width. (b) Averaged  $C_{16}K_2$  headgroup charge as a function of pH in standard water environment obtained by Monte Carlo simulation, showing deprotonation around pH 8.2. (c)  $C_{16}K_2$  titration curve showing how pH changes as a function of the volume of NaOH added.

For comparison, calculated titration curves based on a monoprotic acid with  $\text{pKa} = 8.2$  (red, dashed) and Monte Carlo simulations (green) are shown.

- 108
- 6.5 (a)  $C_{16}K_n$  titration curves showing how pH changes as function of the volume of NaOH added. All  $C_{16}K_n$  exhibit single buffer stage. (b) Averaged  $C_{16}K_n$  headgroup charge as a function of pH obtained through Henderson-Hasselbach equation of monoprotic acid (6.1).  $\text{pKa}$  is determined from the titration curves. 109
- 6.6 (a-d) AFM peakforce error images for  $C_{16}K_1$  membranes at Si/NaCl solution interfaces. As the NaCl concentration increases, nanoribbon to isotropic sheet and to rolled-up cochleate transformations are observed. (e-h) Cryogenic TEM images of cochleates exhibit scroll morphology and the internal multilayer features. It can be readily seen that the interbilayer spacing  $D$  within the cochleate structure decreases with increasing NaCl concentration. 112
- 6.7 (upper) Illustration of nanoribbon-to-cochleate transition. (bottom) Interlayer distance decreases with increasing salt concentration. 113
- 6.8 (a) Schematic representation of  $C_{16}K_1$  nanoribbon showing ribbon dimensions used for the energy calculation. (b) The membrane energy per unit area in equation (1) as a function of the inverse of membrane aspect ratio  $W/L$ . At low salt concentration, the minimum of the membrane energy indicates that elongated ribbon structure is the equilibrium morphology. As salt concentration increases, the membrane

energy starts to decrease monotonically with  $W/L$  and drives the membrane to form low aspect ratio morphology. 114

6.9 (a) Total energy per charged molecule vs. aspect ratio with total area of membrane being constant. At small Debye length (high salt concentration), membrane favors to be sheets (aspect ratio = 1); at large Debye length (low salt concentration), membrane favors to be narrow ribbons (small aspect ratio). (b) The equilibrium aspect ratio (minimum energy state) for different Debye length. It is a first order transition. (Inset) The energy difference between the equilibrium aspect ratio and the sheets (aspect ratio = 1). There energy difference near the transition point is much smaller than  $1k_B T$ . 116

6.10 (a) An array of charged species with array length  $L_0$  and spontaneous curve  $C_0$ . This model is used to calculate the sum of electrostatic and curvature energy as a function of salt concentration and curvature. (b) Total energy per unit length (6.5) versus array curvature  $C_1$  at different salt concentrations ( $3 > 2 > 1 > \text{No salt}$ ). 117

6.11 (a) The geometry of the lamellar stack. The thicknesses of membrane and interbilayer aqueous regions are  $\delta$  and  $d$ , respectively. (b) Theoretical prediction showing linear correlation between interbilayer spacing  $D$  and  $c^{-1/2}$ , where  $c$  is NaCl concentration with unit of mol/L. The deviation relative to experimental result is likely due to the assumption of planar stack rather than spiral geometry in the theoretical model. 119

- 7.1 (a) Snapshot depicting a  $N = 100$  polyelectrolyte network structure. Monomers and counterions are denoted by cyan and purple spheres respectively. Every cross-linking node (drawn as oversized red spheres for illustration purpose) is attached by six polyelectrolyte chains, each of which has  $N$  monomers. Unit cell box in simulation typically has  $4 \times 4 \times 4$  cross-linking nodes ( $2 \times 2 \times 2$  shown here). (b) Illustration of the cell parameter that is used to determine condensed ion distributions. The distance from chain  $d$  is defined by the distance between an ion and its nearest monomer. The ion is considered as condensed ion when  $d \leq 2\sigma$ . 131
- 7.2 (a) Average end-to-end distance  $R_e$  of polyelectrolyte chains exhibit a linear scaling with  $N$  for both  $l_B = 1\sigma$  (empty square) and  $5\sigma$  (solid sphere). Due to the stronger electrostatic interaction,  $l_B = 5\sigma$  has a smaller  $R_e$  than its  $l_B = 1\sigma$  equivalence. A linear reference line is shown to guide the eye. (b) Fraction of condensed counterions  $f_{CI}$  at zero external electric field, all ions within a distance of  $2\sigma$  around the backbone chains are summed up. As  $N \rightarrow \infty$ , the counterion condensation ratio approaches the Manning theory (dashed line). 135
- 7.3 Comparison of linear-response mobilities  $\mu$  and equilibrium diffusivities  $D$  of counterions in gels and 1:1 simple electrolytes for an electrostatic strength of  $l_B = 5\sigma$ . The diffusion coefficients are calculated via mean square displacement of counterions (MSD) in Eq. 7.2 at zero field, whereas the mobilities are calculated via Eq. 7.1 at  $E = 0.1\epsilon/q\sigma$ . For

comparison, polymerization degree  $N$  and monomer concentration  $c$  are related by using  $c \equiv N/R_e^3$  for gels and shown as an alternative x-axis (top axis). 137

7.4 Mobility of counterions for various gels under external electric fields for both  $l_B = 1\sigma$  and  $l_B = 5\sigma$ . All the mobility values are rescaled by the Langevin damping parameter  $\mu_0 = 1/\gamma$ . Arrow indicates the value of the electric field ( $E = 0.1\epsilon/q\sigma$ ) that is used in Figure 7.3. Notice that this field is within the linear-response regime 138

7.5 (a) Integrated ion distributions for various polyelectrolyte networks. The distance from chain  $d$  is normalized by the end-to-end distance  $R_e$ . Inset shows mobility of ions as a function of their distance from chains at  $E = 0.1\epsilon/q\sigma$  with  $l_B = 5\sigma$ . (b) The calculated electrostatic potentials for counterions as a function of the distance. Inset shows average Coulomb energy per counterion in various gels and 1:1 binary electrolytes at identical ionic concentrations at  $E = 0.1\epsilon/q\sigma$ . 141

7.6 Integrated ion distribution around the chains of  $N = 100$  polyelectrolyte networks for various external electric fields (a)  $l_B = 1\sigma$  and (b)  $l_B = 5\sigma$ . The distance is normalized by the end-to-end distance  $R_e$ . Insets show mobility and number of free ions on a single plot. Blue squares denote the mobility values respect to left y axis, while red dots denote the fraction of free ions respect to right y axis. (c) 2D plots of counterions-concentration profiles are shown for  $E = 0.1\epsilon/q\sigma$  (left) and  $E = 1\epsilon/q\sigma$  (right), external field is in z-direction. The red regions refer

to high local concentration of counterions around the network chains,  
 whereas blue color refers to the low local concentration. 144

- 7.7 Mobility as a function of the applied electric field. The mobility increases with the electric field, as the reaction equilibria shift toward the region where ions move freely (i.e. ions break free from the gel backbone). The contrast in the mobility is larger for dilute gels ( $N = 100$ ). Under specific assumptions, the (relative) mobility at zero field is lower in dilute gels than the more dense gels. The simulations were required to confirm these assumptions, and to show the same qualitative trend without these assumptions. The inset shows the fraction of the ion population in each of the three regions as a function of  $E$ , for  $N = 30$ . 148
- 8.1 Induced charge of plane. 153
- 8.2 Induced charge of sphere. 154
- 8.3 Induced charge of cylinder. 155
- 8.4 System we are going to study: Ionic transport in nanchannel. 155

## CHAPTER 1

### **Introduction**

It is hard to overstate the importance of the electrostatic force in soft-matter systems with charges. Electrostatic interactions play an major role in determining the structure and function of several biological macromolecules, such as proteins and DNA [2, 3]. In cell signaling, the creation of electrical potential differences and ionic transport are of chief importance [4]. On the other hand, electrostatic forces allow the stabilization of many synthetic structures, endowed with remarkable properties: self-assembled colloidal dispersions [5], overcharged surfaces [6], patterned surfaces by competition between short-range and Coulombic interactions [7], and faceted thin shells [8].

It is imperative to mention that, in soft-matter systems with charges, most real situations involve regions with different dielectric response, as is the case for proteins within an aqueous cellular medium or for emulsions where oil and water are partitioned [9]. Due to the ensuing theoretical and computational challenges, this inhomogeneous dielectric response of the medium is often ignored or excessively simplified. Nevertheless, to accurately understand the role of electrostatic interactions in such systems, it is important to take into account the presence of dielectric heterogeneities in the medium.

All-atom simulations are considered the best tool to study dielectric inhomogeneity, since polarization effects are included in the atomic details of the solvent molecules. However, those simulations are generally prohibitively expensive, and the role of surface polarization cannot be extracted. Therefore, coarse-grained molecular dynamics (CGMD) that

include explicitly surface polarization effects are desired [10]. Recently, surface polarization has been introduced in implicit solvent CGMD simulations using the boundary element method [11, 12, 13], perturbation theory [14] and the variational method [15, 16]. The variational method is further extended and validated for better performance, which will be discussed in the method part (Chapter 2).

With such a tool, we can study many interesting phenomena. For example, aggregation of foreign phases in dielectric media that contain ions is ubiquitous in biological systems, oil refining industry and water purification membranes [4, 17, 18]. Segregation of ion-containing emulsions in organic solvents is particularly important in extraction of rare earths and nuclear waste. Therefore, we investigate the surface polarization effects on ion-containing emulsions (Chapter 3). Another example is the polarizable interface between two dielectric media, which has important effects on the electrolytes in its vicinity. This becomes more complicated when there are charged amphiphile molecules at the interface, as in the solvent extraction process. Our studies show a nontrivial structured interface will cause symmetry breaking in electrolytes distribution (Chapter 4).

As mentioned, solvent extraction [19], also known as liquid-liquid extraction, is a common technique used to remove a specific ion or compound from an aqueous solution. The process works by bringing together two immiscible liquid phases, an aqueous phase containing the dissolved ions and another liquid phase, usually with specialized extractant molecules at the interface. The desired ion is then preferentially transferred to the non-aqueous solvent, resulting in a target-metal-rich solvent phase and a waste aqueous phase. This method has applications in mining and refinement of rare earth metals, in nuclear fuel reprocessing (actinide separation), and in the cleanup of toxic waste [19, 20, 21, 22].

Despite decades of research into the mechanics and development of solvent extraction [20, 23], and its widespread use in industry, there is very little understanding of many fundamental aspects of the process. Besides the polarization at the interface, the dynamical dissociation of charges of extractant molecules is another obstacle. Therefore, Monte-Carlo simulation is introduced to study the intra-lanthanide selectivity (Chapter 5).

Also, we can use Monte-Carlo simulation to study the self assemblies of charged amphiphiles, which have wide-ranging applications including extraction, decontamination, remediation and biosensing (Chapter 6). The degree of ionization is sensitively dependent on external parameters such as pH and salt concentration, which provides a unique platform for the design of materials with controllable structural features at different length scales.

To further extend our research in electrostatic systems, we can apply external field and study the transport properties. Ion dynamics in non-equilibrium simulation in itself is a difficult topic, even without considering structure and conformation changes in the ionic environment. However, in most circumstances, it is not possible to extend equilibrium studies to include dynamical effects because systems driven out of equilibrium often take conformations not accessible in equilibrium, especially when charges are involved. Ionic transport in heterogeneous media on the microscale and nanoscale is of paramount interest for many applications including water desalination systems [24, 25], biomimetic systems [26, 27], as well as the potential for future generations of man-made devices, which can interface and be intrinsically compatible with biological tissues. During the past few years, large research effort and significant progress have been achieved in the area of ionic

devices, such as ionic diodes [28, 29, 30], ionic transistors [31, 32, 33, 34], and ionic conductors [35, 36]. Also, ionic conduction of polymer electrolyte confined in micro and nanopores has wide applications in batteries and fuel cells [37]. So we present our work on ion dynamics in Chapter 7.

In Chapter 8, we summarize our work and give a brief discussion for promising future work.

## CHAPTER 2

**Method****2.1. Variational approach for dielectric response**

For charged systems, one of the major difficulties in simulation is to accurately calculate the effects of dielectric medium on the charges and similarly the effects of charges on the medium's dielectric response. Generally, such information comes at the cost of solving the Poisson equation

$$(2.1) \quad -\nabla^2\Phi(\mathbf{r}) = \frac{\rho(\mathbf{r})}{\epsilon}$$

at each time step of the simulation. It is often advantageous to think of alternative ways to approach problems in electrostatics than to directly attack the Poisson equation to determine the electrostatic potential. For example, in the problem of charges present in two different dielectric media separated by a single interface, it is desirable to choose the polarization charge density (also called the induced charge density) as the variable to solve for rather than the potential. This is because the unknown induced charge density lies only on the interface, thus presenting a reduction of the full three-dimensional electrostatic problem to a two-dimensional surface problem.

Similarly, instead of directly investing in the expensive procedure of solving the Poisson equation, which is a second order partial differential equation, it is often desirable to adopt a variational approach. This is especially the case if one is interested in simulations of

charges in heterogeneous media, where one faces the task of solving the Poisson equation at every step of the simulation. Under a variational formulation we are offered the possibility of bypassing the effort spent to explicitly solve Poisson equation at each step by framing the problem in such a way that the very process of updating the simulation guarantees the solving of Poisson equation. In other words, Poisson equation is solved on the fly in tandem with the generation of the new charge configuration. Algorithms that implement this possibility are known as dynamical optimization algorithms and such schemes are valid only when the functional underlying the variational formulation is an energy functional <sup>1</sup>.

We use the energy functional for a general electrostatics problem with the polarization charge density as the only function variable. The functional  $I[\omega]$  has such form [16, 38]:

$$(2.2) \quad I[\omega] = \frac{1}{2} \iint \rho(\mathbf{r}) G(\mathbf{r}, \mathbf{r}') (\rho(\mathbf{r}') + s[\omega](r')) d^3 \mathbf{r} d^3 \mathbf{r}' \\ - \frac{1}{2} \iint s[\omega](\mathbf{r}) G(\mathbf{r}, \mathbf{r}') (\omega(\mathbf{r}') - s[\omega](r')) d^3 \mathbf{r} d^2 \mathbf{s}$$

where

$$s[\omega](r) = \nabla \cdot \left[ \chi(r) \nabla_r \int G(\mathbf{r}, \mathbf{r}') (\rho(\mathbf{r}') + \omega(r')) d^3 \mathbf{r}' \right]$$

For piecewise uniform dielectric media, the total induced charge density  $\omega(r)$  splits into two parts:  $\omega_P(r)$ , which presents on the point charges induced charge density;  $\omega_I(r)$ , which is located at the interface.

---

<sup>1</sup> A functional is an energy functional when it *minimizes* to reveal the *correct* energy in the system

## 2.2. General functional for multiple interfaces

The functional can be written as:

$$\begin{aligned}
(2.3) \quad I[w] = & \frac{1}{2} \iint \rho(\mathbf{r}) G(\mathbf{r}, \mathbf{r}') \frac{\rho(\mathbf{r}')}{\epsilon(\mathbf{r}')} d^3 \mathbf{r} d^3 \mathbf{r}' \\
& + \frac{1}{2} \iint \frac{\rho(\mathbf{r})}{\epsilon(\mathbf{r})} G(\mathbf{r}, \mathbf{s}) \Omega(\mathbf{s}) d^3 \mathbf{r} d^2 \mathbf{s} \\
& - \frac{1}{2} \iint \frac{1 - \epsilon(\mathbf{r})}{\epsilon(\mathbf{r})} \rho(\mathbf{r}) G(\mathbf{r}, \mathbf{s}) \omega(\mathbf{s}) d^3 \mathbf{r} d^2 \mathbf{s} \\
& - \frac{1}{2} \iint \Omega(\mathbf{s}) G(\mathbf{s}, \mathbf{s}') \omega(\mathbf{s}') d^2 \mathbf{s} d^2 \mathbf{s}' \\
& + \frac{1}{2} \iint \Omega(\mathbf{s}) G(\mathbf{s}, \mathbf{s}') \Omega(\mathbf{s}') d^2 \mathbf{s} d^2 \mathbf{s}'
\end{aligned}$$

where

$$(2.4) \quad \Omega(\mathbf{s}) = \nabla_s \cdot \left( \chi(\mathbf{r}) \nabla_s \left( \int G(\mathbf{s}, \mathbf{r}) \frac{\rho(\mathbf{r})}{\epsilon(\mathbf{r})} d^3 \mathbf{r} + \int G(\mathbf{s}, \mathbf{s}') \omega(\mathbf{s}') d^2 \mathbf{s}' \right) \right)$$

Generally, for any number of sharp interfaces ( $u$  and  $u'$  are indice of interfaces):

$$\begin{aligned}
(2.5) \quad \Omega(\mathbf{s}) = & \sum_u (1 - \epsilon_u) \omega(\mathbf{s}_u) \\
& + \sum_u \epsilon_{du} \hat{\mathbf{n}}_u \cdot \nabla_u \int G(\mathbf{s}_u, \mathbf{r}) \frac{\rho(\mathbf{r})}{\epsilon(\mathbf{r})} d^3 \mathbf{r} \\
& + \sum_u \sum_{u'} \epsilon_{du} \hat{\mathbf{n}}_u \cdot \nabla_u \int G(\mathbf{s}_u, \mathbf{s}_{u'}) \omega(\mathbf{s}_{u'}) d^2 \mathbf{s}_{u'}
\end{aligned}$$

where  $\epsilon_{mu} \equiv \frac{\epsilon_{u+} + \epsilon_{u-}}{2}$  defined as the dielectric constant of the interface (average between two regions), and  $\epsilon_{du} \equiv \frac{\epsilon_{u+} - \epsilon_{u-}}{4\pi}$  defined the difference between two regions.

Substitute (2.5) into (2.3) we obtain (I'll insert the derivation in later version):

$$\begin{aligned}
(2.6) \quad I[w] = & \frac{1}{2} \iint \rho(\mathbf{r}) R_{\rho\rho}(\mathbf{r}, \mathbf{r}') \rho(\mathbf{r}') d^3\mathbf{r} d^3\mathbf{r}' \\
& + \frac{1}{2} \sum_u \iint \rho(\mathbf{r}) R_{\rho\omega}(\mathbf{r}, \mathbf{s}_u) \omega(\mathbf{s}_u) d^3\mathbf{r} d^2\mathbf{s} \\
& + \frac{1}{2} \sum_u \sum_{u'} \iint \omega(\mathbf{s}) R_{\omega\omega}(\mathbf{s}_u, \mathbf{s}_{u'}) \omega(\mathbf{s}_{u'}) d^2\mathbf{s} d^2\mathbf{s}'
\end{aligned}$$

where

$$\begin{aligned}
(2.7) \quad R_{\rho\rho}(\mathbf{r}, \mathbf{r}') &= \frac{1}{\epsilon(\mathbf{r}')} G(\mathbf{r}, \mathbf{r}') + \frac{1}{\epsilon(\mathbf{r})\epsilon(\mathbf{r}')} \mathcal{G}(\mathbf{r}, \mathbf{r}') + \frac{1}{\epsilon(\mathbf{r})\epsilon(\mathbf{r}')} \mathcal{G}(\mathbf{r}, \mathbf{r}') \\
R_{\rho\omega}(\mathbf{r}, \mathbf{s}_u) &= \left(1 - \frac{\epsilon_u}{\epsilon(\mathbf{r})}\right) G(\mathbf{r}, \mathbf{s}_u) + \frac{1 - 2\epsilon_u}{\epsilon(\mathbf{r})} \mathcal{G}(\mathbf{s}_u, \mathbf{r}) + \frac{1}{\epsilon(\mathbf{r})} \mathcal{G}(\mathbf{r}, \mathbf{s}_u) + \frac{2}{\epsilon(\mathbf{r})} \mathcal{G}(\mathbf{r}, \mathbf{s}_u) \\
R_{\omega\omega}(\mathbf{s}_u, \mathbf{s}_{u'}) &= \epsilon_u(\epsilon_{u'} - 1) G(\mathbf{s}_u, \mathbf{s}_{u'}) + (1 - \epsilon_u - \epsilon_{u'}) \mathcal{G}(\mathbf{s}_u, \mathbf{s}_{u'}) + \mathcal{G}(\mathbf{s}_u, \mathbf{s}_{u'})
\end{aligned}$$

and

$$\begin{aligned}
(2.8) \quad \mathcal{G}(a, b) &\equiv \sum_u \int G(a, \mathbf{s}_u) \epsilon_{du} \hat{\mathbf{n}}_u \cdot \nabla_u G(\mathbf{s}_u, b) d^2\mathbf{s}_u \\
\mathcal{G}(a, b) &\equiv \sum_u \sum_{u'} \iint \epsilon_{du} \hat{\mathbf{n}}_u \cdot \nabla_u G(\mathbf{s}_u, a) G(\mathbf{s}_u, \mathbf{s}_{u'}) \epsilon_{d'u'} \hat{\mathbf{n}}_{u'} \cdot \nabla_{u'} G(\mathbf{s}_{u'}, b) d^2\mathbf{s}_u d^2\mathbf{s}_{u'}
\end{aligned}$$

where  $\mathbf{r}$ ,  $\mathbf{r}'$  are position vectors of ions, and  $\mathbf{s}_u$  is the position vector on interface  $u$ . Equations (2.6) (2.7) (2.8) are all we need. Notice the definition of  $\mathcal{G}$  and  $\mathcal{G}$  are different here compared to previous notes, we absorb the  $\epsilon_d$  into the definition so that (2.6) has a general simply form for any number of interfaces.

## 2.3. Numerical Implementation

### 2.3.1. Discretization

The numerical approach begins with representing the interface between the two dielectrics by a set of discrete grid points. Let us suppose  $M$  points grid the interface. We label the position vectors of these points as  $\mathbf{s}_k$ , where the subscript identifies the  $k^{\text{th}}$  point. Each grid point, called a vertex from now on, is assigned an area  $a_k$  so as to effect the transition from the continuum form of the functional  $I[\omega]$  (which involves integrals) to a discrete version as required for the numerical exploration. Each vertex also gets its own normal vector  $\hat{n}_k$ . Thus the surface integrals appearing in the functional move to discrete sums:

$$(2.9) \quad \int \dots d^2s \quad \longrightarrow \quad \sum_{k=1}^M \dots a_k$$

and a function prescribed on the surface, such as, for example the surface induced charge density, becomes a function of the discrete position vectors:

$$(2.10) \quad \omega(\mathbf{s}) \quad \longrightarrow \quad \omega(\mathbf{s}_k) \equiv \omega_k$$

where  $\omega_k$  is the induced charge density at the  $k^{\text{th}}$  vertex. As noted before, we represent the free charges (ions) as point charges and, the bulk free charge density  $\rho(\mathbf{r})$  is expressed as the discrete sum:

$$(2.11) \quad \rho(\mathbf{r}) = \sum_{i=1}^N q_i \delta(\mathbf{r} - \mathbf{r}_i),$$

where we consider  $N$  ions in the system with  $q_i$  being the charge of the  $i^{\text{th}}$  ion and  $\mathbf{r}_i$  its position vector. Employing equations (2.9)-(2.11) the functional can be transformed into

its discretized form:

$$(2.12) \quad I[\omega] = \frac{1}{2} \sum_{i=1}^N \sum_{j=1}^N q_i R_{\rho\rho}(\mathbf{r}_i, \mathbf{r}_j) q_j + \frac{1}{2} \sum_{i=1}^N \sum_{k=1}^M q_i R_{\rho\omega}(\mathbf{r}_i, \mathbf{s}_k) \omega_k a_k + \frac{1}{2} \sum_{k=1}^M \sum_{l=1}^M \omega_k a_k R_{\omega\omega}(\mathbf{s}_k, \mathbf{s}_l) \omega_l a_l.$$

Recall that the functions  $R_{\rho\rho}$ ,  $R_{\rho\omega}$ , and  $R_{\omega\omega}$  are given by equations (2.7). These  $R$  functions require the evaluation of renormalized Green's functions  $\mathcal{G}$  and  $\mathcal{G}$ . We introduced these renormalized Green's functions in equations (2.8). For a numerical evaluation of these functions we need to work with the discretized form which, by employing (2.9) and (2.10), is found to be

$$(2.13) \quad \begin{aligned} \mathcal{G}(\mathbf{a}, \mathbf{b}) &\equiv \sum_{m=1}^M G(\mathbf{a}, \mathbf{s}_m) \epsilon_{dm} \hat{\mathbf{n}}_m \cdot \nabla_m G(\mathbf{s}_m, \mathbf{b}) a_m \\ \mathcal{G}(\mathbf{a}, \mathbf{b}) &\equiv \sum_{m=1}^M \sum_{l=1}^M \epsilon_{dm} \hat{\mathbf{n}}_m \cdot \nabla_m G(\mathbf{s}_m, \mathbf{a}) G(\mathbf{s}_m, \mathbf{s}_l) \epsilon_{dl} \hat{\mathbf{n}}_l \cdot \nabla_l G(\mathbf{s}_l, \mathbf{b}) a_m a_l \end{aligned}$$

Using equations (2.13) and (2.7), the functional  $I[\{\omega_k\}]$  can be evaluated for any set of discrete induced charge values  $\{\omega_k\}$ . One cautionary note before we move forward. The bare Green's function  $G(\mathbf{s}_k, \mathbf{s}_l)$  and its gradient  $\nabla G(\mathbf{s}_k, \mathbf{s}_l)$ , which are required for the computation of  $\mathcal{G}$  and  $\mathcal{G}$  and also the  $R$  functions, diverge at the point  $k = l$ . The discretization of the functional leads us to the expression where we will encounter such divergences. To get around these divergences we employ the standard trick of approximating the sum by an integral expression at these special points, and evaluate the subsequent integral analytically. These integrals are easy to evaluate in symmetric geometries, such as sphere or cylinder. For more complicated shapes we will have to get them in an approximate analytical form which is indeed possible.

### 2.3.2. Calculate Induced charge

As demonstrated in original notes, we need to minimize the functional (2.12) to obtain the induced charge at each time step. The simplest way to minimize a function is to take the derivative:

$$(2.14) \quad \nabla_{\omega} I[\omega] = 0, \quad \text{and} \quad \nabla_{\omega}^2 I[\omega] > 0$$

We have

$$(2.15) \quad \nabla_{\omega_k} I[\omega] = \frac{1}{2} \sum_{i=1}^N q_i R_{\rho\omega}(\mathbf{r}_i, \mathbf{s}_k) + \frac{1}{2} \sum_{l=1}^M [R_{\omega\omega}(\mathbf{s}_k, \mathbf{s}_l) + R_{\omega\omega}(\mathbf{s}_l, \mathbf{s}_k)] \omega_l a_l.$$

This has the matrix form of a linear equation

$$(2.16) \quad (R_{\omega\omega} + R_{\omega\omega}^T) \vec{\omega} + qR_{\rho\omega} = 0$$

so

$$(2.17) \quad \vec{\omega} = (R_{\omega\omega} + R_{\omega\omega}^T)^{-1} qR_{\rho\omega}$$

A naive method would solve this matrix (inversion of matrix) at every time step. However, there are faster methods to work around the time consuming inversion of matrix, for example, iterative method [12] and CarParrinello molecular dynamics (CPMD) on-the-fly optimization [15]. We'll discuss the non-static interfaces in details later. On the other hand, for static interfaces, it's not a problem since  $(R_{\omega\omega} + R_{\omega\omega}^T)^{-1}$  never changes. So we can calculate this term at the beginning and store it during the whole simulation. Then at every time step, only the  $qR_{\rho\omega}$  needs to be updated.

Notice numerically implementation need a good behavior matrix  $R_{\omega\omega} + R_{\omega\omega}^T$ . In some extreme conditions, such as all  $\epsilon_u = 1$  for all vertex on the interfaces, and only one planar interface, e.g.  $\hat{\mathbf{n}}_m \cdot \nabla_m G(\mathbf{s}_m, \mathbf{s}_l) = 0$ , Then  $R_{\omega\omega} = 0$ , no inversion exists. Such details should be taken care of during the real implementation.

### 2.3.3. Static interfaces

When interfaces are fixed, we only need to solve the matrix  $R_{\omega\omega}$  once. Every time step, we only need to update the quantity:

$$(2.18) \quad \sum_i q_i R_{\rho\omega}(r_i, s_k)$$

$R_{\omega\omega}$  can be calculated using same formula in previous document, just note there are triple loop in that implementation. As long as it's only calculated once, no need to optimize.

### 2.3.4. Non-periodic boundary condition

If the system has open boundary condition, (2.12) can be easily evaluated by counting all  $N$  ions and  $M$  vertices on the interfaces, where

$$(2.19) \quad G(\mathbf{a}, \mathbf{b}) = \frac{1}{|\mathbf{a} - \mathbf{b}|}$$

and

$$(2.20) \quad \nabla_{\mathbf{a}} G(\mathbf{a}, \mathbf{b}) = -\frac{\mathbf{a} - \mathbf{b}}{|\mathbf{a} - \mathbf{b}|^3}$$

### 2.3.5. Periodic boundary condition

Under periodic boundary condition, the system becomes infinity, containing infinity number of ions and vertices. We denote  $\mathbf{n}$  and  $\mathbf{n}'$  as the index of periodic images, and  $\mathbf{L}$  is the periodic vector, each unit cell contains  $N$  ions and  $M$  vertices, the functional (2.12) can be rewritten into

$$\begin{aligned}
 (2.21) \quad I[\omega] = & \sum_{\mathbf{n}'=-\infty}^{+\infty} \sum_{\mathbf{n}=-\infty}^{+\infty} \left[ \frac{1}{2} \sum_{i=1}^N \sum_{j=1}^N q_i R_{\rho\rho}(\mathbf{r}_i + \mathbf{n} \cdot \mathbf{L}, \mathbf{r}_j + \mathbf{n}' \cdot \mathbf{L}) q_j \right. \\
 & + \frac{1}{2} \sum_{i=1}^N \sum_{k=1}^M q_i R_{\rho\omega}(\mathbf{r}_i + \mathbf{n} \cdot \mathbf{L}, \mathbf{s}_k + \mathbf{n}' \cdot \mathbf{L}) \omega_k a_k \\
 & \left. + \frac{1}{2} \sum_{k=1}^M \sum_{l=1}^M \omega_k a_k R_{\omega\omega}(\mathbf{s}_k + \mathbf{n} \cdot \mathbf{L}, \mathbf{s}_l + \mathbf{n}' \cdot \mathbf{L}) \omega_l a_l. \right]
 \end{aligned}$$

Since only relative distance between two particles is important, the above equation can be reformulated into

$$\begin{aligned}
(2.22) \quad I[\omega] &= \sum_{\mathbf{n}'=-\infty}^{+\infty} \sum_{\mathbf{n}=-\infty}^{+\infty} \left[ \frac{1}{2} \sum_{i=1}^N \sum_{j=1}^N q_i R_{\rho\rho}(\mathbf{r}_i, \mathbf{r}_j + (\mathbf{n}' - \mathbf{n}) \cdot \mathbf{L}) q_j \right. \\
&\quad + \frac{1}{2} \sum_{i=1}^N \sum_{k=1}^M q_i R_{\rho\omega}(\mathbf{r}_i, \mathbf{s}_k + (\mathbf{n}' - \mathbf{n}) \cdot \mathbf{L}) \omega_k a_k \\
&\quad \left. + \frac{1}{2} \sum_{k=1}^M \sum_{l=1}^M \omega_k a_k R_{\omega\omega}(\mathbf{s}_k, \mathbf{s}_l + (\mathbf{n}' - \mathbf{n}) \cdot \mathbf{L}) \omega_l a_l \right] \\
I[\omega] &= \sum_{\mathbf{n}'=-\infty}^{+\infty} \sum_{\mathbf{n}'-\mathbf{n}=-\infty}^{+\infty} \left[ \frac{1}{2} \sum_{i=1}^N \sum_{j=1}^N q_i R_{\rho\rho}(\mathbf{r}_i, \mathbf{r}_j + (\mathbf{n}' - \mathbf{n}) \cdot \mathbf{L}) q_j \right. \\
&\quad + \frac{1}{2} \sum_{i=1}^N \sum_{k=1}^M q_i R_{\rho\omega}(\mathbf{r}_i, \mathbf{s}_k + (\mathbf{n}' - \mathbf{n}) \cdot \mathbf{L}) \omega_k a_k \\
&\quad \left. + \frac{1}{2} \sum_{k=1}^M \sum_{l=1}^M \omega_k a_k R_{\omega\omega}(\mathbf{s}_k, \mathbf{s}_l + (\mathbf{n}' - \mathbf{n}) \cdot \mathbf{L}) \omega_l a_l \right]
\end{aligned}$$

The above term surely will blow up since infinity system has infinity energy. By simply removing the 1st index  $n'$ , we obtain the energy per unit cell

$$\begin{aligned}
(2.23) \quad I[\omega] &= \sum_{\mathbf{n}=-\infty}^{+\infty} \left[ \frac{1}{2} \sum_{i=1}^N \sum_{j=1}^N q_i R_{\rho\rho}(\mathbf{r}_i, \mathbf{r}_j + \mathbf{n} \cdot \mathbf{L}) q_j \right. \\
&\quad + \frac{1}{2} \sum_{i=1}^N \sum_{k=1}^M q_i R_{\rho\omega}(\mathbf{r}_i, \mathbf{s}_k + \mathbf{n} \cdot \mathbf{L}) \omega_k a_k \\
&\quad \left. + \frac{1}{2} \sum_{k=1}^M \sum_{l=1}^M \omega_k a_k R_{\omega\omega}(\mathbf{s}_k, \mathbf{s}_l + \mathbf{n} \cdot \mathbf{L}) \omega_l a_l \right]
\end{aligned}$$

Then we absorb the summation  $\sum_{\mathbf{n}=-\infty}^{+\infty}$  into all the  $R_{xx}$  terms. According to (2.7), the summation finally gets into  $G$ ,  $\mathcal{G}$  and  $\mathcal{G}$

$$(2.24) \quad G(\mathbf{r}, \mathbf{r}') \longrightarrow \sum_{\mathbf{n}=-\infty}^{+\infty} G(\mathbf{r}, \mathbf{r}' + \mathbf{n} \cdot \mathbf{L})$$

$$(2.25) \quad \mathcal{G}(\mathbf{r}, \mathbf{r}') \longrightarrow \sum_{\mathbf{n}=-\infty}^{+\infty} \mathcal{G}(\mathbf{r}, \mathbf{r}' + \mathbf{n} \cdot \mathbf{L})$$

$$(2.26) \quad \mathcal{G}(\mathbf{r}, \mathbf{r}') \longrightarrow \sum_{\mathbf{n}=-\infty}^{+\infty} \mathcal{G}(\mathbf{r}, \mathbf{r}' + \mathbf{n} \cdot \mathbf{L})$$

We now show (2.25) and (2.26) will reduce to (2.24). First we generalize (2.8) and (2.13) to periodic system:

$$(2.27) \quad \mathcal{G}(\mathbf{a}, \mathbf{b}) \equiv \sum_{\mathbf{n}'=-\infty}^{+\infty} \sum_{m=1}^M G(\mathbf{a}, \mathbf{s}_m + \mathbf{n}' \cdot \mathbf{L}) \epsilon_{dm} \hat{\mathbf{n}}_m \cdot \nabla_m G(\mathbf{s}_m + \mathbf{n}' \cdot \mathbf{L}, \mathbf{b}) a_m$$

$$(2.28) \quad \mathcal{G}(\mathbf{a}, \mathbf{b}) \equiv \sum_{\mathbf{n}'=-\infty}^{+\infty} \sum_{\mathbf{n}''=-\infty}^{+\infty} \sum_{m=1}^M \sum_{l=1}^M \left( \epsilon_{dm} \hat{\mathbf{n}}_m \cdot \nabla_m G(\mathbf{s}_m + \mathbf{n}' \cdot \mathbf{L}, \mathbf{a}) G(\mathbf{s}_m + \mathbf{n}' \cdot \mathbf{L}, \mathbf{s}_l + \mathbf{n}'' \cdot \mathbf{L}) \right. \\ \left. \epsilon_{dl} \hat{\mathbf{n}}_l \cdot \nabla_l G(\mathbf{s}_l + \mathbf{n}'' \cdot \mathbf{L}, \mathbf{b}) a_m a_l \right)$$

We have

$$\begin{aligned}
& \sum_{\mathbf{n}=-\infty}^{+\infty} \mathcal{G}(\mathbf{r}, \mathbf{r}' + \mathbf{n} \cdot \mathbf{L}) \\
&= \sum_{\mathbf{n}=-\infty}^{+\infty} \sum_{\mathbf{n}'=-\infty}^{+\infty} \sum_{m=1}^M G(\mathbf{r}, \mathbf{s}_m + \mathbf{n}' \cdot \mathbf{L}) \epsilon_{dm} \hat{\mathbf{n}}_m \cdot \nabla_m G(\mathbf{s}_m + \mathbf{n}' \cdot \mathbf{L}, \mathbf{r}' + \mathbf{n} \cdot \mathbf{L}) a_m \\
(2.29) \quad &= \sum_{\mathbf{n}-\mathbf{n}'=-\infty}^{+\infty} \sum_{\mathbf{n}'=-\infty}^{+\infty} \sum_{m=1}^M G(\mathbf{r}, \mathbf{s}_m + \mathbf{n}' \cdot \mathbf{L}) \epsilon_{dm} \hat{\mathbf{n}}_m \cdot \nabla_m G(\mathbf{s}_m, \mathbf{r}' + (\mathbf{n} - \mathbf{n}') \cdot \mathbf{L}) a_m \\
&= \sum_{\mathbf{n}''=-\infty}^{+\infty} \sum_{\mathbf{n}'=-\infty}^{+\infty} \sum_{m=1}^M G(\mathbf{r}, \mathbf{s}_m + \mathbf{n}' \cdot \mathbf{L}) \epsilon_{dm} \hat{\mathbf{n}}_m \cdot \nabla_m G(\mathbf{s}_m, \mathbf{r}' + \mathbf{n}'' \cdot \mathbf{L}) a_m \\
&= \sum_{m=1}^M \left( \left[ \sum_{\mathbf{n}'=-\infty}^{+\infty} G(\mathbf{r}, \mathbf{s}_m + \mathbf{n}' \cdot \mathbf{L}) \right] \epsilon_{dm} \hat{\mathbf{n}}_m \cdot \nabla_m \left[ \sum_{\mathbf{n}''=-\infty}^{+\infty} G(\mathbf{s}_m, \mathbf{r}' + \mathbf{n}'' \cdot \mathbf{L}) \right] a_m \right)
\end{aligned}$$

and similarly

$$\begin{aligned}
\sum_{\mathbf{n}=-\infty}^{+\infty} \mathcal{G}(\mathbf{r}, \mathbf{r}' + \mathbf{n} \cdot \mathbf{L}) &= \sum_{\mathbf{n}=-\infty}^{+\infty} \sum_{\mathbf{n}'=-\infty}^{+\infty} \sum_{\mathbf{n}''=-\infty}^{+\infty} \sum_{m=1}^M \sum_{l=1}^M \left( \epsilon_{dm} \hat{\mathbf{n}}_m \cdot \nabla_m G(\mathbf{s}_m + \mathbf{n}' \cdot \mathbf{L}, \mathbf{r}) \right. \\
&\quad \left. G(\mathbf{s}_m + \mathbf{n}' \cdot \mathbf{L}, \mathbf{s}_l + \mathbf{n}'' \cdot \mathbf{L}) \epsilon_{dl} \hat{\mathbf{n}}_l \cdot \nabla_l G(\mathbf{s}_l + \mathbf{n}'' \cdot \mathbf{L}, \mathbf{r}' + \mathbf{n} \cdot \mathbf{L}) a_m a_l \right) \\
&= \sum_{\mathbf{n}=-\infty}^{+\infty} \sum_{\mathbf{n}'=-\infty}^{+\infty} \sum_{\mathbf{n}''=-\infty}^{+\infty} \sum_{m=1}^M \sum_{l=1}^M \left( \epsilon_{dm} \hat{\mathbf{n}}_m \cdot \nabla_m G(\mathbf{s}_m + \mathbf{n}' \cdot \mathbf{L}, \mathbf{r}) G(\mathbf{s}_m, \mathbf{s}_l + (\mathbf{n}'' - \mathbf{n}') \cdot \mathbf{L}) \right. \\
&\quad \left. \epsilon_{dl} \hat{\mathbf{n}}_l \cdot \nabla_l G(\mathbf{s}_l, \mathbf{r}' + (\mathbf{n} - \mathbf{n}'') \cdot \mathbf{L}) a_m a_l \right) \\
&= \sum_{\mathbf{n}-\mathbf{n}''=-\infty}^{+\infty} \sum_{\mathbf{n}''-\mathbf{n}'=-\infty}^{+\infty} \sum_{\mathbf{n}'=-\infty}^{+\infty} \sum_{m=1}^M \sum_{l=1}^M \left( \epsilon_{dm} \hat{\mathbf{n}}_m \cdot \nabla_m G(\mathbf{s}_m + \mathbf{n}' \cdot \mathbf{L}, \mathbf{r}) G(\mathbf{s}_m, \mathbf{s}_l + (\mathbf{n}'' - \mathbf{n}') \cdot \mathbf{L}) \right. \\
&\quad \left. \epsilon_{dl} \hat{\mathbf{n}}_l \cdot \nabla_l G(\mathbf{s}_l, \mathbf{r}' + (\mathbf{n} - \mathbf{n}'') \cdot \mathbf{L}) a_m a_l \right) \\
&= \sum_{\mathbf{n}_1=-\infty}^{+\infty} \sum_{\mathbf{n}_2=-\infty}^{+\infty} \sum_{\mathbf{n}'=-\infty}^{+\infty} \sum_{m=1}^M \sum_{l=1}^M \left( \epsilon_{dm} \hat{\mathbf{n}}_m \cdot \nabla_m G(\mathbf{s}_m + \mathbf{n}' \cdot \mathbf{L}, \mathbf{r}) G(\mathbf{s}_m, \mathbf{s}_l + \mathbf{n}_2 \cdot \mathbf{L}) \right. \\
&\quad \left. \epsilon_{dl} \hat{\mathbf{n}}_l \cdot \nabla_l G(\mathbf{s}_l, \mathbf{r}' + \mathbf{n}_1 \cdot \mathbf{L}) a_m a_l \right) \\
&= \sum_{m=1}^M \sum_{l=1}^M \left( \epsilon_{dm} \hat{\mathbf{n}}_m \cdot \nabla_m \left[ \sum_{\mathbf{n}'=-\infty}^{+\infty} G(\mathbf{s}_m + \mathbf{n}' \cdot \mathbf{L}, \mathbf{r}) \right] \left[ \sum_{\mathbf{n}_2=-\infty}^{+\infty} G(\mathbf{s}_m, \mathbf{s}_l + \mathbf{n}_2 \cdot \mathbf{L}) \right] \right. \\
&\quad \left. \epsilon_{dl} \hat{\mathbf{n}}_l \cdot \nabla_l \left[ \sum_{\mathbf{n}_1=-\infty}^{+\infty} G(\mathbf{s}_l, \mathbf{r}' + \mathbf{n}_1 \cdot \mathbf{L}) \right] a_m a_l \right) \tag{2.26}
\end{aligned}$$

So the only difficult for periodic system is to calculate

$$\sum_{\mathbf{n}=-\infty}^{+\infty} G(\mathbf{r}, \mathbf{r}' + \mathbf{n} \cdot \mathbf{L})$$

### 2.3.6. Real space and reciprocal space separation

The common techniques to calculate  $\sum_{\mathbf{n}=-\infty}^{+\infty} G(\mathbf{r}, \mathbf{r}' + \mathbf{n} \cdot \mathbf{L})$  is to separate Green's functions into real space and reciprocal space  $G = G^R + G^K$ . This is usually done by employing Error function  $\text{erf}(x)$  and its complementary  $\text{erfc}(x)$ . Since  $\text{erf}(x) + \text{erfc}(x) = 1$ , we have

$$(2.27) \quad \frac{1}{r} = \frac{\text{erfc}(\alpha r)}{r} + \frac{\text{erf}(\alpha r)}{r}$$

where  $\alpha$  is just a parameter. The 1st term has a singular behavior as  $r \rightarrow 0$ , but decays exponentially as  $r \rightarrow \infty$ . The 2nd term goes to a constant as  $r \rightarrow 0$  but has a long range tail as  $r \rightarrow \infty$ . So the 1st term can be estimated accurately in real space with a reasonable truncate cutoff length, while the 2nd term has to be calculated in reciprocal space for a faster convergence. They are denoted as real space term and kspace term respectively. Reciprocal space calculation depends on different methods such as Ewald or PPPM.

### 2.3.7. Ewald method

There are many ways to derive the exact Ewald formula. Typically, the total energy of a charge neutral unitcell is considered, and then separated into real space term with a double summation over all the charged particles and a kspace term with summation over dozens of  $\mathbf{k}$  points of the structure factor  $S(\mathbf{k}) = \sum_{i=1}^N q_i e^{i\mathbf{k}\mathbf{r}_i}$ . However, we are going to follow another procedure (cite something here), starting from the Ewald potential of a single unit charge. This way, we do not need to assume the charge neutrality, as a neutralizing background is present automatically. We will show this would be better for general derivation, and it can give us the correct physics when dealing with some

test system (for example, single unit charge in an infinite long cylinder) in the following chapters.

We express the Green's function as (derivation skipped):

$$\begin{aligned}
 \sum_n^\infty G(\mathbf{r}_1, \mathbf{r}_2 + \mathbf{nL}) &= \sum_n^\infty \frac{1}{|\mathbf{r}_1 - \mathbf{r}_2 - \mathbf{nL}|} \equiv \sum_n^\infty \frac{1}{|\mathbf{r} - \mathbf{nL}|} \\
 (2.28) \qquad \qquad \qquad &= \sum_n^{\text{cutoff}} \frac{\text{erfc}(\alpha|\mathbf{r} + \mathbf{n} \cdot \mathbf{L}|)}{|\mathbf{r} + \mathbf{n} \cdot \mathbf{L}|} + \frac{4\pi}{V} \sum_{k \neq 0} \frac{e^{-k^2/4\alpha^2}}{k^2} e^{i\mathbf{k} \cdot \mathbf{r}} - \frac{\pi}{V\alpha^2}
 \end{aligned}$$

where the last term is neutralizing background potential. If the whole system is neutral, the last term would be zero, and the summation of Green's function between all pairs would reduce to the formula in any textbook. Notice the original summation is infinity, after separated in real space  $G^R$  and kspace  $G^K$ , the summation for real space only contains very few term within the cutoff range. Usually  $n$  only contains nearest  $\{-1, 0, +1\}$  periodic images, and only  $|\mathbf{r} + \mathbf{n} \cdot \mathbf{L}| < r_{\text{cut}}$  are considered, thus real space calculation is largely reduced.

**2.3.7.1. Ewald method for reciprocal calculation.** For Ewald method, the Green's function in reciprocal space is:

$$(2.29) \qquad \qquad \qquad G^K(\mathbf{r}, \mathbf{r}') = \frac{4\pi}{V} \sum_{k \neq 0} \frac{e^{-k^2/4\alpha^2}}{k^2} e^{i\mathbf{k} \cdot (\mathbf{r} - \mathbf{r}')}$$

According to (2.7),  $R_{\rho\omega}$  has four terms, so (2.18) has four terms.

**2.3.7.2. The 1st term:**

$$(2.30) \qquad \qquad \qquad \sum_i q_i \left(1 - \frac{\epsilon_{mk}}{\epsilon(\mathbf{r}_i)}\right) \left[ G^R(\mathbf{r}_i, \mathbf{s}_k) + G^K(\mathbf{r}_i, \mathbf{s}_k) \right]$$

only consider the Kspace term:

$$\begin{aligned}
 (2.31) \quad & \sum_i q_i \left(1 - \frac{\epsilon_{mk}}{\epsilon(\mathbf{r}_i)}\right) G^K(\mathbf{r}_i, \mathbf{s}_k) \\
 &= \frac{4\pi}{V} \sum_{k \neq 0} \frac{e^{-k^2/4\alpha^2}}{k^2} \left[ \left( \sum_i q_i e^{i\mathbf{k} \cdot \mathbf{r}_i} \right) e^{-i\mathbf{k} \cdot \mathbf{s}_k} - \epsilon_{mk} \left( \sum_i \frac{q_i}{\epsilon(\mathbf{r}_i)} e^{i\mathbf{k} \cdot \mathbf{r}_i} \right) e^{-i\mathbf{k} \cdot \mathbf{s}_k} \right]
 \end{aligned}$$

Now we define structure factors:

$$(2.32) \quad S_{ions}(\mathbf{k}) \equiv \sum_i q_i e^{i\mathbf{k} \cdot \mathbf{r}_i}$$

$$(2.33) \quad S_{ions,\epsilon}(\mathbf{k}) \equiv \sum_i \frac{q_i}{\epsilon(\mathbf{r}_i)} e^{i\mathbf{k} \cdot \mathbf{r}_i}$$

Notice traditional Ewald approach only need the 1st structure factor, while our functional needs more (we'll see others later). However, it's not a problem since the calculation of structure factors only have time scale  $\sim O(N)$ . In the code, we calculate cos and sin instead of exp, for example:

$$(2.34) \quad S_{ions}(\mathbf{k}) = \sum_i q_i (\cos \mathbf{k} \cdot \mathbf{r}_i + i \sin \mathbf{k} \cdot \mathbf{r}_i) \equiv \cos S_{ions}(\mathbf{k}) + i \sin S_{ions}(\mathbf{k})$$

$$(2.35) \quad e^{-i\mathbf{k} \cdot \mathbf{s}_k} = \cos \mathbf{k} \cdot \mathbf{s}_k - i \sin \mathbf{k} \cdot \mathbf{s}_k$$

we have

$$(2.36) \quad Re \left[ \left( \sum_i q_i e^{i\mathbf{k}\cdot\mathbf{r}_i} \right) e^{-i\mathbf{k}\cdot\mathbf{s}_k} \right] = \cos S_{ions}(\mathbf{k}) \cos(\mathbf{k} \cdot \mathbf{s}_k) + \sin S_{ions}(\mathbf{k}) \sin(\mathbf{k} \cdot \mathbf{s}_k)$$

$$(2.37) \quad Re \left[ \left( \sum_i \frac{q_i}{\epsilon(\mathbf{r}_i)} e^{i\mathbf{k}\cdot\mathbf{r}_i} \right) e^{-i\mathbf{k}\cdot\mathbf{s}_k} \right] = \cos S_{ions,\epsilon}(\mathbf{k}) \cos(\mathbf{k} \cdot \mathbf{s}_k) + \sin S_{ions,\epsilon}(\mathbf{k}) \sin(\mathbf{k} \cdot \mathbf{s}_k)$$

$$(2.38)$$

### 2.3.7.3. The 2nd term:

$$(2.39) \quad \sum_i q_i \left( \frac{1 - 2\epsilon_m}{\epsilon(\mathbf{r}_i)} \right) \int G(\mathbf{s}_m, \mathbf{s}_u) \epsilon_{dl} \hat{\mathbf{n}}_l \cdot \nabla_l G(\mathbf{s}_l, \mathbf{r}_i) d^2 \mathbf{s}_l$$

where  $G(\mathbf{s}_m, \mathbf{s}_u) = G^R + G^K$  has already been calculated when calculating all the interfaces terms, and  $\nabla_l G(\mathbf{s}_l, \mathbf{r}_i) = \nabla_l G^R + \nabla_l G^K$  need to be calculated. (2.39) can be reformulated into

$$(2.40) \quad (1 - 2\epsilon_m) \int G(\mathbf{s}_m, \mathbf{s}_u) \epsilon_{dl} \hat{\mathbf{n}}_l \cdot \left[ \sum_i \frac{q_i}{\epsilon(\mathbf{r}_i)} \nabla_l G^{R+K}(\mathbf{s}_l, \mathbf{r}_i) \right] d^2 \mathbf{s}_l$$

Only consider the kspace term in  $\nabla G$ , notice

$$(2.41) \quad \nabla_l G^K(\mathbf{s}_l, \mathbf{r}_i) = \frac{4\pi}{V} \sum_{k \neq 0} \frac{e^{-k^2/4\alpha^2}}{k^2} i\mathbf{k} e^{i\mathbf{k}\cdot(\mathbf{s}_l - \mathbf{r}_i)}$$

So kspace term in (2.39) becomes

$$(2.42) \quad (1 - 2\epsilon_m) \int G(\mathbf{s}_m, \mathbf{s}_u) \epsilon_{dl} \hat{\mathbf{n}}_l \cdot \left[ \sum_i \frac{q_i}{\epsilon(\mathbf{r}_i)} \nabla_l G^K(\mathbf{s}_l, \mathbf{r}_i) \right] d^2 \mathbf{s}_l$$

where

$$(2.43) \quad \sum_i \frac{q_i}{\epsilon(\mathbf{r}_i)} \nabla_l G^K(\mathbf{s}_l, \mathbf{r}_i) = \frac{4\pi}{V} \sum_{k \neq 0} \frac{e^{-k^2/4\alpha^2}}{k^2} \left[ \sum_i \frac{q_i}{\epsilon(\mathbf{r}_i)} e^{-i\mathbf{k} \cdot \mathbf{r}_i} \right] i\mathbf{k} e^{i\mathbf{k} \cdot \mathbf{s}_l}$$

Again, term in square bracket is one of the structure factors  $S_{ions,\epsilon}$ . In terms of cos and sin

$$(2.44) \quad Re \sim (\cos S - i \sin S) i\mathbf{k} (\cos + i \sin) = \mathbf{k} (\sin S_{ions,\epsilon} \cos(\mathbf{k} \cdot \mathbf{s}_l) - \cos S_{ions,\epsilon} \sin(\mathbf{k} \cdot \mathbf{s}_l))$$

#### 2.3.7.4. The 3rd term:

$$(2.45) \quad \sum_i \frac{q_i}{\epsilon(\mathbf{r}_i)} \int G(\mathbf{r}_i, \mathbf{s}_l) \epsilon_{dl} \hat{\mathbf{n}}_l \cdot \nabla_l G(\mathbf{s}_l, \mathbf{s}_m) d^2 \mathbf{s}_l$$

Similarly, the interface term has been calculated already, only consider  $G = G^R + G^K$

$$(2.46) \quad \sum_i \frac{q_i}{\epsilon(\mathbf{r}_i)} G^K(\mathbf{r}_i, \mathbf{s}_l) = \frac{4\pi}{V} \sum_{k \neq 0} \frac{e^{-k^2/4\alpha^2}}{k^2} \left( \sum_i \frac{q_i}{\epsilon(\mathbf{r}_i)} e^{i\mathbf{k} \cdot \mathbf{r}_i} \right) e^{-i\mathbf{k} \cdot \mathbf{s}_l}$$

The same as the 2nd term in (2.31)

#### 2.3.7.5. The 4th term:

$$(2.47) \quad \sum_i \frac{2}{\epsilon(\mathbf{r}_i)} \mathcal{G}(\mathbf{r}_i, \mathbf{s}_m) = \sum_i \frac{2}{\epsilon(\mathbf{r}_i)} \iint \epsilon_{dl} \hat{\mathbf{n}}_l \cdot \nabla_l G(\mathbf{s}_l, \mathbf{r}_i) G(\mathbf{s}_l, \mathbf{s}_k) \epsilon_{dk} \hat{\mathbf{n}}_k \cdot \nabla_k G(\mathbf{s}_k, \mathbf{s}_m) d^2 \mathbf{s}_l d^2 \mathbf{s}_k$$

where interface term  $G(\mathbf{s}_l, \mathbf{s}_k) \epsilon_{dk} \hat{\mathbf{n}}_k \cdot \nabla_k G(\mathbf{s}_k, \mathbf{s}_m)$  has already been calculated, only consider

$$(2.48) \quad \sum_i \frac{2}{\epsilon(\mathbf{r}_i)} \nabla_l G^K(\mathbf{s}_l, \mathbf{r}_i)$$

which is the same as in (2.43)

**2.3.7.6. Wrap it up.** After calculating those four terms, we obtain the quantity (2.18)

$$(2.49) \quad \sum_i q_i R_{\rho\omega}(r_i, s_k)$$

Together with the already known matrix  $R_{\omega\omega} + R_{\omega\omega}^T$ , we can calculate the induced charge for each time step.

The total energy functional (2.6) now can be evaluated. On the other hand, the total electrostatic energy can be calculated using

$$(2.50) \quad U = \frac{1}{2} \iint \rho(r) \frac{G(r, r')}{\epsilon(r')} \rho(r') d^3 r d^3 r' + \frac{1}{2} \iint \rho(r) G(r, s) \omega(s) d^3 r d^2 s$$

We can compare those two results for validation.

### 2.3.8. Force calculation

The electrostatic force on the  $i$ th ion is  $\mathbf{F}_i = -\nabla_{\mathbf{r}_i} U$ . In the minimization condition (correct induced charge),  $U = I[\omega]$ , so  $\mathbf{F}_i = -\nabla_{\mathbf{r}_i} I[\omega]$ . We can use either equation to calculate force, we did that in fact to validate our results. However, in the implementation,  $\mathbf{F}_i = -\nabla_{\mathbf{r}_i} U$  would be easier since  $\nabla_{\mathbf{r}_i} I[\omega]$  contains extra terms to calculate in both real and reciprocal space.

$$(2.51) \quad \mathbf{F}_i = -\nabla_{\mathbf{r}_i} U = -q_i \sum_{j=1}^N \nabla_{\mathbf{r}_i} G(\mathbf{r}_i, \mathbf{r}_j) \frac{q_j}{\epsilon_j} - q_i \sum_{m=1}^M \nabla_{\mathbf{r}_i} G(\mathbf{r}_i, \mathbf{s}_m) \omega_m a_m$$

There are only two terms to calculate. Without further notice, we only consider kspace calculation as usual.

### 2.3.8.1. The 1st term:

$$(2.52) \quad \sum_j \nabla_i G^K(\mathbf{r}_i, \mathbf{r}_j) \frac{q_j}{\epsilon_j} = \frac{4\pi}{V} \sum_{k \neq 0} \frac{e^{-k^2/4\alpha^2}}{k^2} \left( \sum_j \frac{q_j}{\epsilon_j} e^{-i\mathbf{k} \cdot \mathbf{r}_j} \right) e^{i\mathbf{k} \cdot \mathbf{r}_i} i\mathbf{k}$$

Using the structure factor  $S_{ions,\epsilon}$  calculated in previous section, the real part is

$$(2.53) \quad Re \sim \mathbf{k} \left( \sin S_{ions,\epsilon} \cos(\mathbf{k} \cdot \mathbf{r}_i) - \cos S_{ions,\epsilon} \sin(\mathbf{k} \cdot \mathbf{r}_i) \right)$$

### 2.3.8.2. The 2nd term:

$$(2.54) \quad \sum_m \nabla_{\mathbf{r}_i} G^K(\mathbf{r}_i, \mathbf{s}_m) \omega_m a_m = \frac{4\pi}{V} \sum_{k \neq 0} \frac{e^{-k^2/4\alpha^2}}{k^2} \left( \sum_m \omega_m a_m e^{-i\mathbf{k} \cdot \mathbf{s}_m} \right) e^{i\mathbf{k} \cdot \mathbf{r}_i} i\mathbf{k}$$

We define a new term “structure factor of interface charges” here  $S_\omega = \left( \sum_m \omega_m a_m e^{-i\mathbf{k} \cdot \mathbf{s}_m} \right)$ , then the real part is

$$(2.55) \quad Re \sim \mathbf{k} \left( \sin S_\omega \cos(\mathbf{k} \cdot \mathbf{r}_i) - \cos S_\omega \sin(\mathbf{k} \cdot \mathbf{r}_i) \right)$$

To summarize, in order to calculate electrostatic energy (functional) and force, we need three structure factors: traditional one  $S_{ions}$ , structure factor including dielectric environment  $S_{ions,\epsilon}$  and structure factor of interface  $S_\omega$ .

### 2.3.9. Beyond Ewald method

We still need to calculate three structure factors discussed above, only the detail of kspace calculations are different.

### **2.3.10. Non-static interfaces**

We could use the original CPMD method [15].

## CHAPTER 3

**Surface Polarization Effects on Ion-Containing Emulsions**

This chapter applies the variational method to solve surface polarization in a real physics problem. The content of this chapter is based on the following publication:

- Meng Shen, Honghao Li, and Monica Olvera De La Cruz. "Surface Polarization Effects on Ion-Containing Emulsions." *Physical Review Letters* 119, no. 13 (2017): 138002.

**Abstract**

Surface polarization in ion-containing heterogeneous dielectric media such as cell media and emulsions is determined by and determines the positions of the ions. We compute the surface polarization self-consistently as the ions move and analyze their effects on the interactions between electro-neutral, ion-containing droplets using coarse-grained molecular dynamics simulations based on the true energy functional. For water droplets immersed in oil, the inter-droplet interaction is attractive, and the surface polarization makes the major contribution. By contrast, for oil droplets in water, the ion-surface induced charge interaction is repulsive and counteracts the attraction between the ions, leading to a small attractive interaction between the droplets. This research improves our understanding of self-assembly in mixed phases such as metal extraction for recovering rare earth elements and nuclear waste as well as water purification.

### 3.1. Introduction

Aggregation of foreign phases in dielectric media that contain ions is ubiquitous in biological systems, oil refining industry and water purification membranes [4, 17, 18]. Segregation of ion-containing emulsions in organic solvents is particularly important in extraction of rare earths and nuclear waste. In such processes, multivalent ions and their counterions are encapsulated in self-assembled nano-droplets of water immersed in oil. In the case of amphiphiles encapsulating electroneutral water droplets with trivalent ions (such as lanthanides) together with monovalent counterions in oil, for example, the droplets flocculate into clusters [20], and X-ray scattering data reveal long range inter-droplet interactions. A unique feature of these emulsions is the permittivity difference, which gives rise to surface polarization when there is a local electrical field either due to an external field or due to the presence of charges in the system. In order to understand the aggregation of ion-containing emulsions, it is important to study how the surface polarization contributes to the inter-droplet interactions.

All-atom molecular dynamics simulations account for polarization effects. However, it is not easy to extract the underlying interaction mechanism from all-atom simulations, nor to follow the process over long time and length scales. As a result, the role of surface polarization in ion-containing aggregates have remained elusive. Therefore, coarse-grained molecular dynamics (CGMD) simulations that include explicitly surface polarization effects are desired [10]. Recently, surface polarization has been introduced in implicit solvent CGMD simulations using the boundary element method [11, 12, 13], perturbation theory [14] and the variational method [15, 16].

In this research, we use CGMD to investigate the role of surface polarization in the interaction between ion-containing electro-neutral droplets in heterogeneous dielectric media. In contrast to traditional CGMD, this work directly considers interfacial polarization by minimizing the energy functional of surface induced charges [16]. We first simulate two water droplets immersed in an oil medium, each droplet is 1 nm in diameter and encloses cations and anions with stoichiometric ratio (Fig. 3.1), consistent with the observation in all-atomistic simulations for metalloamphiphiles studies [20]. We then simulate the opposite case of two droplets with lower dielectric constant (oil) of the same dimensions immersed in water (Fig. 3.1) to determine the role of surface polarization in settings close to biological conditions such as interactions between bacterial micrompartments including carboxysomes [39]. Trivalent cations and monovalent anions of 2 Å radii are first studied, corresponding to  $\text{Eu}^{3+}$  and  $\text{NO}^-$  studied in experimental measurements [20]. Then we vary the ion size and valency. We model ions explicitly, and we model solvents implicitly. We neglect surfaces [40] and confinement effects [41] on the permittivity of the media. We assume the bulk permittivity is 80 for water, and 5 for oil. The cases we study here are summarized in Table 3.1, where  $\epsilon_1$ : permittivity in droplet 1;  $\epsilon_2$ : permittivity in droplet 2;  $\epsilon_3$ : permittivity in the medium.

Table 3.1. Four cases with different permittivity contrast.

Case ID	Case description	$\epsilon_1/\epsilon_3/\epsilon_2$
(a)	Water droplets in oil	80/5/80
(b)	Oil droplets in water	5/80/5
(c)	Pure water	80/80/80
(d)	Pure oil	5/5/5

### 3.2. Model

The role of surface polarization can be addressed starting from the definition of polarization vector,

$$(3.1) \quad \mathbf{P}(\mathbf{x}) = -\frac{[\epsilon(\mathbf{x}) - 1]\nabla\psi(\mathbf{x})}{4\pi}$$

where  $\epsilon(\mathbf{x})$  is permittivity, and  $\psi(\mathbf{x})$  is electrostatic potential. Gaussian units are used. However, polarization vector is a volume vector in a non-trivial dielectric medium, namely, it is non-zero wherever the electrical field is not zero, making the surface polarization contributions hard to separate from the total electrostatic interactions. In addition, surface polarization is dynamically entangled with the positions of real charges, therefore, it is rather difficult to be calculated and remains unresolved for decades. Fortunately, the induced charge density, which is defined as  $\rho_i(\mathbf{x}) = -\nabla \cdot \mathbf{P}(\mathbf{x})$ , vanishes except when  $\nabla\epsilon(\mathbf{x})$  or  $\rho_r(\mathbf{x})$  is not zero, where  $\rho_r(\mathbf{x})$  is real charge density, i.e. the induced charge is not zero only at dielectric interfaces or at the location of real charges. Therefore, the determination of induced charges enables the separation of surface polarization contributions from total electrostatic interactions.

We obtain the induced charges using a variational method based on the true energy functional of induced charges as discussed in the previous chapter [16, 38]: We emphasize that it is a true energy functional of induced charges. Minimizing the functional solves for the induced charges and gives the true electrostatic energy.

In our CGMD simulations, surfaces are meshed into  $0.0095 \text{ nm}^2$  triangular patches and the induced charges are obtained by minimizing the discretized energy functional. The electrostatic force on the ions is then calculated as the product of ion charge and

the electrical field. The excluded volume of the ions is represented by a shifted repulsive Lennard-Jones potential:  $u_{LJ} = 4\epsilon[(\frac{\sigma}{r})^{12} - (\frac{\sigma}{r})^6] + \epsilon$  for  $r \leq 2^{\frac{1}{6}}\sigma$ , where  $\epsilon$  and  $\sigma$  are the energy and distance parameter, respectively. The encapsulation of the ions by the droplet surface is guaranteed by a shifted repulsive Lennard-Jones potential. The dynamics of ions is advanced following Newton's second law [42]. To simulate the constant temperature ensemble, the system is coupled to a Langevin thermostat at a temperature of 300 K. The timestep is 1 fs. All simulations are run for at least 10 ns.

Including induced charges,  $\rho_i(\mathbf{x})$ , the Poisson's Equation is rewritten as  $\nabla^2\psi(\mathbf{x}) = -4\pi(\rho_r(\mathbf{x}) + \rho_i(\mathbf{x}))$ . Then, the electrostatic potential can be further separated into bulk and surface contributions (see Appendix),

$$(3.2) \quad \psi(\mathbf{x}) = \int_V \frac{\rho_r(\mathbf{x}')}{\epsilon(\mathbf{x}')|\mathbf{x} - \mathbf{x}'|} d^3\mathbf{x}' + \int_S \frac{\omega(\mathbf{x}')}{|\mathbf{x} - \mathbf{x}'|} d^2\mathbf{x}'$$

where  $\omega(\mathbf{x}')$  is surface induced charge density, and the electrostatic energy is expressed in terms of bulk charges and surface induced charges as

$$(3.3) \quad U = \frac{1}{2} \int_V \int_V \frac{\rho_r(\mathbf{x})\rho_r(\mathbf{x}')}{\epsilon(\mathbf{x}')|\mathbf{x} - \mathbf{x}'|} d^3\mathbf{x}' d^3\mathbf{x} + \frac{1}{2} \int_V \int_S \frac{\rho_r(\mathbf{x})\omega(\mathbf{x}')}{|\mathbf{x} - \mathbf{x}'|} d^2\mathbf{x}' d^3\mathbf{x}$$

The first term is the electrostatic interactions excluding the surface charges, and the second term is the contribution that involves surface polarization. To be concise, we refer to the first term in Eq. (3.7) as ion-ion interactions, and the second term in Eq. (3.7) as ion-surface induced charge interactions. However, the factor of  $\frac{1}{2}$  in the second term

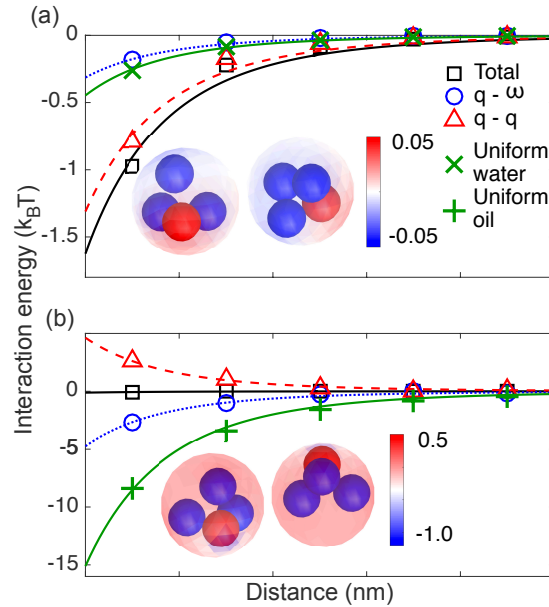


Figure 3.1. Ion-ion (blue circles, fit in blue dotted lines), ion-induced charge (red triangles, fit in red dashed lines) and total (black squares, fit in solid black lines) inter-droplet interactions as a function of inter-droplet distance (a) between water droplets immersed in oil and (b) between oil droplets immersed in water. Inter-droplet interaction with uniform water permittivity (green crosses and fit in green solid lines in (a)) and with uniform oil permittivity (green pluses and fit in solid lines in (b)). Insets are snapshots of the simulations. Red means positive charges, and blue means negative charges.

indicates that this term contains not only real charge-induced charge interactions, but also induced charge-induced charge interactions.

### 3.3. Results and Discussion

It is known that surface polarization is determined by ion distribution, and surface polarization also affects ion distribution. The physics behind this intertwined relation is hardly understood without being able to separate the inter-droplet interactions into ion-ion interaction and ion-surface induced charge interaction. Fig. 3.1 shows the total,

ion-ion and ion-surface induced charge interactions for the four cases (a) - (d) in Table 3.1. Fig. 3.1(a) shows that in case (a), the ion-surface induced charge interaction between the droplets contributes about 80% to the total inter-droplet electrostatic attraction at an inter-droplet distance of 11 Å. The total inter-droplet interaction is about 1.0 k<sub>B</sub>T, close to SAXS measurement in experiments [20]. The interaction energy decays with  $r^{-6}$ , where  $r$  is the distance between the two droplets (see fit curves in Fig. 3.1). This result shows that surface polarization enhances the inter-droplet attraction for water droplets in oil. To understand this enhancement, we notice that the surface induced charge adjacent to positive ions is positive, and vice versa, as is shown in the snapshot in the inset of Fig. 3.1(a) as well as the supplementary video S1 in the original paper [1]. That ions induce same sign charges can be understood by expanding in spherical harmonics induced charges in a single sphere,

$$(3.4) \quad \omega(R, \theta) = \frac{q(\epsilon_{in} - \epsilon_{out})}{4\pi\epsilon_{in}} \times \sum_{l=0}^{\infty} \frac{(l+1)(2l+1)d^l}{[l(\epsilon_{in} + \epsilon_{out}) + \epsilon_{out}]a^{l+2}} P_l(\cos \theta)$$

where  $\omega$  is the surface induced charge,  $q$  is the charge of an ion,  $R$  is the radius of the sphere,  $d$  is the distance from the ion to the center of the sphere,  $\theta$  is the polar angle,  $l$  is the order of each term in the expansion, and  $\epsilon_{in}$  and  $\epsilon_{out}$  is permittivity inside and outside the sphere, respectively. Eq. (3.4) shows that the induced charges are of the same sign as the ion inside the sphere when  $\epsilon_{in} > \epsilon_{out}$ . Consequently, the induced charges increase the total dipole moment formed by the real charges in each droplet, which enhances the inter-droplet attraction.

By contrast, in case (b), the ion-surface induced charge interaction between the droplets is repulsive, while the ion-ion interaction between the droplets is still attractive (Fig. 3.1(b)). These two types of interactions counteract each other, leading to a very small inter-droplet attraction (Fig. 3.1(b)). As shown in the inset in Fig. 3.1(b) and supplementary video S2 in the original paper [1], the surface induced charges are of the opposite sign as the charge of the ion adjacent to the interface grids, which cancels out the dipole moment formed by the ions within the droplet. This is consistent with the spherical harmonics expansion approximation in Eq. (3.4).

To reinforce the importance of including surface polarization for the inter-droplet interactions, we perform simulations without considering surface polarization, using uniform permittivity throughout the system and compare with simulations that consider surface polarization. Fig. 3.1(a) shows that when water permittivity is used throughout the system (case (c) in Table 3.1 shown in green crosses in Fig. 3.1(a)), the total inter-droplet interaction is close to the ion-ion interaction between the droplets for water droplets in oil. This is not surprising, considering that only ion-ion interaction exists for simulations with uniform permittivity, and the permittivity inside the droplets in the two cases is the same. This comparison also indicates that using uniform water permittivity underestimates the total inter-droplet interaction for water droplets in oil by a large amount when surface polarization is neglected. Moreover, by comparing case (a) (black squares in Fig. 3.1(a)) with case (d) (green plus signs in Fig. 3.1(b)), we find that simulations with uniform oil permittivity overestimates the inter-droplet interaction by an order of magnitude. We attribute this to the increased electrostatic interaction between ions due to decreased permittivity. The above comparisons indicates that the total inter-droplet

interaction is not simply reproduced by arbitrarily choosing the permittivity inside or outside the droplets.

On the other hand, the comparison between case (b) (black squares in Fig. 3.1(b)) and case (d) (green plus signs in Fig. 3.1(b)) shows that when uniform oil permittivity is used, the total inter-droplet attraction is overestimated for oil droplets in water. Moreover, uniform water permittivity in case (c) also overestimates the total inter-droplet interaction for oil droplets in water.

It is interesting that the inter-droplet interaction for case (d) with uniform oil permittivity is at least twice the inter-droplet ion-ion interaction for oil droplets in water in case (b) (Fig. 3.1(b)). This seems inconsistent with the fact that the permittivity inside the droplets is the same for the two cases, which seems to correspond to similar ion-ion interactions between the droplets for the two cases, based on Eq. (3.7). To understand this difference in ion-ion interactions with or without accounting for surface polarization, we recall that surface polarization not only is determined by the ion distribution, but also determines the ion distribution, and consequently ion-ion inter-droplet interactions. The effect of surface polarization on the ion-ion inter-droplet interaction can be analyzed with dipole-dipole interactions by simply modeling ions in each droplet as one dipole:

$$(3.5) \quad W = \frac{|\mathbf{p}(\mathbf{x}_1)||\mathbf{p}(\mathbf{x}_2)|(\cos \theta_{12} - 3 \cos \theta_1 \cos \theta_2)}{\epsilon |\mathbf{x}_1 - \mathbf{x}_2|^3}$$

where  $W$  is the interaction energy between dipoles  $\mathbf{p}(\mathbf{x}_1)$  and  $\mathbf{p}(\mathbf{x}_2)$ ,  $\theta_{12}$  is the angle between the two dipoles,  $\theta_1$  ( $\theta_2$ ) is the polar angle of dipole 1 (dipole 2) with respect to  $\mathbf{n}$ , the unit vector in the direction of  $(\mathbf{x}_1 - \mathbf{x}_2)$ , and  $\epsilon$  is permittivity where the dipoles are.

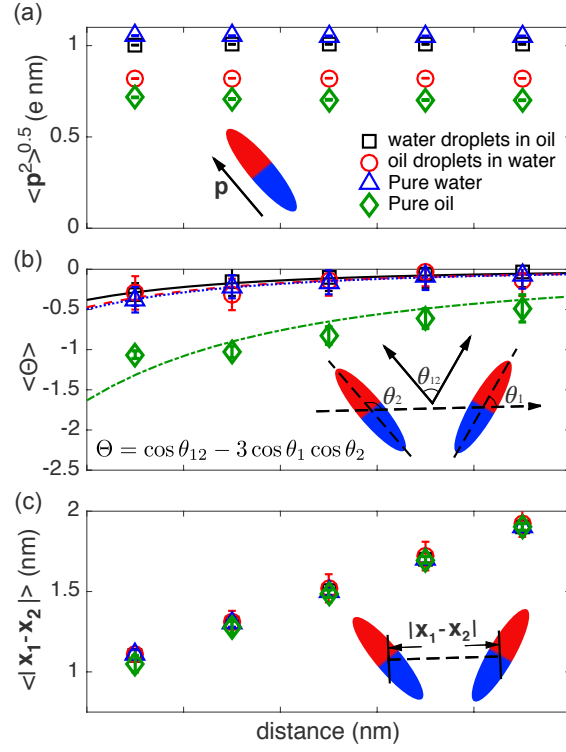


Figure 3.2. (a) the average magnitude of dipole moment, (b) the orientation factor between dipoles and (c) the distance between the center of dipoles formed by ions in each droplet for water droplets in oil (black squares), oil droplets in water (red circles), uniform water permittivity (blue triangles) and uniform oil permittivity (green diamonds). Color online.

Based on Eq. (3.5), the ion-ion interaction between the droplets is determined by four factors in the framework of dipole-dipole interactions: i) the magnitude of the dipoles,  $|\mathbf{p}(\mathbf{x}_1)|$  and  $|\mathbf{p}(\mathbf{x}_2)|$ , ii) the orientation factor of the dipoles  $\Theta = \cos \theta_{12} - 3 \cos \theta_1 \cos \theta_2$ , iii) the distance between the dipoles,  $|\mathbf{x}_1 - \mathbf{x}_2|$ , and iv) the permittivity  $\epsilon$ . While the factor iv) is an input to CGMD, the rest of the factors vary upon ion distribution within the droplets, and are shown in Fig. 3.2 for all four cases (a) to (d).

The average magnitude of the dipole moment formed by ions in each droplet  $\sqrt{\langle \mathbf{p}^2 \rangle}$  is smaller in cases (b) and (d) than cases (a) and (c), as shown in Fig. 3.2(a), because the

electrostatic attraction between ions is stronger in oil than in water, leading to smaller cation-anion distances. Moreover,  $\sqrt{\langle \mathbf{p}^2 \rangle}$  is smaller for water droplets in oil (case (a)) than in uniform water permittivity (case (c)), because ions inside droplets induce surface-induced charges of the same sign, which repel the ions from the surface, making cation-anion distances even smaller. On the contrary,  $\sqrt{\langle \mathbf{p}^2 \rangle}$  is larger for oil droplets in water (case (b)) than in uniform oil permittivity (case (d)), because ions inside droplets induce opposite-sign surface induced charges, pulling ions towards the surfaces.

Fig. 3.2(b) shows that the orientation factor,  $\Theta$ , is much more negative for uniform oil permittivity (case (d)) than the other cases, which has the strongest total inter-droplet attraction in Fig. 3.1. The dipoles are oriented to minimize the enthalpic driven free energy for case (d). We note that  $\Theta$  is 0 for fully random orientations. For cases (a) and (c), the ion-ion electrostatic interactions are normalized by large permittivities, making enthalpic contribution to the free energy less pronounced. Therefore, the dipoles formed by ions in each droplet are more randomly oriented to maximize the entropy. For case (b), the ion-ion attraction between the droplets is canceled out by surface polarization, leading to little enthalpic contribution to the total free energy, therefore, the orientation dependence of the free energy for case (b) is weakened, also leading to random orientations.

The energy functional based CGMD and the separation of inter-droplet interaction enables to understand the physics behind the observed phenomena. The difference in the magnitude and the orientation factor of the dipole moments formed by the ions in each droplet for cases (a) to (d) show that the surface polarization and ion distribution are inter-dependent. Moreover, the average distance between the center of dipoles is more or less of the same length scale as the distance between the droplets. We note

that strictly speaking, ion-ion inter-droplet interactions not only include dipoles but also quadruples, which is important for small inter-droplet interactions, but decay sharply with inter-droplet distance.

### 3.4. Conclusion

Using explicit calculation of induced charges and separation of electrostatic inter-droplet interaction, our work provides a clear understanding behind the intertwined relation between surface polarization and ion distribution. Besides finding strong attractions between droplets with multivalent ions in agreement with all-atom metalloamphiphile extraction studies [20], we find the orientation of the charges in the droplets is strongly affected by the surface polarization and hence the ion-ion interaction between the droplets; these interactions decrease as the ion size and valency decreases (see Appendix). Our studies reveal the role of dielectric mismatch on inter-droplet interactions. While ion-containing oil aggregates in aqueous solutions interact very weakly with each other, much weaker than in the case of simulations that do not include surface polarization, in organic solvents the interactions between water droplets are strongly enhanced due to surface polarization. This understanding helps building meaningful models for analyzing interactions between ion containing emulsions and microcompartments [43], and paves the way for understanding self-assembly of mixed phases for multiple applications.

### 3.5. Appendix

The electrostatic interaction can be calculated from the electrostatic potential  $\psi$  that satisfies Poisson's Equation,  $\nabla \cdot (-\epsilon(\mathbf{x})\nabla\psi(\mathbf{x})) = 4\pi\rho_r(\mathbf{x})$ , where  $\rho_r(\mathbf{x})$  is the real charge

density corresponding to the ions and  $\epsilon(\mathbf{x})$  is permittivity at  $\mathbf{x}$ .  $\epsilon$  is assumed to be piecewise uniform in this work. In terms of the induced charges,  $\rho_i$ , Poisson's Equation is rewritten as:  $\nabla^2\psi(\mathbf{x}) = -4\pi(\rho_r(\mathbf{x}) + \rho_i(\mathbf{x}))$ . Based on Green's theorem in Dirichlet boundary condition, the electrostatic potential is  $\psi(\mathbf{x}) = \int_V \frac{\rho_r(\mathbf{x}') + \rho_i(\mathbf{x}')}{|\mathbf{x} - \mathbf{x}'|} d^3\mathbf{x}'$ , which can be further separated into bulk and surface contributions:

$$(3.6) \quad \psi(\mathbf{x}) = \int_V \frac{\rho_r(\mathbf{x}')}{\epsilon(\mathbf{x}')|\mathbf{x} - \mathbf{x}'|} d^3\mathbf{x}' + \int_S \frac{\omega(\mathbf{x}')}{|\mathbf{x} - \mathbf{x}'|} d^2\mathbf{x}'$$

where  $\omega(\mathbf{x}')$  is the surface induced charge density.

The electrostatic energy is defined as:  $U = \frac{1}{8\pi} \int_V \epsilon(\mathbf{x}) E^2(\mathbf{x}) d^3\mathbf{x}$ . Integration by parts yields  $U = \frac{1}{2} \int_V \rho_r(\mathbf{x}) \psi(\mathbf{x}) d^3\mathbf{x}$ . Substituting Eq. (3.6) for electrostatic potential, the electrostatic energy is expressed in terms of bulk charges and surface induced charges:

$$(3.7) \quad U = \frac{1}{2} \int_V \int_V \frac{\rho_r(\mathbf{x}) \rho_r(\mathbf{x}')}{\epsilon(\mathbf{x}')|\mathbf{x} - \mathbf{x}'|} d^3\mathbf{x}' d^3\mathbf{x} + \frac{1}{2} \int_V \int_S \frac{\rho_r(\mathbf{x}) \omega(\mathbf{x}')}{|\mathbf{x} - \mathbf{x}'|} d^2\mathbf{x}' d^3\mathbf{x}$$

When the ion size is reduced from 0.4 nm to 0.2 nm in diameter, the inter-droplet interaction is much reduced as shown in Fig. 3.3(a), comparing with case (a) studied in this work where both ion diameters are 0.4 nm. We attribute this reduction to the smaller distance between the cations and anions, leading to smaller dipole moment formed by the ions, and consequently smaller induced charges at the surfaces. Fig. 3.3(b) shows that when the cation diameter is 0.5 nm, and anion diameter is 0.3 nm, the inter-droplet interaction is slightly smaller than case (a).

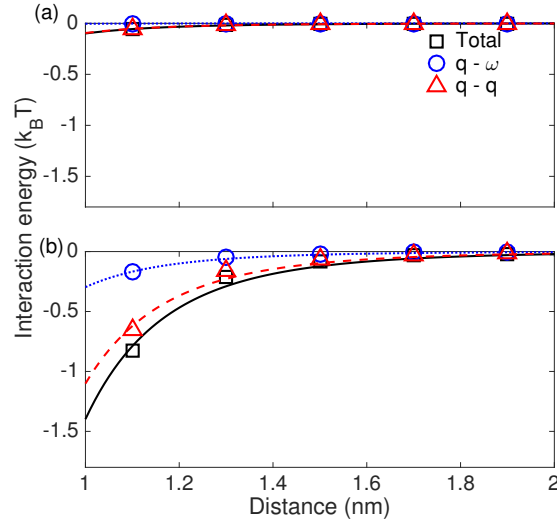


Figure 3.3. Ion-ion (blue circles, fit in blue dotted lines), ion-induced charge (red triangles, fit in red dashed lines) and total (black squares, fit in solid black lines) inter-droplet interactions as a function of inter-droplet distance between the water droplets immersed in oil (a) for ion diameters of 0.2 nm and (b) for cation diameters of 0.5 nm and anion diameters of 0.3 nm.

The ion valence effects are studied for the cases with ion diameters of 0.4 nm. We find that for water droplets immersed in oil, with monovalent ions in the droplets, both the ion-ion interaction and ion-surface induced charge interaction between the droplets are small (Fig. 3.4(a)) comparing with the case with trivalent cations and monovalent anions in case (a). Similarly, for the monovalent ion-containing oil droplets in water (Fig. 3.4(b)), both ion-ion interaction and ion-surface induced charge interaction are smaller than case (b). For trivalent ions, both ion-ion interaction and ion-surface induced charge interaction between the droplets are large for both water droplets in oil (Fig. 3.4(c)) and oil droplets in water (Fig. 3.4(d)) comparing with cases (a) and (b), respectively.

These results indicate that the inter-droplet interaction can be tuned by ion size and ion valence.

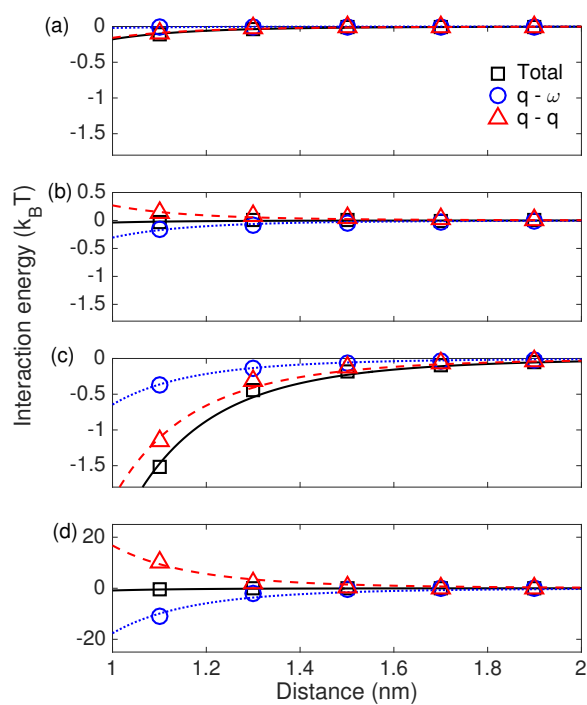


Figure 3.4. Ion-ion (blue circles, fit in blue dotted lines), ion-surface induced charge (red triangles, fit in solid black lines) and total (black squares, fit in solid black lines) inter-droplet interactions as a function of inter-droplet distance for (a) monovalent ions in the water droplets immersed in oil, (b) monovalent ions in the oil droplets immersed in water, (c) trivalent ions in the water droplets immersed in oil, and (d) trivalent ions in the oil droplets immersed in water for ion diameters of 0.4 nm.

## CHAPTER 4

**Asymmetric Electrolytes Near Structured Dielectric Interfaces**

This chapter studies the electrolytes distribution near structured interface, using both our variational method and GMRES. To present a complete story, I have included the figures and data by Huanxin Wu. The content of this chapter is based on the following publications:

- Huanxin Wu, Honghao Li, Francisco Solis, Monica Olvera de la Cruz, and Erik Luijten. "Asymmetric Electrolytes near Structured Dielectric Interfaces". (submitted)
- Honghao Li, Trung D Nguyen, Francisco Solis, and Monica Olvera De La Cruz. "title TBD". (to be submitted).

**Abstract**

The ion distribution of electrolytes near interfaces with dielectric contrast has important consequences for electrochemical processes and many other applications. To date, most studies of such systems have focused on geometrically simple interfaces, for which dielectric effects are analytically solvable or computationally tractable. However, all real surfaces display non-trivial structure at the nanoscale and have, in particular, nonuniform local curvature. Using two recently developed, highly efficient computational methods, we investigate the effect of surface geometry on ion distribution and interface polarization. We consider an asymmetric electrolyte bounded by a sinusoidally deformed surface. We

demonstrate that even when the surface is neutral, the electrolyte acquires a non-uniform ion density profile near the surface. The profile is asymmetric and leads to the effective charging of the surface, which is modulated by the local curvature. The effective charge is opposite to that of the multivalent ion and is larger at concave regions of the surface. We furthermore show that when the surface is charged (e.g. charged amphiphile molecules at interfaces), The electrolyte has the opposite ion distribution compared to the neutral case, here multivalent ions have higher density at concave regions.

#### 4.1. Introduction

The behavior of electrolytes near interfaces has important consequences for surface properties and for processes that take place in their vicinity, such as redox reactions in electrochemical capacitors[44], ion transfer at biomembranes[45], controlling the surface tension of aqueous solutions[46, 47], and establishing colloidal stability via electric double layers[48]. Despite being at the very foundation of modern electrochemistry, complete understanding of electrolyte structure at interfaces is still elusive. Direct probes of the electrolyte structure near an interface have long been challenging in experiments[49, 50]. Theoretical approaches have used the classical Poisson–Boltzmann (PB) model, which offers good descriptions for dilute symmetric electrolyte, but often breaks down at high concentrations, in asymmetric electrolytes, or near strongly charged surfaces.[51, 52, 53] Such breakdown is due to features ignored in the mean field model such as ion size [54, 55], ion hydration [56], dielectric effects [46], and the molecular-scale structure of the liquid solution [57]. Many refinements in the theory have been made, including the modified Poisson–Boltzmann [58], the Born–Green–Yvon approximations [59], the hypernetted

chain [60], charge renormalization [61], and the inclusion of dielectric effects [62]. However, we are still far from a complete description.

Surface structure can have a strong influence on the interfacial properties. In fact, physical roughness should be carefully considered in many applications [63, 64, 65]. For example, the Derjaguin–Landau–Verwey–Overbeek (DLVO) interaction, determined by the repulsive double layer and the attractive van der Waals interaction, differs significantly for rough surfaces compared to perfect smooth ones [66, 67, 68, 69]. Moreover, due to the permittivity mismatch at the interface, ions induce polarization charges on the surface, which is nontrivial for structured surfaces.

Numerical solutions to the polarization problem offer a possible path to the investigation of these structures. However, even with the rapid growth of computational power, previous simulation studies have primarily focused on geometrically simple surfaces where the method of image charges or other techniques can be exploited [70, 71, 72, 73, 74]. One can resort to finite-difference or finite-element methods for structured interfaces. Such algorithms involve discretization of the whole 3-dimensional space, while the induced charges only reside on the surface. Thus, these methods are inefficient for dynamic simulation purposes which require updating the polarization charges at each time step. Recently, boundary element method (BEM) based approaches have gained popularity [11]. Instead of volume discretization, the BEM only discretizes the interface and solves the polarization charges directly, which can be readily utilized in molecular dynamics (MD) simulations. In this paper, we apply (1) the iterative dielectric solver (IDS), which is

solved efficiently via a combination of a fast Ewald summation method and the generalized minimal residual (GMRES) method [12], (2) and the variational method [1, 15, 16] to study the structured interfaces.

The surface structures that are of interest have dimensions in the nanoscale, making first-principle or all-atom simulations unfeasible. We therefore simulate the system with a coarse-grained model with implicit solvent, which captures the finite size effects, the ionic coupling, and the polarization effects. To focus on the dielectric effects, we first study neutral dielectric interfaces, where the electrostatic interaction between the interface and the ions is purely due to surface polarization charges. To complement the simulations we analytically study the system to determine the contribution to the electric potential observed by charges near the interface due to their interaction to the surface. This calculation identifies the origin of the charge accumulation at the surface and its dependence on curvature.

## 4.2. Asymmetric 2:1 electrolytes near solid neutral interface

### 4.2.1. Model

In nature, biomolecular structures, such as membranes and proteins often display complicated surface morphologies. As a first model, we consider a solid–liquid interface with sinusoidal surface topography (see Fig. 4.1). The system is considered as piecewise uniform, with a liquid electrolyte and a low permittivity solid medium. We use the value of  $\epsilon_s = 2$  for the solid, representing materials such as lipid bilayers[75, 76, 77]. The local height of the solid-liquid interface is described by the equation  $z = A \cos(2\pi x/\lambda)$ , where  $A$  is the amplitude of the height oscillation and  $\lambda$  is its wavelength. We start from

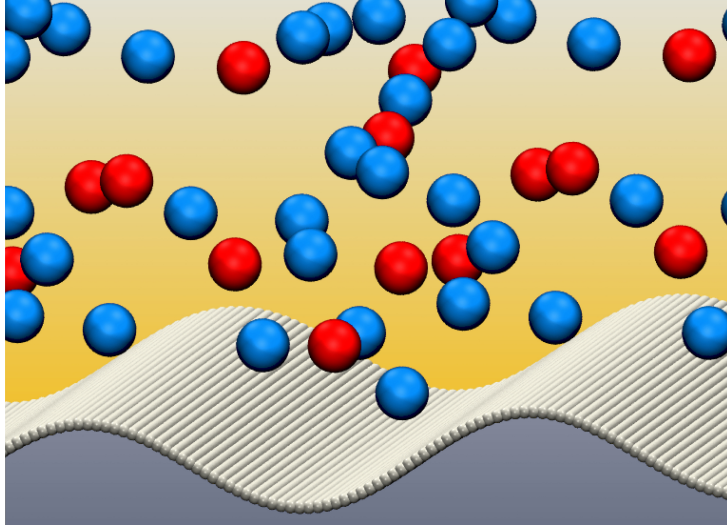


Figure 4.1. Primitive model of an asymmetric electrolyte near a neutral sinusoidal dielectric interface. The positive divalent (red) ions the negative monovalent (blue) ions are immersed in continuum water with relative permittivity  $\epsilon_m = 80$ . The medium below the interface has relative permittivity  $\epsilon_s = 2$ . Apart from the polarization charges, the ions also interact with the surface via the shifted–truncated Lennard–Jones potential.

a configuration of  $A = \sigma$  and  $\lambda = 10\sigma$  for our discussion and later vary the amplitude and the surface structure. Since the roughness length scale of our surface is much larger than the water molecule size, we treat the background solvent as an implicit dielectric continuum of relative permittivity  $\epsilon_m = 80$ . The interface is discretized into a curved rectangular mesh. To capture the excluded volume effects and the atomistic nature of the surface, each mesh point interacts with the ions via the shifted–truncated Lennard–Jones (LJ) interaction. The distance between adjacent mesh points is  $0.2\sigma$ . Such fine mesh also guarantees less than  $10^{-3}$  error in the force calculation of the IDS for worst configurations when ions are closest to the surface. We model the hydrated ions as equal size spheres of diameter  $\sigma = 7.14\text{\AA}$  with point charges of valence  $Z_i$  embedded in their centers.

Since for symmetric electrolytes, dielectric effects are the same for both ion species, it is more interesting to explore the behavior of asymmetric electrolytes. We carry out simulations of 2:1 electrolytes at 50 mM concentration. Slab simulation box of dimension  $10 \times 10 \times 100\sigma^3$  is used with periodicities in both  $x$  and  $y$  directions. The dielectric interface is centered at  $z = 0$ . The electrolyte only stays in upper half of the box. The slab height is sufficiently high to eliminate the boundary effects. Using a Langevin thermostat with damping time  $20t_0$ , where  $t_0 = (m\sigma^2/k_B T)^{1/2}$  is the LJ unit time with  $k_B T$  the Boltzmann factor and  $m$  the ion mass, The system is kept at room temperature with Bjerrum length  $l_B = \sigma$ .

#### 4.2.2. Mean-field model

To better understand the features observed in the simulations we analyze the properties of the surface polarization for a single ion of valence  $Z$  near the interface. These results indicate the presence of induced charges and their dependence on curvature. The solution is obtained as a perturbative expansion on the surface amplitude  $A$ . Once the induced polarization charge is determined, the excess energy of the ion due to the polarization effects is given by  $U = Ze\phi_P/2$  where  $\phi_P$  is the electric potential due only to the polarization charges. The Boltzmann weight,  $\exp[-U/k_B T]$  is then used to determine the relative depletion of ions at the interface.

The perturbative approach expands the polarization potential as  $\phi_P = \phi_P^{(0)} + \phi_P^{(1)} + \dots$ , and similar expansions are applied to the charge density and the geometric quantities. The order of a term in the expansion is the power of the modulation amplitude  $A$  that appears in the expression. The zeroth order of this calculation corresponds to the case of

a single ion near a flat interface. In that case, we have  $\bar{\epsilon}\sigma^{(0)} + \epsilon_0\Delta\epsilon\hat{\mathbf{n}}^{(0)} \cdot \mathbf{E}^{(0)} = 0$ . In this flat geometry, the electric field  $\mathbf{E}^{(0)}$  is due only to the single ion as the field created by the polarization charges is parallel to the surface. We have  $\mathbf{n}^{(0)} \cdot \mathbf{E}^{(0)} = Ze(4\pi\epsilon_0)^{-1}(\mathbf{x}' - \mathbf{x}) \cdot \mathbf{n}^{(0)}/|\mathbf{x}' - \mathbf{x}|^3$ , where  $\mathbf{x}'$  is a point at the surface and we take the ion position as  $\mathbf{x} = (0, 0, a)$ . Integration of the Coulomb potential due to the resulting surface charge density gives the standard image-charge potential at the position of the ion:  $\phi_P^{(0)} = (4\pi\epsilon_0)^{-1}(\Delta\epsilon/\bar{\epsilon})Ze/(2a)$ . The resulting energy of the ion is  $U^0 = (4\pi\epsilon_0)^{-1}(\Delta\epsilon/\bar{\epsilon})Z^2e^2/(4a)$ . This expression is positive when the solid phase has a lower permittivity.

The first order term in the expansion of the potential is associated with the deformation of the surface. To simplify its calculation, we consider the limit where the ion is brought to the interface. In addition, we consider first the case where its position coincides with a peak of the deformed surface. Results for other positions follow from this calculation. According to the image-charge result, the energy in this limit is singular but the exclusion of a small region around the ion renders the result finite. We take the excluded region as spherical, with radius  $a$ . That is, we use the original distance of the ion to the surface as the cutoff for the divergent terms. This choice is not very important but simplifies the presentation of the results. The evaluation of the potential retains an explicit dependence on the wavelength, which is the key feature of interest in our analysis. A more complex calculation, maintaining the ion at a finite distance from the interface, gives similar results. In this limit, the first order terms read  $\bar{\epsilon}\sigma^{(1)} + \epsilon_0\Delta\epsilon\hat{\mathbf{n}}^{(1)} \cdot \mathbf{E}^{(0)} = 0$ . Other terms in the expansion of the equation cancel due to the geometry used. The first order term in the expression for the normal is  $\hat{\mathbf{n}}^{(1)} = [(2\pi A/\lambda)\sin(2\pi x/\lambda), 0, 0]$ . Solving for the charge density we obtain  $\sigma^{(1)} = -(\Delta\epsilon/\bar{\epsilon})(2\pi A/\lambda)(Ze/4\pi)x\sin(kx)/(x^2 + y^2)^{3/2}$ . The electric potential

created at the ion location is the integration of this density,  $\sigma^{(1)}$ , times the Coulomb potential  $(4\pi\epsilon_0)^{-1}(x^2 + y^2)^{-1}$ . The potential at the ion position has a leading term  $\phi_P^{(1)} = -(\Delta\epsilon/\bar{\epsilon})A(Ze/4\pi\epsilon_0)(2\pi/\lambda)^2C|\ln(a/\lambda)|$  with  $C$  a positive constant. For positive ions this excess potential is negative. For other positions, the leading term in the potential is approximately  $\phi_P^{(1)} = -(\Delta\epsilon/\bar{\epsilon})A(Ze/4\pi\epsilon_0)(2\pi/\lambda)^2C|\ln(a/\lambda)|\cos(2\pi x/\lambda)$ . We now use the fact that the mean curvature of the surface is  $H = -(1/2)(2\pi/\lambda)^2A\cos(2\pi x/\lambda)$ . The sign of the mean curvature is negative at convex regions such as those around the peaks of the surface. Therefore, our result can be understood as indicating the dependence of the potential as a function of the curvature  $\phi_P^{(1)} = (\Delta\epsilon/\bar{\epsilon})(Ze/4\pi\epsilon_0)(2CH)|\ln(a/\lambda)|$ . We observe that this expression can be used as an approximation for the potential in cases with a different modulation of the surface. The resulting first-order contribution to the interaction energy between ion and surface is  $U^{(1)} = (\Delta\epsilon/\bar{\epsilon})(Z^2e^2/4\pi\epsilon_0)(CH)|\ln(a/\lambda)|$ .

For a particle near the surface the dominant term of its energy is given by its interaction with the polarization charges. We can then write the excess charge density near the surface in terms of the Boltzmann population factor  $\exp[-(U^{(0)} + U^{(1)})/k_B T]$ . Expanding the exponential factor and multiplying by the bulk densities, we obtain an excess charge density near the surface. Within an atomic diameter from the surface, the net accumulated charge per unit area takes the approximate form

$$(4.1) \quad \delta q = -l_B \left[ C_1 - C_2 A a \frac{|\ln(a/\lambda)|}{\lambda^2} \cos\left(\frac{2\pi x}{\lambda}\right) \right] \times \sum_i c_i e Z_i^3.$$

where  $c_i$  is the bulk number density of species  $i$ , and the integration constants  $C_1$  and  $C_2$  are positive according to the functional form of the estimated potentials. The values of the constants can be estimated in terms of the parameters of the system but we note

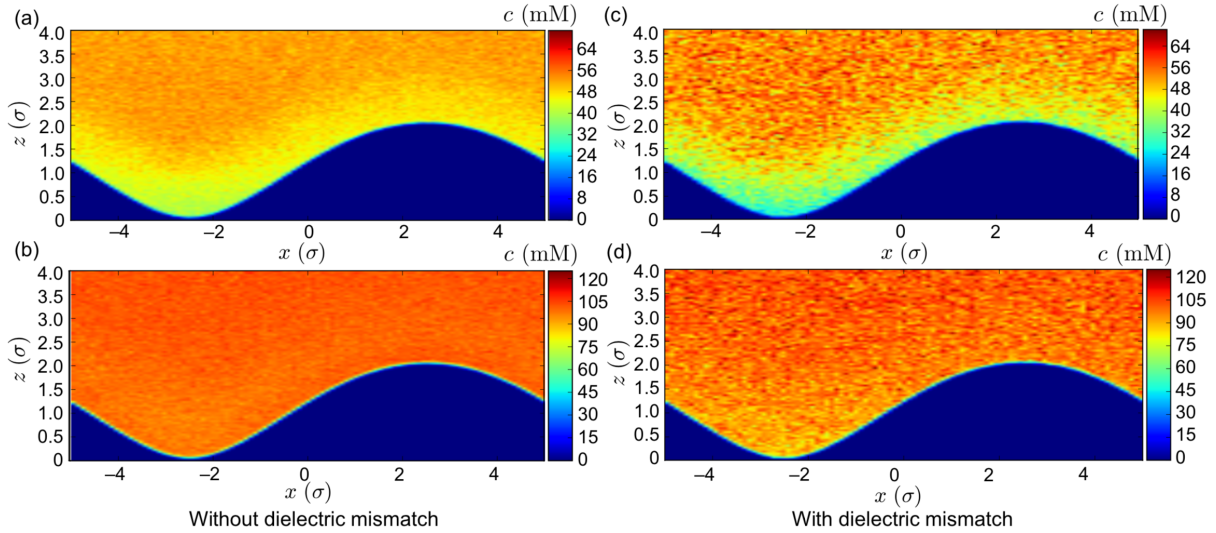


Figure 4.2. Density distributions of a 50 mM 2:1 electrolyte above a structured interface. Left: (a) Divalent and (b) monovalent ion density distributions for a surface *without* dielectric mismatch. Right: (c) Divalent and (d) monovalent ion density distributions for a surface *with* permittivity mismatch 80/2. The polarization charges significantly enhance the surface depletion, in particular for the divalent ions.

that, within the calculation outlined above, they depend on the specific cutoff  $a$  chosen. Equation (4.1) retains the dependence on valencies and characteristic lengths. In particular, we emphasize that the result is not zero for asymmetric electrolytes. The net charge is a result of the asymmetric depletion of ions near the interface. Additionally, the sign of the first order term indicates that the depletion is stronger at concave regions. This result ignores ion correlations and is based on the properties of the direct interaction of individual ions with the dielectric interface. Yet, as shown below, it reproduces the key features of the charge distribution observed in simulations, indicating that it likely represents the dominant contribution.

### 4.2.3. Results and Discussion

Figure 4.2 shows the ion number density for the 50mM 2:1 electrolyte near the modulated surface. In the absence of dielectric contrast the bulk monovalent ion density is almost exactly twice that of the divalent ions; only close to the surface a small depletion occurs, which is more pronounced for the divalent ions. This effect appears as ions near the interface lack a symmetric shell of screening counterions. The asymmetric counterion shell pulls the ions towards the bulk[78, 73]. These results serve as a baseline to assess the effects of the dielectric contrast case.

In the presence of dielectric contrast, we observe a stronger depletion of both charged species, owing to the repulsive polarization charges. The depletion now extends further into the bulk, as can be expected from the long-range nature of the electrostatic interactions. More importantly, since the interaction between the ion and its polarization charge scales as  $Z^2$ , the divalent ions are significantly more depleted near the surface than the monovalent ions. This asymmetry breaks the concentration balance  $c_{+2} = (1/2)c_{-1}$  that is fulfilled in the bulk, so that charge neutrality is violated in the vicinity of the surface, with a net negative charge cloud above the surface (Figure 4.3(a)). Strictly, this effect also occurs in the absence of dielectric mismatch (Figure 4.3(b)) owing to the above-mentioned difference in asymmetry of the counterion shell, but the net charge density is substantially stronger in the presence of dielectric contrast. Also, we observe that the depletion effect is stronger near concave domains of the surface than near convex ones (Figure 4.3(c)). This result is consistent with the results obtained from the analytical calculation.

Along with the net ionic charge density in the electrolyte, the simulations also provide the average induced surface charge density. Although globally the net induced charge of

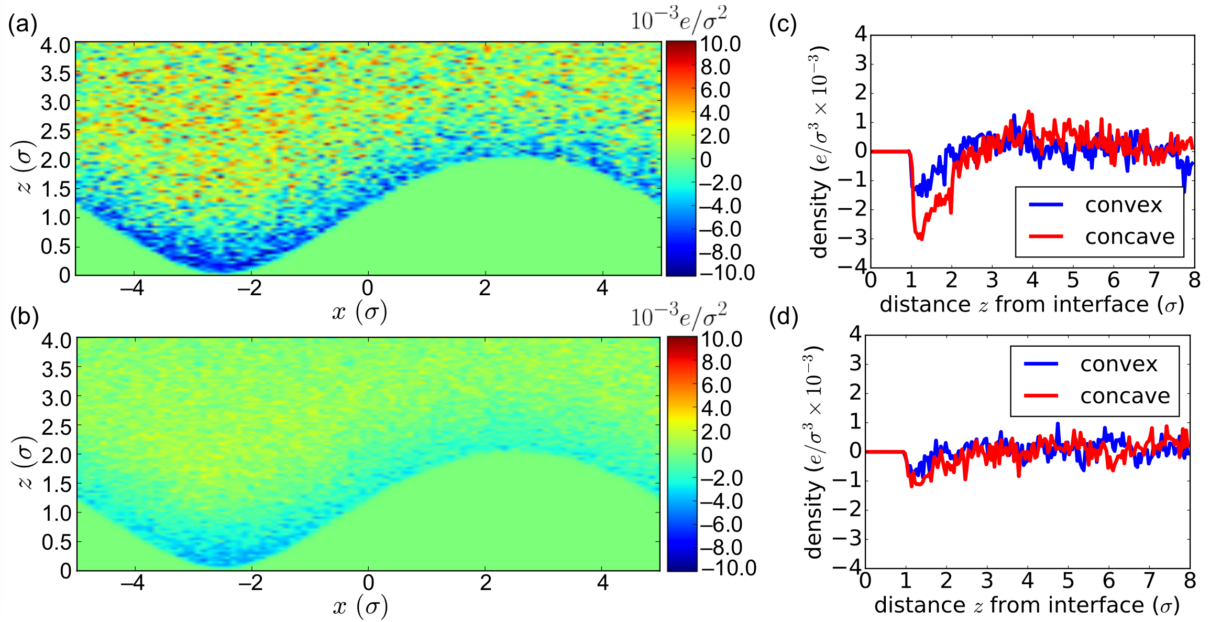


Figure 4.3. Net ionic charge distribution formed by 50 mM 2:1 electrolyte above a neutral structured interface with (a) permittivity mismatch 80/2 and (b) no dielectric mismatch. The net ionic charge density is significantly enhanced by dielectric effects. In addition, the lateral position above the surface also affects the net charge density, as confirmed in panels (c) and (d), with and without permittivity mismatch, respectively. The magnitude of the net charge density is largest above the concave regions (troughs) of the surface. The bin width is  $0.5\sigma$  along the  $x$  direction and  $dz = 0.02\sigma$  in the  $z$  direction. Panels (c) and (d) were obtained using simulations based upon the variational approach of Ref[1].

the interface must vanish, it presents persistent nonzero averages as a function of position. Consistent with the modulation of the ionic charge density, the average induced charge density is positive at convex regions and negative at the concave regions, as illustrated by the time average in Fig. 4.4(a).

To further examine the dependence of the induced charge and ion charge density on surface structure we systematically vary the parameters of the modulated surface. We perform simulations for different modulation amplitudes  $A$  ranging from 0 to  $2\sigma$ .

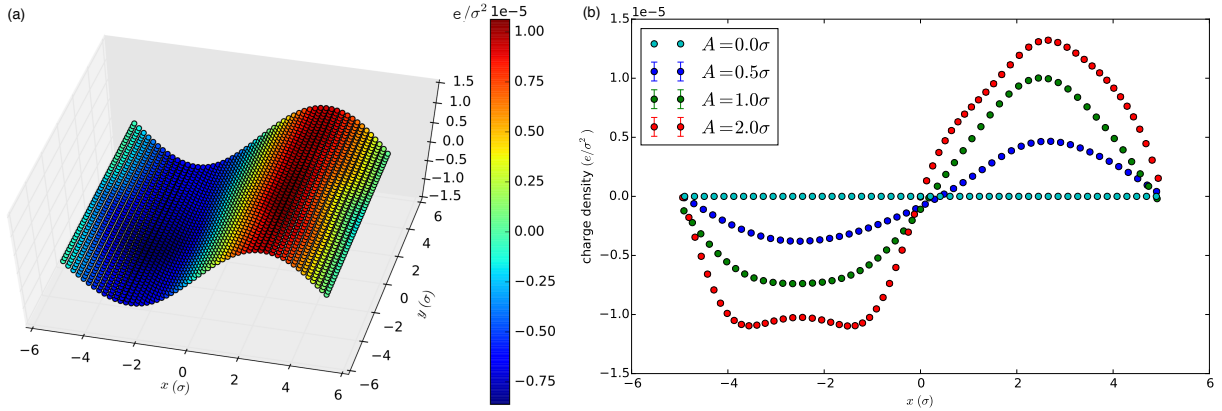


Figure 4.4. (a) Time-averaged surface polarization charge density induced by the spatially modulated ion distribution. (b) Surface polarization charge profile for various amplitudes of the profile.

Figure 4.4(b) shows the induced charge density averaged over the  $y$  direction, along which the properties of the system are invariant. For large amplitudes, we observe that the induced charge density amplitude is larger and varies more rapidly at the peak than in the trough. At low amplitude, the induced charge density itself mimics the sinusoidal variation of the surface, but this similarity breaks down at high amplitude ( $A = 2.0\sigma$ ). This break-down reflects steric effects, where ions cannot reach the bottom of the trough once the gap near the minimum becomes too narrow.

Lastly, the phenomenon we have found in our simulations as well as the PB analysis, of curvature-dependent charge depletion, is generic and not limited to surfaces with modulation in a single dimension. Indeed, it can be generalized to other structures. For example, Fig. 4.5 illustrates the net surface polarization charge pattern of the same 50 mM 2:1 electrolyte above a structured dielectric interface with permittivity mismatch  $80/2$ , but a surface modulation in both  $x$  and  $y$  directions,  $z(x, y) = A \cos(kx) \sin(ky)$ . Similar to our previous results, the valleys of the surface acquire a negative surface polarization

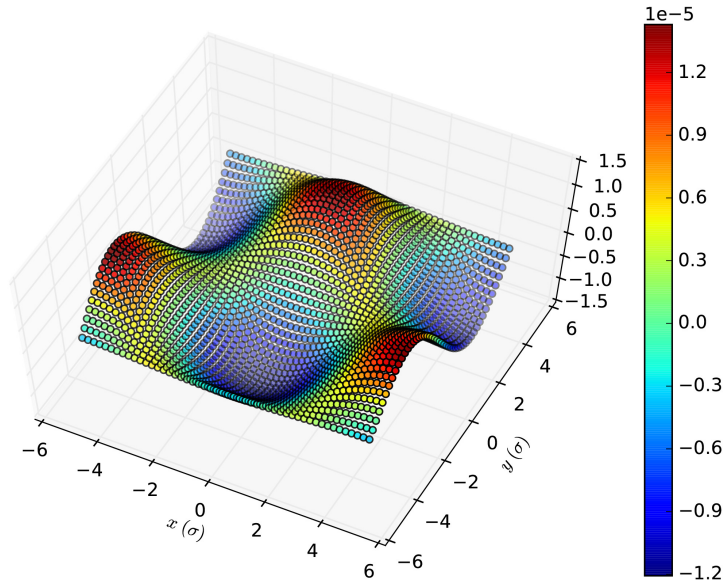


Figure 4.5. Induced surface charge density at a structured dielectric interface that is modulated along both the  $x$  and  $y$  directions. As in the sinusoidal case [Fig. 4.4(a)], the dielectric mismatch is  $80/2$  with a  $50 \text{ mM}$   $2:1$  electrolyte placed above the surface.

charge, whereas the peaks carry a positive induced charge. We note that periodicity of the modulation is not a requirement for the phenomenon to occur.

### 4.3. Asymmetric 3:1 electrolytes near neutral/charged interface

#### 4.3.1. Model

In this study, we consider two dielectric media with the dielectric constants  $\epsilon_1 = 80$  (water) and  $\epsilon_2 = 2$  (e.g. lipid bilayers) respectively. We assume a sharp interface between two dielectric media. For simplicity, a sinusoidal interface is studied, with equation  $z = A \cos(2\pi x/\lambda)$ , where the amplitude  $A = 1.0\sigma$  and the wavelength  $\lambda = 10\sigma$ . To calculate the polarization charge, the interface is discretized into  $80 \times 40 = 3200$  patches. The electrolyte solution is only in the aqueous media. The trivalent cation concentration is

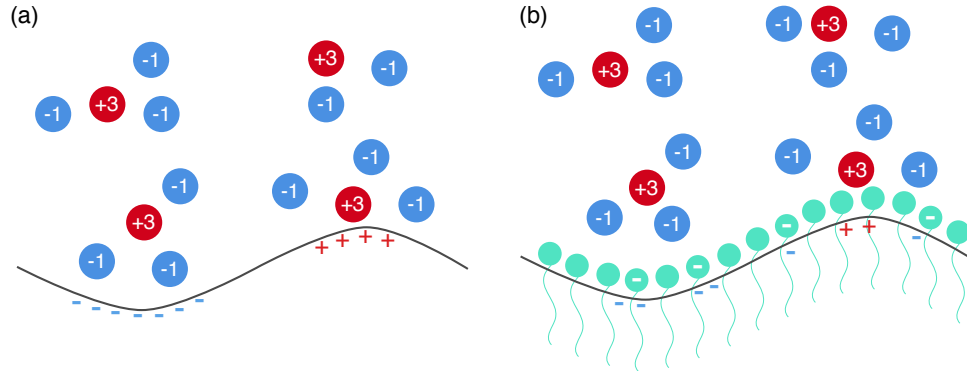


Figure 4.6. The sketch of the studied system. (a) A sinusoidal interface between two different dielectric constants regions ( $\epsilon_1 = 80$  and  $\epsilon_2 = 2$ ). Ions are all in the 1st region. When they approach the interface, the interface will have induced charge thus affect the ions distribution. (b) Another layer of amphiphile molecules are considered. They can move freely along the interface and some of them are negative charged.

50mM. Implicit solvent is considered. We choose the diameter of the ions as  $1\sigma = 0.5nm$ . The simulation box is  $10 \times 10 \times 55$  with the sinusoidal interface at  $z = 0$  and another rigid wall at  $z = 50$  to confine the electrolytes. The simulation is periodic in x, y direction while non-periodic in z direction.

Later we also consider another layer of amphiphile molecules. They can move freely along the interface and some of them are negative charged. We change the fraction of charge and study how this could affect the ion distribution. The molecules are modeled by spherical LJ particles, restrained near the interface via a virtual hard wall layer at distance of  $1.2\sigma$  to the interface.

#### 4.3.2. Curvature effect

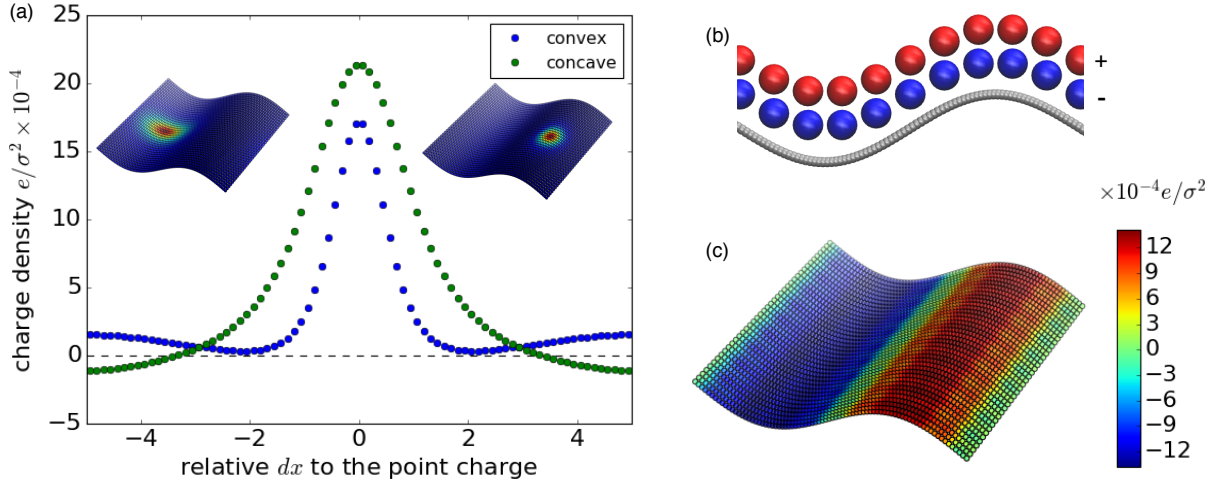


Figure 4.7. (a) A single positive charge is placed  $1\sigma$  above the convex/concave point, the induced charge density along  $x$  direction is plotted. When the charge is placed above the concave point, the induced charge has higher peak, wider shape, and a compensated negative value at convex region. (b) When two layers of uniform charges ( $10 \times 10$  point ions each layer) are placed above the interface with negative layer closer and positive layer further away. (c) the polarization charge is negative at concave region while positive at convex region.

**4.3.2.1. Single charge.** We start from the simplest test case, a single charge near different curvature interface. We found the charge near concave region generates strong polarization on the interface than a charge near the convex region, see Fig. 4.7(a).

The force calculation demonstrated the same result. For a single charge near infinite planar dielectric interface, the force exerted on the charge by the polarization can be easily calculated using image charge method,  $f = \frac{\epsilon_1 - \epsilon_2}{\epsilon_1 + \epsilon_2} \frac{q^2}{4\pi\epsilon_1 r^2}$ . For our case,  $\epsilon_1 = 80$  (where the charge presents) and  $\epsilon_2 = 2$ . We have  $f = \frac{80-2}{80+2} \frac{q^2}{4\pi\epsilon_1 (2\sigma)^2} = 0.2378 \frac{q^2}{4\pi\epsilon_1 \sigma^2}$ ; While the simulation gives  $f = 0.1917 \frac{q^2}{4\pi\epsilon_1 \sigma^2}$  for charge above convex point, and  $f = 0.3271 \frac{q^2}{4\pi\epsilon_1 \sigma^2}$  for charge above concave point. So the interaction for the charge is: concave  $>$  planar  $>$  convex region.

**4.3.2.2. Many charges.** For two layers of uniform charges near the interface, we find that the polarization mainly depends on the closest layer of charges. The surface polarization of concave region has the same sign as the closest layer of charges due to the stronger effect there. To fulfill the total surface charge neutrality, the polarization of convex region has to be opposite. Conclusion: different depletion would result asymmetric polarization for different curvatures.

### 4.3.3. Electrolytes

**4.3.3.1. Trivalent with same size.** The ion distribution is investigated, Fig. 4.8(a)(d) demonstrates a stronger depletion effect of the trivalent cations than that of the monovalent anions. This can be explained by considering different forces experienced by ions near a dielectric boundary[73]: (1) The deformation of the double layer tends to pull ions away from the boundary; (2) The steric interactions tend to push ions against the boundary; (3) The surface charge and polarization charge can attract or repel ions depending on the relative sign of the charges. Since the interaction between the ion and its polarization charges scales with the valence ( $Z^2$ ), the trivalent ions are much more depleted near the interface than the monovalent ions. Similar effect can also be found in divalent systems (previous sections).

We also notice the depletion effect is stronger at concave region than that at convex region, see Fig. 4.8(b). This can be understood since an ion near concave point experiences a stronger repel force than an ion near convex point, as we discussed in previous section. This asymmetric depletion effect can also be observed for monovalent anions, see Fig. 4.8(e). However, it is weaker than the trivalent cation case.

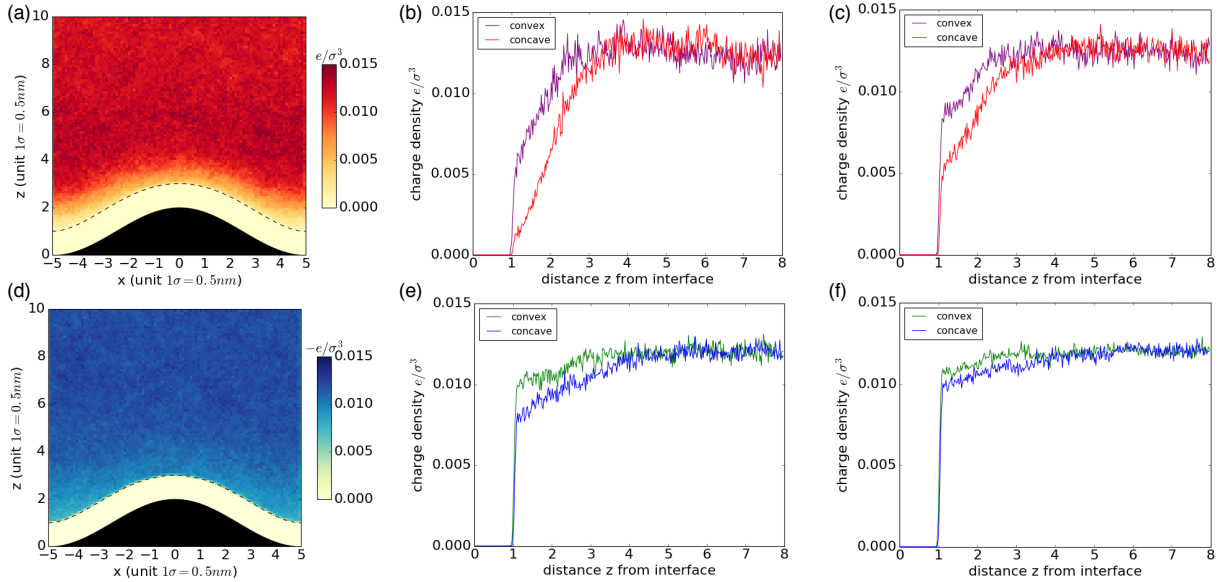


Figure 4.8. Ion distribution. (a) Charge density of positive ions. The interface is denoted by black color, the dashed line represents the closest distance an ion can reach due to the hard-core LJ potential. (b) Charge density of positive ions in the narrow bin (width  $dx = 0.5\sigma$ ) above the convex/concave region. (c) Charge density of positive ions in the narrow bin (width  $dx = 0.5\sigma$ ) above the convex/concave region (system without dielectric mismatch). (d) Charge density of negative ions. (e) Charge density of negative ions in the narrow bin (width  $dx = 0.5\sigma$ ) above the convex/concave region. (f) Charge density of negative ions in the narrow bin (width  $dx = 0.5\sigma$ ) above the convex/concave region (system without dielectric mismatch). To summarize, (a), (b), (d) and (e) are for system with dielectric mismatch while (c) and (f) are for system without dielectric mismatch.

Both of the above effects can be found in a system where there is no dielectric mismatch (e.g. a hard wall interface with both sides  $\epsilon = 80$ ). This proves the deformation of double layer dominates over the steric interactions. However, the depletion and the asymmetric depletion are much weaker.

Fig. 4.9(a) shows the net charge density in the system with dielectric mismatch. It is clear to see the closest layer are negative due to the stronger depletion of trivalent cations

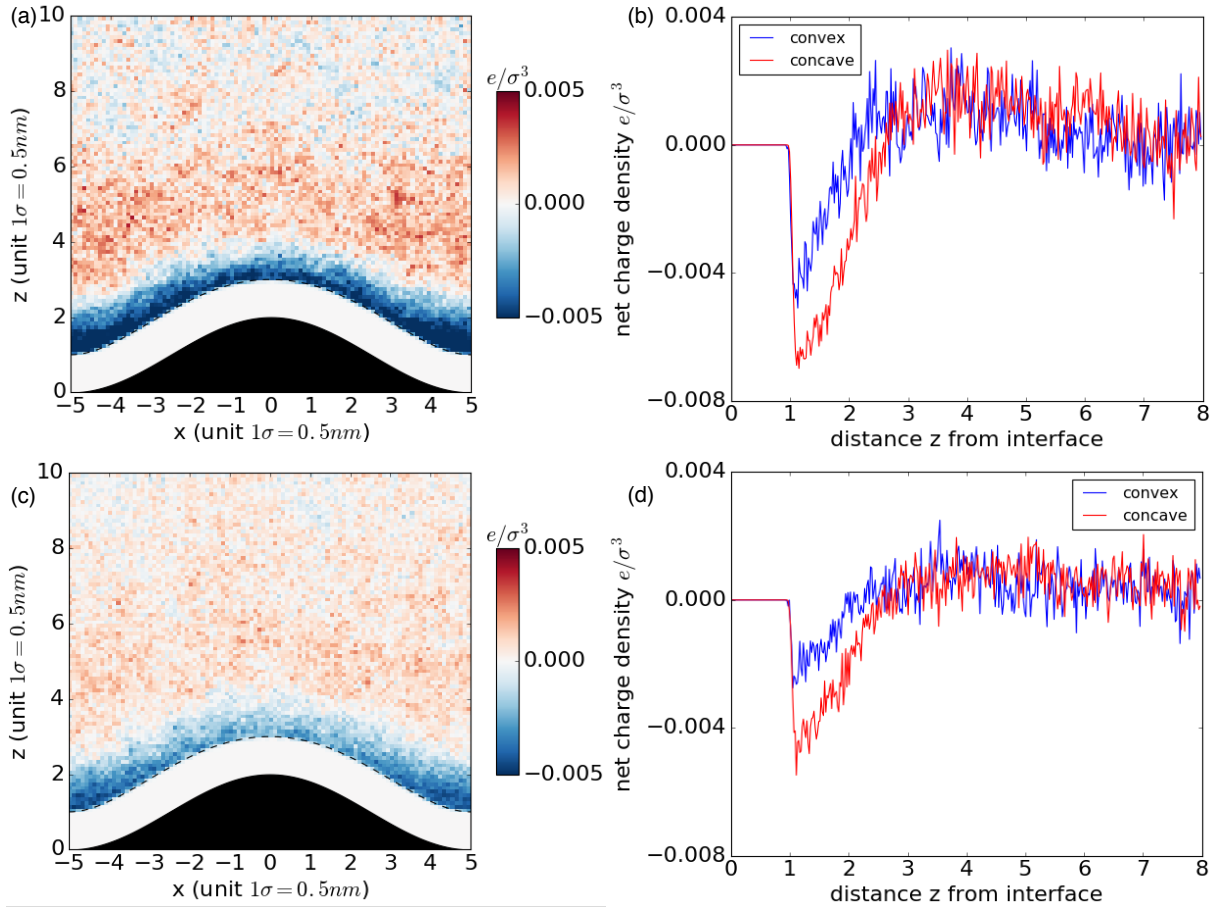


Figure 4.9. Net charge density. (a) Net charge density. (b) Net charge density in the narrow bin (width  $dx = 0.5\sigma$ ) above the convex/concave region. (c) Net charge density in system without dielectric mismatch. (d) Net charge density in the narrow bin (width  $dx = 0.5\sigma$ ) above the convex/concave region (system without dielectric mismatch).

as we discussed above. Fig. 4.9(b) also shows the effect is stronger at concave region than convex region. Fig. 4.9(c)(d) is the comparison results for the system without dielectric mismatch, similar effect but weaker.

Fig. 4.10 shows the induced charge density of the interface averaged over time. The total charge is zero within the error due to the neutrality in the system. However, since the closest layer of negative net charge density. there is a positive polarization at convex

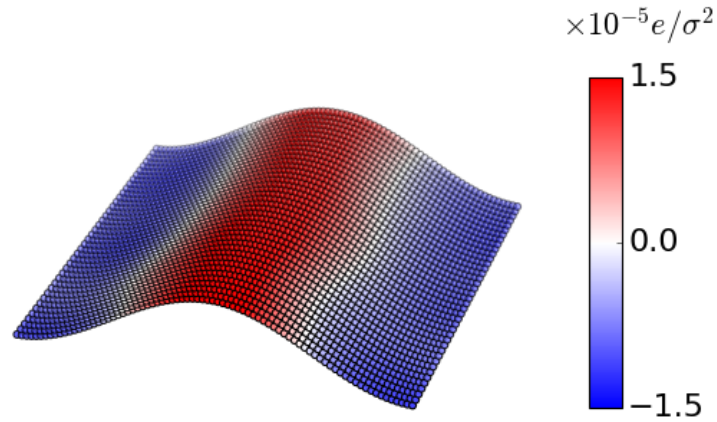


Figure 4.10. Induced charge density on the interface when the dielectric mismatch is present.

region and a negative polarization at concave region. This result agrees with our discussion in previous section, see Fig. 4.7.

Also, in the second layer, trivalent has higher distribution at convex part. This could further enhances the asymmetry.

#### 4.3.4. Molecular layer

**4.3.4.1. Ion distribution for different charge fraction.** Now we consider the system with a layer of amphiphile molecules. Fig. 4.11 illustrates the distribution of trivalent cations above convex/concave region, for different fraction of charge of molecules. We find the depletion still exists when the molecular layer is not charged or weakly charged, but the effect is weaker than the case without molecules. This is because the molecular layer makes the ions further away from the interface, thus reduces the effect. With the fraction of charge increases, the depletion effect disappears. The repulsion changes to attraction. Note that for the attraction at higher fraction of charge, concave region attracts more ions than convex region.

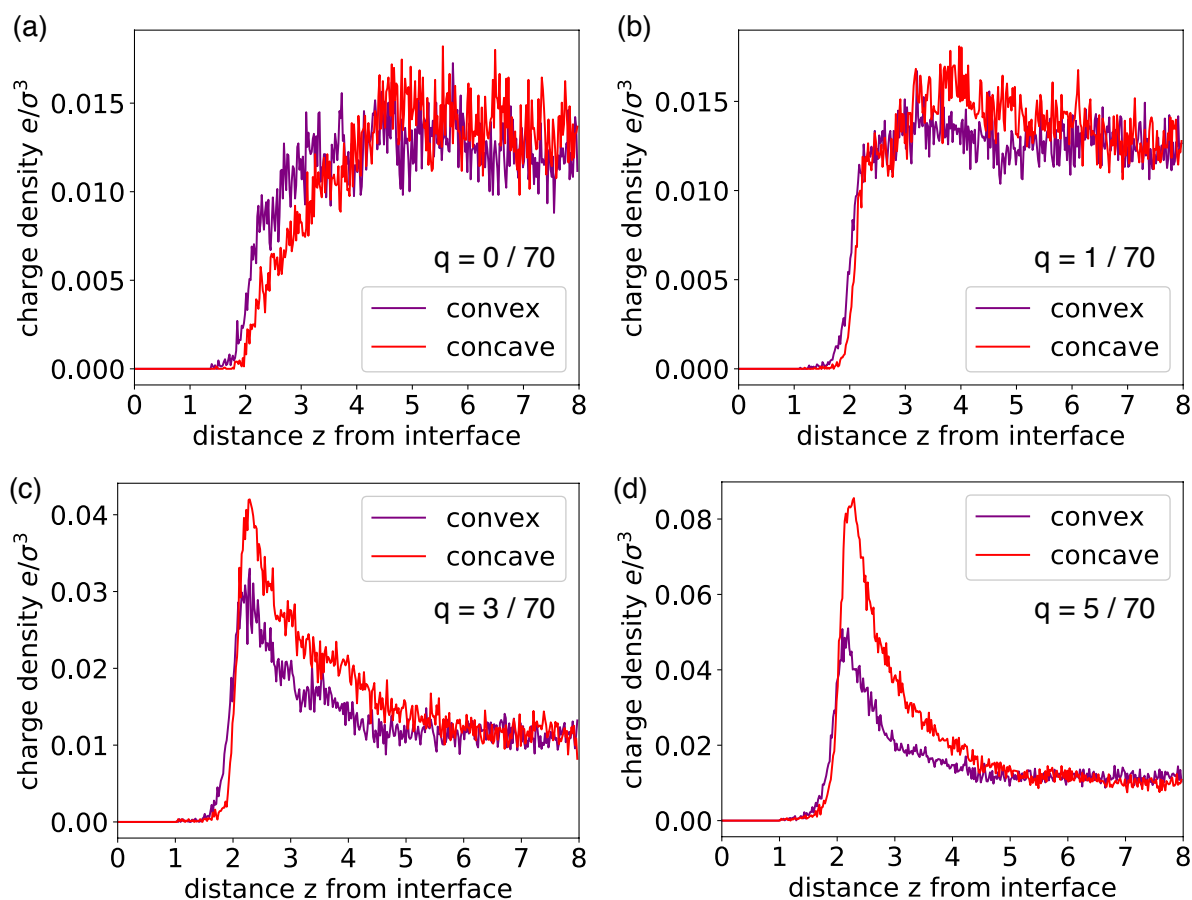


Figure 4.11. Charge density of positive ions in the narrow region above the convex/concave region when the molecular layer is present. (a) None of the 70 molecules is charged. (b) 1 out of 70 molecules is negative charged. (c) 3 out of 70 molecules are negative charged. (d) 5 out of 70 molecules are negative charged.

Actually, we also calculated the ion distribution for planar case, see Fig. 4.12.

#### 4.4. Conclusion

The simulations presented, along with the arguments based on single-ion interactions with the surface, demonstrate that the effect observed is universal. The local curvature of the surface always induces effective surface polarization and net ion charge accumulation

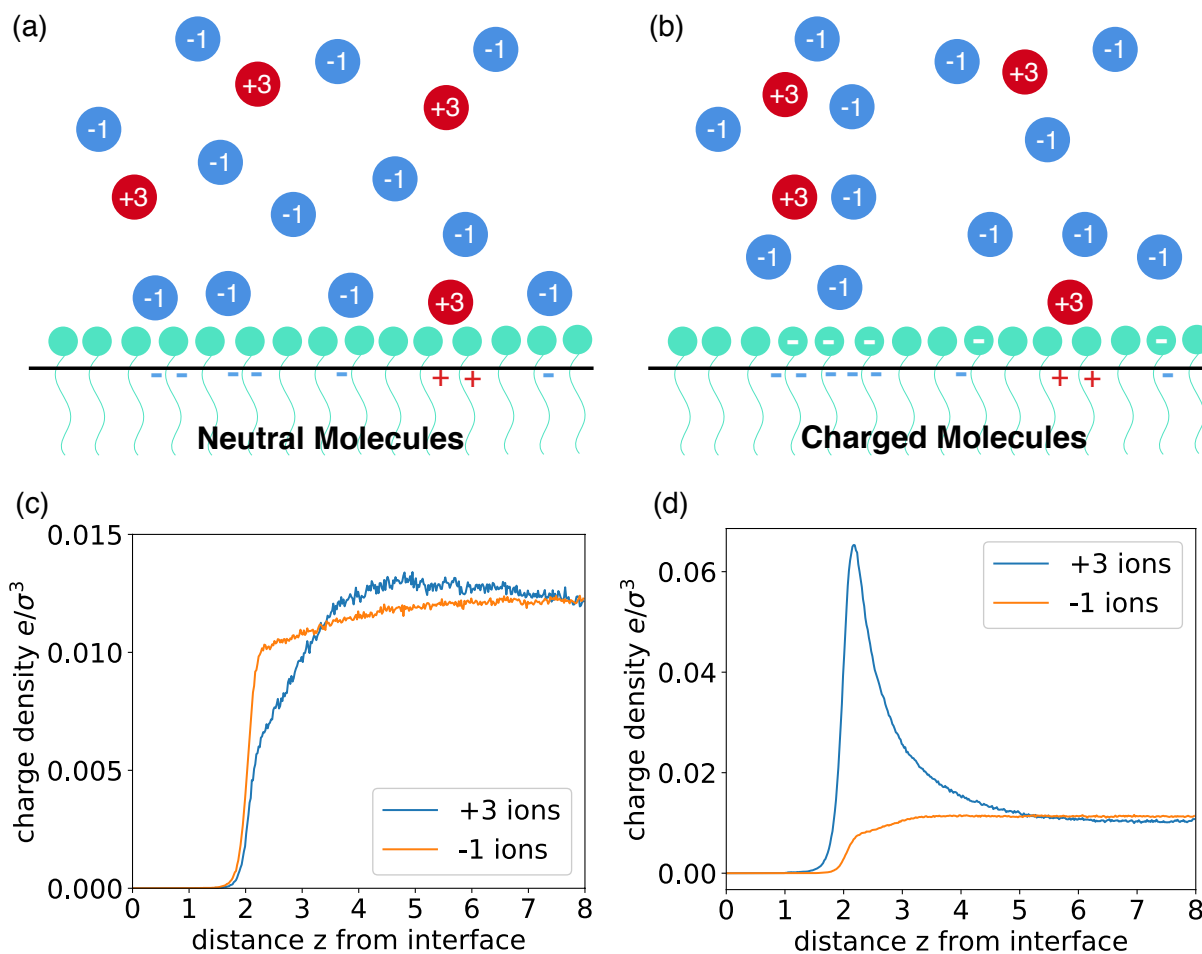


Figure 4.12. Charge distribution for planar case with molecular layer.

in the presence of asymmetric electrolytes. The effect should be observable not only on surfaces that bound an electrolyte, but also at the surface of electrolyte-immersed colloids. Trivalent ions has a stronger symmetry-breaking effect than divalent ions. When there is a layer of charged molecules present at the interface, The ion distribution could be altered. Our findings can be applied to the design of surfaces with useful physicalchemical properties.

## CHAPTER 5

**Interfacial origin of intra-lanthanide selectivity during solvent extraction**

The content of this chapter is based on the following publications:

- Miller, Mitchell; Li, Honghao; Chu, Miaoqi; Yoo, Sangjun; Bu, Wei; de la Cruz, Monica Olvera; Dutta, Pulak "Interfacial origin of intra-lanthanide selectivity during solvent extraction". (submitted)

**Abstract**

Rare earths are fundamental components of modern technologies, and solvent extraction is widely used for recovering and separating these elements from aqueous solutions. Heavier lanthanides are more easily extracted than lighter lanthanides, even though the ions are chemically very similar, but very little is known about the nanoscale processes responsible for this selectivity. Using a floating (Langmuir) monolayer as a model extractant, we have measured the interfacial densities of two lanthanide ions ( $\text{Er}^{3+}$  and  $\text{Nd}^{3+}$ ) using X-ray fluorescence near total reflection (XFNTR). When a single lanthanide is present, the interfacial concentration shows a near-step-function dependence on bulk solution concentration. The threshold bulk concentration of erbium ( $Z=68$ ) is an order of magnitude lower than that of neodymium ( $Z=60$ ). When both ions are present in the

bulk solution, Er segregates preferentially to the interface even when its bulk concentration is lower. Using a theoretical model and Monte Carlo simulations, we find that electrostatic effects arising from the inhomogeneity of the interfacial medium can explain both the unusual step-function dependence and the large difference in the threshold bulk concentrations. Our results imply that the extractant-rich interface plays an essential role in separating lanthanides during solvent extraction.

### 5.1. Introduction

Solvent extraction [19], also known as liquid-liquid extraction, is a common technique used to remove a specific ion or compound from an aqueous solution. The process works by bringing together two immiscible liquid phases, an aqueous phase containing the dissolved ions and another liquid phase, usually with specialized extractant molecules at the interface. The desired ion is then preferentially transferred to the non-aqueous solvent, resulting in a target-metal-rich solvent phase and a waste aqueous phase. This method has applications in mining and refinement of rare earth metals, in nuclear fuel reprocessing (actinide separation), and in the cleanup of toxic waste [19, 20, 21, 22].

Despite decades of research into the mechanics and development of solvent extraction [20, 23], and its widespread use in industry, there is very little understanding of many fundamental aspects of the process. One example is the lanthanides' nearly ubiquitous trend of increased extraction efficiency as a function of atomic weight [19]. This phenomenon is well documented using dozens of different extractant molecules, and can be very useful because the source minerals typically contain multiple lanthanides. However, extraction efficiency is a macroscopic measurement and there are a multitude of microscopic

and nanoscale processes that could work together and also compete with one another to produce this outcome. The chemistry of f-element separation [79] is highly complex. Metal hydration before and after complexation with extractant molecules [80], the presence of other salts [79, 81, 82], and even the nanoscale structure of water molecules [83] could all have competing or cooperating effects on the overall extraction of a given metal. The adsorption of amphiphilic extractant molecules onto the aqueous-organic interface will affect solvent extraction [84]. Behaviors like the rate of chemical reaction between extractants and metal ions to form complexes, the speed of diffusion from the interface to the bulk rate could also affect the net extraction efficiency [84]. These behaviors may or may not be attributable to the widely known “lanthanide contraction” [85]. There is much debate as to which processes or interactions are most important in determining intra-lanthanide selectivity. The general view is that bulk interactions dominate and that the extractant-rich interfaces are only of interest in the transport of the different species. However, while there are many studies of bulk solvent extraction [86, 87, 88, 89], surprisingly few experiments have focused on the interface between liquid phases.

The difficulty in experimentally probing the surfactant-liquid interface is a major reason for the scarcity of studies. However, over the past five years, nanoscale and in situ measurements of model systems have yielded important information regarding real solvent extraction processes. Early x-ray studies of isolated (no extractant analogue) aqueous lanthanide solutions showed that there is a dramatic difference between the coordination of erbium near the surface and in the bulk [90, 91]. Another study of the same system revealed that there is a nonmonotonic density profile perpendicular to the liquid surface, suggesting the spontaneous formation of high density ionic layers at the surface [92].

More realistic model systems in which an aqueous solution is completely submerged in dodecane extractant solution [93, 94], create a static interface that can be probed with x-rays. This system showed several different morphologies of ion-extractant complexes, depending on what ion is present in the aqueous phase. Further, interfacial lanthanides have recently demonstrated unexpected trends in lateral ordering structure as a function of atomic number [95].

While these studies enhance our understanding of the interface, they do not address the question of why and where intra-lanthanide selectivity occurs during the extraction process. Using X-ray fluorescence near total reflection (XFNTR; see the original paper for details) at the Advanced Photon Source, Argonne, IL, we have measured the interfacial densities of two lanthanides adsorbed at amphiphile monolayers as functions of their concentration in the bulk solution. We find that the heavier lanthanide was much more strongly attracted to the interface. We explain this unexpected finding with a theoretical model that shows that this selectivity results from the fact that the interface is inhomogeneous.

## 5.2. Results and Discussion

### 5.2.1. Experiment

We first studied the interfacial lanthanide density when the only lanthanide present in the aqueous subphase was  $\text{Er}^{3+}$ . The floating monolayer was octadecylphosphonic acid (ODPA) chosen because phosphates are often used as extractants. With bulk solution concentrations between  $10^{-4}\text{M}$  and  $\sim 5 \times 10^{-8}\text{M}$  of  $\text{ErCl}_3$ , the surface density of erbium

measured by XFNTR was roughly constant, at about  $0.016 \text{ ions}/\text{\AA}^2$ . However, at concentrations, below  $\sim 5 \times 10^{-8} \text{ M}$  the surface density drops quite sharply to  $< 0.001 \text{ ions}/\text{\AA}^2$ , essentially zero. This is shown in Fig. 5.1; the line through the data is a theoretical prediction, to be discussed later.

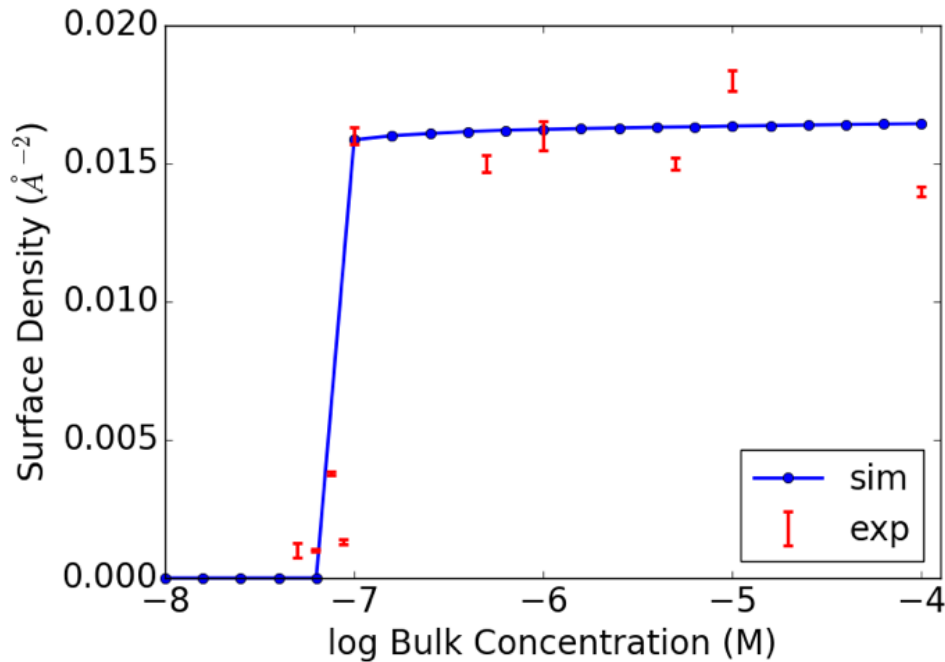


Figure 5.1. Surface density of Er (red error bars) vs. bulk concentration in the aqueous phase. The line connects theoretically calculated values (blue dots) using simulation parameters:  $l_B^+ = 1.769l_B^{water}$ ,  $l_B^i = 1.963l_B^{water}$ , with interlayer distance  $d = \sigma = 0.5 \text{ nm}$ . See Simulations and Theory Results section for an explanation of these variables, and other details.

Solutions of  $\text{NdCl}_3$  likewise show an attraction to ODPA monolayers, but to a much lesser extent (Fig. 5.2). The average surface density at higher bulk concentrations is  $0.013 \text{ Nd}/\text{\AA}^2$ , slightly lower than that of Er at equivalent concentrations. However, at  $5 \times 10^{-7} \text{ M}$

$\text{NdCl}_3$  and below, the surface density decreases to zero. Thus the bulk concentration thresholds of these similar ions differ by a full order of magnitude.

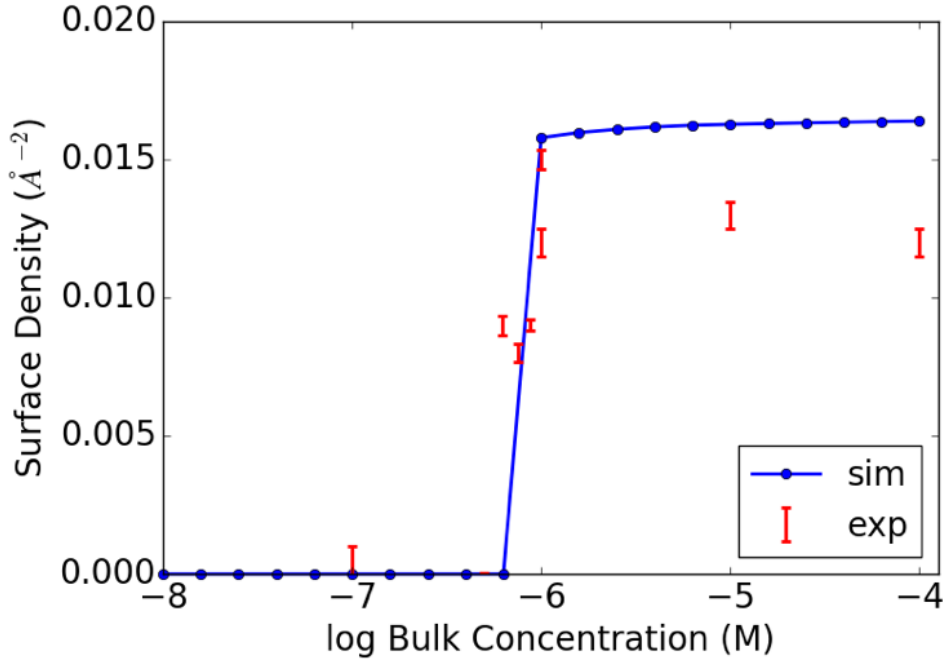


Figure 5.2. Surface density of Nd (red error bars) vs. bulk concentration in the aqueous phase. The line connects theoretically calculated values (blue dots) using simulation parameters:  $l_B^+ = 1.769l_B^{water}$ ,  $l_B^- = 1.963l_B^{water}$ , with interlayer distance  $d = 1.07\sigma = 0.535\text{nm}$ . See Simulations and Theory Results section for an explanation of these variables, and other details.

Finally, we investigated mixtures of Nd and Er in aqueous solution. When there are equal concentrations of Nd and Er ( $10^{-4}\text{M}$  of  $\text{NdCl}_3$  and  $\text{ErCl}_3$ ), there is five times as much Er compared to Nd at the interface (Fig. 5.3). When the Er concentration is reduced while the Nd concentration is held constant, there is a continuous (not sudden) decrease in Er surface density and a roughly equal increase in Nd density (i.e. the total surface density is approximately constant). But to have a 50% reduction in Er surface

density (which is also the point at which Er and Nd are present in equal quantities at the surface), the bulk Er concentration must be lowered by an order of magnitude.

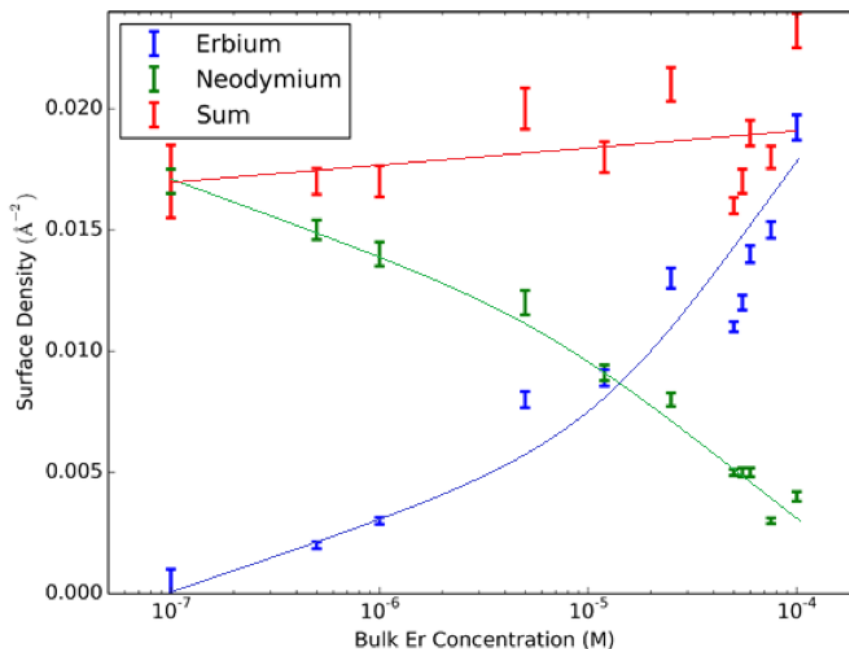


Figure 5.3. Surface densities of  $\text{Er}^{3+}$  and  $\text{Nd}^{3+}$  when the bulk Er concentration is varied (Nd concentration fixed at  $10^{-4}\text{M}$ ). The lines are guides to eye.

These fluorescence measurements can be used to calculate an average number of ions per ODPA molecule. A previous report [95] showed that ODPA molecules have an area of  $\sim 21\text{\AA}^2$  when spread over lanthanide salt solutions. In pure solutions, the data reported here mean that neodymium and erbium have an average area of  $77\text{\AA}^2$  and  $63\text{\AA}^2$  per ion respectively. Thus there are approximately four ODPA molecules for every  $\text{Nd}^{3+}$  ion and three ODPA molecules for every  $\text{Er}^{3+}$  ion attracted to the interface. When both ions are dissolved in the subphase, the total surface density remains almost constant while the

relative bulk concentrations are varied. If one considers this a measure of the average area for either an erbium or neodymium ion, we find an area of  $56\text{\AA}^2$ . This is close to the density observed with erbium by itself, i.e. there is approximately 1 ion (either erbium or neodymium) per 3 ODPA molecules. These results are unexpected since both erbium and neodymium have the same valence, and  $\text{pK}_a$  values indicate that ODPA molecules have completely dissociated one hydrogen and have only about 5% dissociation of the second. Therefore, the Er numbers seem reasonable, while there is a mismatch in charge with neodymium, with cations providing 3+ and ODPA molecules providing 4- in the same area. However, note that XFNTTR does not measure total charge and cannot detect  $\text{H}^+$ ,  $\text{OH}^-$ ,  $\text{Cl}^-$  etc. Moreover, one cannot assume that the local pH at the interface is the same as that in the bulk [96].

## 5.2.2. Simulation & Theory

**5.2.2.1. Monte Carlo Simulation.** The surface of a liquid, or the interface between two liquids, is a complicated environment. We cannot assume a homogenous dielectric medium, with an overall dielectric constant. The dielectric environment could change dramatically in the vicinity of interface [97, 98, 99, 100], and the presence of dissolved ions also results in a different bulk dielectric constant [101]. The hydration shells of different lanthanide ions add to the complications. Since the electrostatic interactions are crucial in our system, we need to introduce dielectric inhomogeneity to capture the fundamental physics. Full atom simulations are considered the best tool to study dielectric inhomogeneity, but this method lacks a mechanism to dynamically change the dissociation state of molecules. Therefore, the adsorption of lanthanide ions on surfactant monolayer

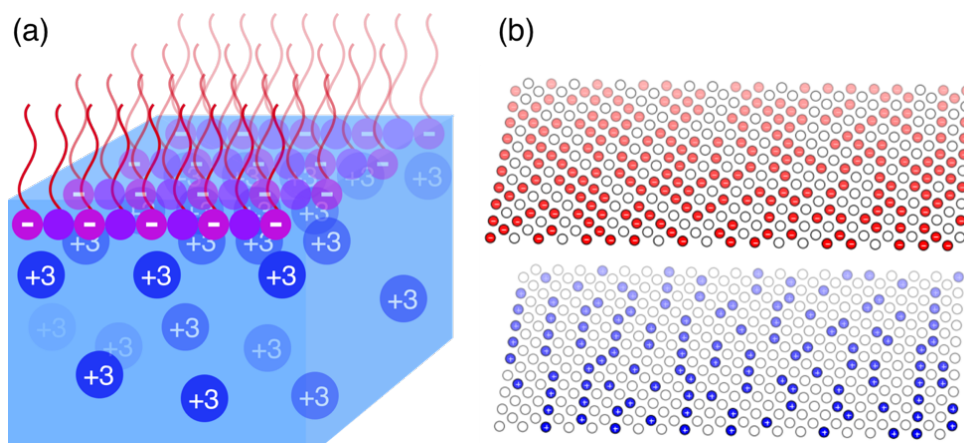


Figure 5.4. (a) Schematic diagram of the system being simulated. (b) Sample Monte-Carlo simulation setup (smaller system  $20 \times 20$  here for clarity), upper(lower) hexagonal lattice layer is molecules(lanthanides), red is charged molecules, blue is absorbed lanthanides; white is neutral molecules or empty sites of lanthanides. The separation in the  $z$  direction is exaggerated here for clarity.

near interface as a function of concentration were examined using Monte Carlo simulations. According to the Henderson-Hasselbach equation, the fraction of dissociated rate  $\alpha$  for an acid molecule is:

$$(5.1) \quad \alpha = \frac{1}{1 + 10^{pK_a - pH}}$$

However, the above description does not include effects resulting from the electrostatic interaction between charges. Each amphiphile near the interface is surrounded by many other amphiphiles. If one amphiphile dissociates, then due to the strong electrostatic repulsion between the neighboring charges, it will become harder for its immediate neighbors to dissociate. If one lanthanide ion is absorbed, due to the electrostatic attraction between positive charged ions and negative charged amphiphiles, it will be easier for nearby amphiphiles to dissociate. Therefore, the actual dissociation and adsorption

rate depends on many factors such as the range of electrostatic correlations, dielectric environment due to local water structure and the specific arrangement of amphiphiles and ions, see Figure 5.4(a).

We model the effects of electrostatic interactions by a lattice model introduced by Netz [102], and used in previous studies [103, 104]. We choose hexagonal lattices for both ODPa molecules and lanthanide ions. One layer represents the ODPa molecule headgroups, while the other represents the lanthanide ions (Fig. 5.4(b)). For the molecular layer, each site can have  $-1e$  (dissociated) or  $0$  (neutral) charge; for the ionic layer, each site can have  $+3e$  (adsorbed) or  $0$  (not adsorbed) charge. Notice that charge neutrality does not have to hold locally between ODPa headgroups and ions, as discussed earlier. Two nearby sites are separated by  $\sigma = 0.5nm$ , comparable to the size of hydrated ions. The distance between two layers are approximately the size of the hydrated lanthanide ions, which we set  $\sigma = 0.5nm$ .

Our modified Monte-Carlo model introduces several parameters to capture the dielectric inhomogeneity. First, we define the Bjerrum length  $l_B = \frac{e^2}{4\pi\epsilon_0\epsilon_1 k_B T}$  to indicate the electrostatic strength, where  $\epsilon$  is the relative permittivity,  $e$  is the unit charge and  $k_B T$  is the thermo energy. ( $l_B = 0.7nm$  for an aqueous environment). Thus, the screened electrostatic interaction between two charges is  $\frac{E}{k_B T} = l_B \frac{Z_i Z_j}{r_{ij}} e^{-\kappa r_{ij}}$ , where  $Z$  is the valence,  $r$  is the distance, and  $\kappa$  is the inverse of Debye screening length. To effectively capture the dielectric inhomogeneity, we then introduce three parameters:  $l_B^+$ ,  $l_B^-$  and  $l_B^{inter}$  to represent the strength of electrostatic positively charged ion/ion interactions, negatively charged molecule/molecule interaction and interlayer molecule/ion interactions respectively. The

Hamiltonian used in our simulations is then given by

$$(5.2) \quad \frac{H}{k_B T} = -n_+ \ln(c) + \frac{\mu}{k_B T} n_- - l_B^{inter} \sum_{+-} \frac{Z_+ Z_-}{r_{+-}} e^{-\kappa r_{+-}} + l_B^- \sum_{--} \frac{Z_- Z_-}{r_{--}} e^{-\kappa r_{--}} + l_B^+ \sum_{++} \frac{Z_+ Z_+}{r_{++}} e^{-\kappa r_{++}}$$

where  $n_+$  is the number of adsorbed ions (how many sites are +3 charged),  $c$  is the bulk concentration of lanthanide ions.  $\sum_{+-}$  means the summation over all charged ion/molecule pairs. The chemical potential of the dissociation of acid molecules is given by 4

$$(5.3) \quad \frac{\mu}{k_B T} = -\ln 10(pH - pKa)$$

This value is a constant since the pH is constant.

Before getting into details of the simulation results, we discuss an analytical model to rationalize the physical mechanism leading to a sharp transition. In the Hamiltonian above, the summation terms depend on the lattice configuration of the system. To simplify this Hamiltonian, we define  $f$  as the fraction of dissociated sites ( $0 \leq f \leq 1$ ),  $f_+$  for positive charged lanthanides ions and  $f_-$  for negative charged molecules. Qualitatively,

$$(5.4) \quad \sum_{ij} \frac{e^{-\kappa r_{ij}}}{r_{ij}} \approx f_i f_j, \quad (i, j = +, -)$$

Note that this scaling argument is a very crude approximation since it ignores the lattice configuration, the screening factor and even the  $1/r$  electrostatic potential. The

Hamiltonian simplifies to:

$$(5.5) \quad \frac{H}{k_B T} \approx -f_+ \ln(c) - 3l_B^{inter} f_+ f_- + l_B^- f_- f_- + 9l_B^+ f_+ f_+$$

where the coefficients 3 and 9 are from the charge valence of the lanthanides ion. For any given concentration  $c$ , the equilibrium  $f_+$ ,  $f_-$  value is obtained by minimizing  $H$ . Since  $H$  is expressed as a 2nd-order function with two variables, the Hessian matrix is

$$(5.6) \quad \begin{bmatrix} \frac{\partial^2 H}{\partial f_+ \partial f_+} & \frac{\partial^2 H}{\partial f_+ \partial f_-} \\ \frac{\partial^2 H}{\partial f_- \partial f_+} & \frac{\partial^2 H}{\partial f_- \partial f_-} \end{bmatrix} = \begin{bmatrix} 18l_B^+ & -3l_B^{inter} \\ -3l_B^{inter} & 2l_B^- \end{bmatrix}$$

If  $(l_B^{inter})^2 < 4l_B^- l_B^+$ , the Hessian matrix has two positive eigenvalues,  $H$  is positive definite, and thus always has a local minimum at:

$$(5.7) \quad f_+ = \frac{\ln c}{9(2l_B^+ - \frac{(l_B^{inter})^2}{2l_B^-})}, \quad f_- = \frac{3l_B^{inter}}{2l_B^-} f_+$$

Therefore,  $f_+(f_-)$  changes continuously with concentration.

However, if  $(l_B^{inter})^2 > 4l_B^- l_B^+$ , the Hessian matrix has both positive and negative eigenvalues,  $H$  is saddle-like, and has no local minimum. Due to  $0 \leq f \leq 1$ , either  $f_+(f_-) = 0$  or  $1$  would give the minimum  $H$  of the system. Therefore,  $f_+(f_-)$  has a sharp transition from 0 to 1 at some threshold concentration  $c_0$ . The threshold concentration can be estimated by considering the Hamiltonian in two scenarios:

$$(5.8) \quad H(f_+ = f_- = 1) \leq H(f_+ = f_- = 0)$$

which gives

$$(5.9) \quad \ln(c_0) \approx -3l_B^{inter} + l_B^- + 9l_B^+$$

It is easy to notice that the threshold concentration will be larger for a smaller interlayer coupling strength.

To summarize, the relation between  $(l_B^{inter})^2$  and  $l_B^-l_B^+$  provides a guideline to predict the sharp transition regime. Since the Hamiltonian is highly simplified, we cannot rely on the exact condition  $(l_B^{inter})^2 > 4l_B^-l_B^+$  to predict the sharp transition regime. In particular, we cannot assume the coefficient is 4 in a real situation. We can assume generally  $(l_B^{inter})^2 > kl_B^-l_B^+$  but the coefficient  $k$  must be determined from the simulation results.

The concentration dependent dissociation and adsorption rate are calculated for various combinations of  $l_B$  to compare with the experimental results (see Methods/Simulation Parameters section).

Alternatively, if we fix all three Bjerrum lengths, then only increasing the interlayer distance would increase the threshold concentration. The reason is that the strength of interlayer interaction decreases with increasing the interlayer distance, thus higher threshold bulk concentration of ions is needed for the transition, as discussed above. Simulation shows that about 7% change of the distance would result in an order of magnitude difference in the threshold concentration. A distance of  $d = 1.07\sigma$  would fit the neodymium experimental data very well [see Figure 5.2]. The atomic radius of erbium, the heavier lanthanide, is about 9% smaller than that of neodymium; this is the "lanthanide contraction". The 7% distance difference between Er and Nd simulation systems is roughly consistent with the hydrated ionic size difference between Er and Nd. This implies that the vastly

different threshold concentrations for Er and Nd are due to the different strength of electrostatic interaction resulting from their slightly different hydrated ion sizes. As reported above, a mixture of Nd and Er does not show any sharp transition with increasing bulk concentration. From the theoretical point of view, the three-component system (Nd, Er and ODPa) has a 3 by 3 Hessian Matrix. The analytical condition for a sharp transition is too complicated to obtain any simple physical insight. Most practical parameters in this system would lead to a positive definite Hamiltonian, which has no sharp transition, consistent with the experimental observation (Fig. 5.3). This is also confirmed by the simulation.

### 5.3. Conclusions

This study shows that strong elemental selectivity in the solvent extraction process occurs at the interface between aqueous and organic phases. Erbium (the heavier and smaller lanthanide) is attracted to a Langmuir monolayer of extractant-like molecules even at much lower bulk concentrations than neodymium. When both metals are present in the solution, erbium is the dominant surface adsorbant even when much more neodymium is present in the bulk. Using a theoretical model and Monte Carlo simulations, we find that electrostatic effects arising from the inhomogeneity of the interfacial medium and small differences between ions are responsible for this strong selectivity between these two chemically similar ions. Our results imply that the interface plays the essential role in separating lanthanides during solvent extraction. We therefore suggest that efforts to understand, modify and improve lanthanide (and perhaps also actinide) separations processes should focus on the unusual chemical environment of the interface.

#### 5.4. Appendix: Simulation Parameters

The concentration dependent dissociation and adsorption rate was calculated for various combinations of  $l_B$  to compare with the experimental results. Since  $\epsilon_{air} \sim 1$  and  $\epsilon_{water} \sim 80$ , we simply assume the molecules near the interface have a dielectric constant  $\epsilon_{average} = (\epsilon_{air} + \epsilon_{water})/2$  which leads to  $l_B^- = 2l_B^{water}$ . According to the experiments, the surface density of ions after the threshold concentration stays constant ( $0.016Er/\text{\AA}^2$  or  $0.013Nd/\text{\AA}^2$ ) at higher bulk concentrations. This means that there are  $\sim 3 - 4$  ODPAs molecules per ion. Simulation shows that the surface density only depends on the ratio  $l_B^{inter}/l_B^+$ . Larger  $l_B^{inter}/l_B^+$  gives larger surface density and vice versa. In particular,  $l_B^{inter}/l_B^+ = 1.11$  gives a good fit to the observed saturation surface density. Together with the threshold concentration of the sharp transition, we can fit the erbium experimental data with simulation parameters  $l_B^+ = 1.769l_B^{water}$ ,  $l_B^{inter} = 1.963l_B^{water}$ , with adsorption layer distance  $\sigma = 0.5nm$  [see Figure 1]. Notice here  $(l_B^{water})^2 = 1.089l_B^-l_B^+$  does not exactly match the analytical coefficient of 4 in the sharp transition criterion  $(l_B^{inter})^2 > kl_B^-l_B^+$ . To justify why  $l_B^+$  is larger than  $l_B^{water}$  here, as we mentioned, full atom simulation shows concentrated solution results in a different bulk dielectric constant (e.g. 1M concentration would decrease  $\epsilon_{water}$  from 80 to about 40) [101]. Since the surface density of ions is equivalent to a local concentration  $\sim 1M$ ,  $l_B^+ \sim 2l_B^{water}$  is a good qualitative approximation. A typical simulation system consists of two layers of sites ( $N=80*80*2=12800$ ), with 1,000 equilibration steps and 10,000 measurement sweeps, where a sweep is defined as the attempt to flip the charge of all sites.

Please find the details of experimental part in the original publication.

## CHAPTER 6

## Electrostatic Control of Polymorphism in Charged Amphiphile Assemblies

To present a complete story, I have included figures by Changrui Gao. The content of this chapter is based on the following publications:

- Changrui Gao, Honghao Li, Yue Li, Sumit Kewalramani, Liam C. Palmer, Vinayak P. Dravid, Samuel I. Stupp, Monica Olvera de la Cruz, and Michael J. Bedzyk. "Electrostatic control of polymorphism in charged amphiphile assemblies." *The Journal of Physical Chemistry B* 121, no. 7 (2017): 1623-1628.
- Changrui Gao, Honghao Li, Sumit Kewalramani, Monica Olvera de la Cruz, and Michael J. Bedzyk. "Electrostatic shape control of a charged molecular membrane from ribbon to scroll" (to be submitted).

### 6.1. Introduction

Molecular self-assembly is defined as the process of spontaneous association of randomly distributed molecular units into highly organized supramolecular structures. A typical building block of those functional self-assembly structure is the amphiphilic molecule, which is a type of molecule possessing both hydrophilic and hydrophobic properties. The structure of common amphiphilic molecules consists of a polar hydrophilic head-group grafted to a hydrophobic carbon chain. When dissolved in aqueous solution, these

molecules can self-assemble into a large variety of aggregates such as micelles, fibers, planar membranes, and vesicles.

Assemblies of amphiphilic molecules in aqueous solutions and at interfaces are often used as model systems for cell membranes and associated processes and have important nanotechnological applications, including extraction[**20, 22**], decontamination and remediation [**105**], and biosensing [**106**]. Peptide amphiphiles (PAs), molecules in which a hydrophobic alkyl tail is covalently linked to an amino acid sequence, can self-assemble into nanostructures with a broad range of applications[**107, 108, 109, 110, 111**]. Interestingly, these structures can reconfigure in response to external stimuli, including temperature, pH, and ionic strength[**112, 113, 114**], which allows versatile conformations such as membrane and fiber conformations that can mimic extracellular matrixes[**115**].

The varying structures of PA assembly could arise from interplay of several different intermolecular interactions, including van der Waals, hydrogen bonding, electrostatic interaction, steric effect, and  $\pi$ - $\pi$  stacking. However, it remains highly challenging to experimentally regulate those intermolecular interactions, and also detailed physical explanations of the equilibrium self-assembly structure are often lacking in those studies. Electrostatic interaction, unlike other interactions, can be experimentally tuned by the solution pH and salt concentration. The solution pH controls the charge of the amino acids in the headgroup, and the counterions from the salt screen the intermolecular electrostatic interactions. Theoretical investigations have probed the dependence of PA assembly structures on the relative strengths of the electrostatic interactions[**116, 117**]. For example, a combined Monte Carlo, molecular dynamics (MD) simulation, and transmission electron microscopy (TEM) study on the assembly of a bioactive PA showed that PAs assemble

into spherical or cylindrical micelle structure only if the electrostatic repulsion between the headgroup is weak. This demonstrates the critical role of electrostatic interactions in the PA assembly.

So the first part of this chapter focuses on how Monte-Carlo simulations give better estimation of the electrostatic interaction in such systems.

Another interesting assembly structure is the nanoribbon, which is a high aspect ratio (10:1 or greater) bilayer. Nanoribbons are a gateway to a number of other morphologies with distinct functionalities. For example, nanoribbons of a charged chromophore amphiphile can transform to a scroll-like (cochleate) morphology when the ionic strength of the solution is increased [118]. These cochleate structures serve as efficient charge transfer agents for photocatalysts in hydrogen production. Cochleate formation from liposomes of negatively charged phospholipids in the presence of multivalent cations also involves a nanoribbon intermediate [119, 120, 121]. Biocompatible phospholipid cochleates are being explored as drug-delivery agents because they can trap macromolecules, such as proteins, peptides and DNA, and provide protection against degradation due to their multilayer geometry. Nanoribbons have also been observed in peptide amphiphiles (PA), which consist of a sequence of amino acids covalently linked to an alkyl tail [109, 109]. For example, a peptide amphiphile that stimulates collagen production has been found to self-assemble into nanotapes with an internal bilayer structure [122]. In a PA with alternating charged and neutral amino acids, nanoribbons were found to transform into helical ribbons as the PA concentration was reduced [123] and into helical and twisted nanoribbons when the amino acid sequence was permuted [124]. Helical supramolecular assemblies have been previously used to template semiconductor nanohelices [125].

Despite the progress, the correlation between experimental conditions such as molecular design, ionic strength, pH, amphiphile concentration and the attained nanoribbon-related morphology are not fully established. Therefore, precise control of nanoribbon assembly architecture requires further understanding of the delicate interplay between intermolecular interactions and elastic and interfacial energies.

A recent theoretical study showed that for charged molecules, tuning the range of electrostatic interactions could induce transitions between different nanoribbon-related morphologies [126]. Specifically, a phase diagram was deduced for a 2D lattice of charged points, which interacted via long-range repulsive electrostatic interactions and short-range attractive interactions. Planar nanoribbon to wavy ribbon with periodic undulations to helical ribbon transitions were predicted as the range of the electrostatic interactions is increased. This study suggests a facile experimental method for accessing distinct nanoribbon architectures by varying the ionic strength ( $\mu$ ) of the solution because the range of electrostatic interactions as parameterized by Debye length ( $\lambda_D$ ) scales as  $\mu^{-1/2}$ . Recent experiments also attest that tuning the ionic strength leads to predictable changes in the nanoribbon-related assembly morphology. For example, the period of the twists in amyloid fibril aggregates monotonically increases with decreasing ionic strength [127].

In the second part of this chapter, we focus on the morphological changes in charged planar nanoribbons as a function of increasing ionic strength. In this regime, the inter-nanoribbon interactions become prominent, and as mentioned, nanoribbon to cochleate transformations have been observed in phospholipids [120] and chromophore amphiphiles

[118, 128, 129, 130]. However, the generality and the mechanistic details of this transition are still unknown. In particular, the correlation between the ionic strength induced changes in the molecular packing and the mesoscopic morphology transformations are elusive.

## 6.2. Polymorphism of peptide amphiphile assembly induced by headgroup charge and size regulation

Our collaborator Changrui Gao focuses on the self-assembly of a modular series of peptide amphiphiles:  $C_{16}K_4$ ,  $C_{16}K_3$ ,  $C_{16}K_2$ , and  $C_{16}K_1$ , which carry different number of ionizable lysine residues conjugated to the same  $C_{16}$ -alkyl tail (Fig. 6.1)

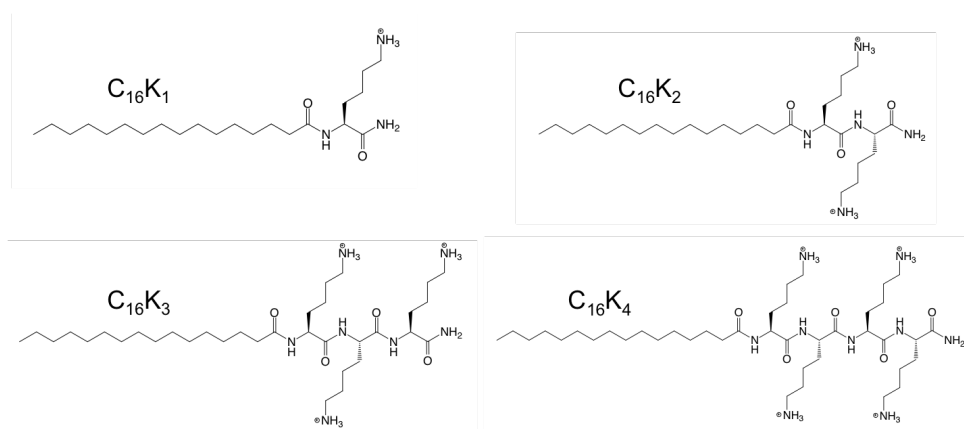


Figure 6.1. Molecular structures of positively charged  $C_{16}K_4$ ,  $C_{16}K_3$ ,  $C_{16}K_2$ , and  $C_{16}K_1$  peptide amphiphiles.

Based on their SAXS/WAXS and Cryo-TEM results, They establish a phase diagram shown in Figure 6.2 as function of pH and headgroup. In this diagram, we can observe that as the headgroup size decreases and pH increases (i.e. headgroup charge decreases), the equilibrium self-assembly structure transforms from ill-defined unaggregated state to spherical micelles, to cylindrical micelles, to nanoribbons, and finally to microtubules,

which depicts the correlation between intermolecular interaction and resulting assembly structures. Strong intermolecular repulsion (electrostatic and steric) could lead to loosely packed assembly structures (spherical micelles) or even no assembly at all, while the weak repulsion favors the formation of closely packed assemblies such as crystalline bilayers. Future work could focus on the theoretical simulation of the assembly structures (i.e. Molecular Dynamic simulation) to quantitatively describe the correlations between the thermodynamic equilibrium structures and the strength of intermolecular interactions.

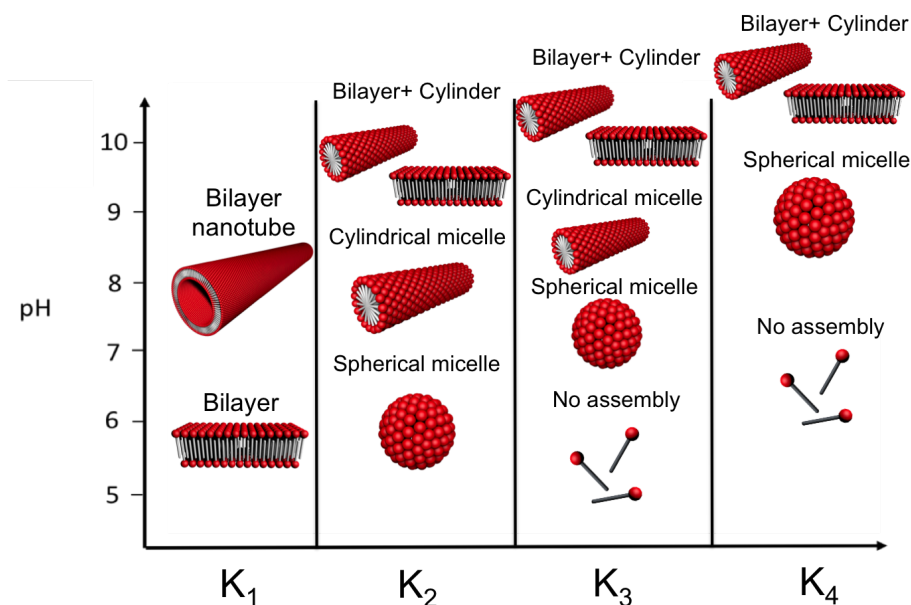


Figure 6.2. Phase diagram showing the formation and transition of self-assembly morphology of  $C_{16}K_n$  peptide amphiphile as a function of head-group size and pH.

Here we take  $C_{16}K_2$  as an example, see Fig. 6.3.

The effects of charge correlations on the ionization of  $C_{16}K_2$  headgroup as a function of pH were examined by Monte Carlo simulations. According to the Henderson Hasselbach

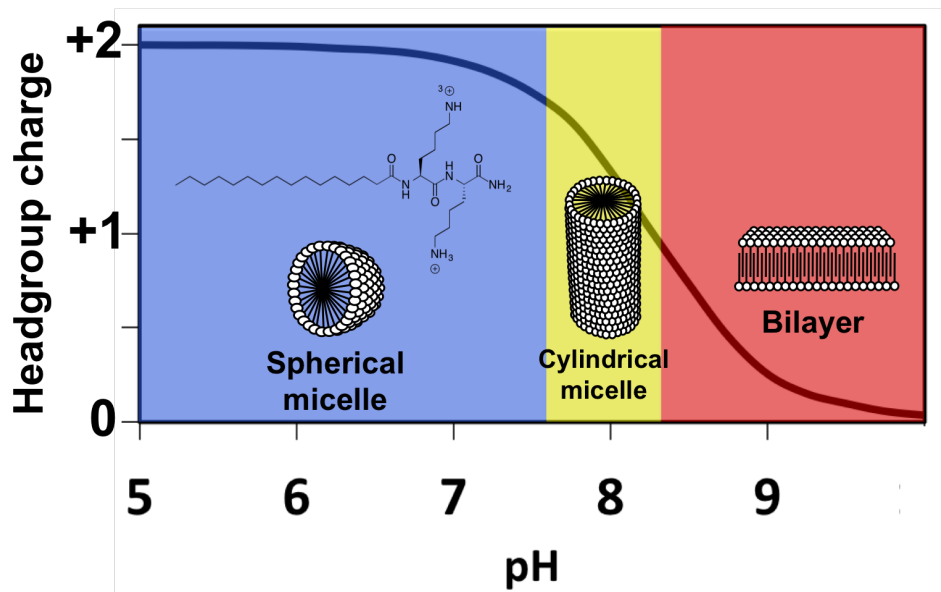


Figure 6.3. Phase diagram showing the formation and transition of self-assembly morphology (the headgroup charge) of  $C_{16}K_2$  peptide amphiphile as a function pH.

equation, the fraction of dissociated sites  $\alpha$  for a monoprotic acid is:

$$(6.1) \quad \alpha = \frac{1}{1 + 10^{pK_a - pH}}$$

However, the above description does not include the effects resulting from the electrostatic interaction between charges. Each amphiphile in the self-assembly structures is surrounded by many other amphiphiles. If an amphiphile dissociates due to the strong electrostatic repulsion between the neighboring charges, it will become harder for its immediate neighbors to dissociate as well (this is true also for other ionizable groups on the same molecule). In other words, the average dissociation will become much lower. Therefore, the actual dissociation depends on the range of electrostatic correlations and the specific arrangement of amphiphiles in the self-assembly structures.

We model the effects of electrostatic interactions by a lattice model introduced by Netz [102], and used in previous studies [103]. As a simplification, we choose a square lattice for  $C_{16}K_2$  molecules. Two nearby sites separated by  $0.5nm$  are connected to represent a single molecule. Each site can be either in state  $n = 0$  (neutral) or  $n = 1$  (dissociated). The energy is measured in terms of  $k_B T$ , and the Bjerrum length  $l_B = \frac{e^2}{4\pi\epsilon_0\epsilon_1 k_B T}$  is introduced for simplicity, where  $\epsilon_r$  is the relative permittivity and the  $e$  is the unit charge. The Hamiltonian used in the simulations is given by

$$(6.2) \quad \frac{H}{k_B T} = \frac{\mu}{k_B T} \sum_i n_i + \frac{1}{2} \sum_{i \neq j} l_B \frac{e^{-\kappa r_{ij}}}{r_{ij}}$$

where  $n = 0$  or  $1$  is the dissociation state of site  $i$  and  $\kappa$  is the inverse of the Debye screening length which is controlled by the salt concentration. In order to model actual experiment, we set the Bjerrum length  $l_B = 0.7nm$  for aqueous environment and  $l_B = 1.4nm$  for water-air interface. The chemical potential (as mentioned in previous chapter):

$$(6.3) \quad \frac{\mu}{k_B T} = -\ln 10(pH - pKa)$$

A typical simulation consists of 10,000 equilibration steps and 100,000 measurement sweeps, where a sweep is defined as an attempted flip of each site.

Figure 6.4c shows the measured titration curve for 4 mM  $C_{16}K_2$  with 100 mM NaOH.  $C_{16}K_2$  was soluble over the entire pH range with the solutions becoming highly viscous for  $pH > 10$ . For comparison, two calculated titration curves are shown (Figure 6.4c). The first calculation (red, dashed) assumes that each protonated lysine is a monoprotic acid with a  $pKa = 8.2$  and uses the HendersonHasselbach equation (6.1) up to the volume

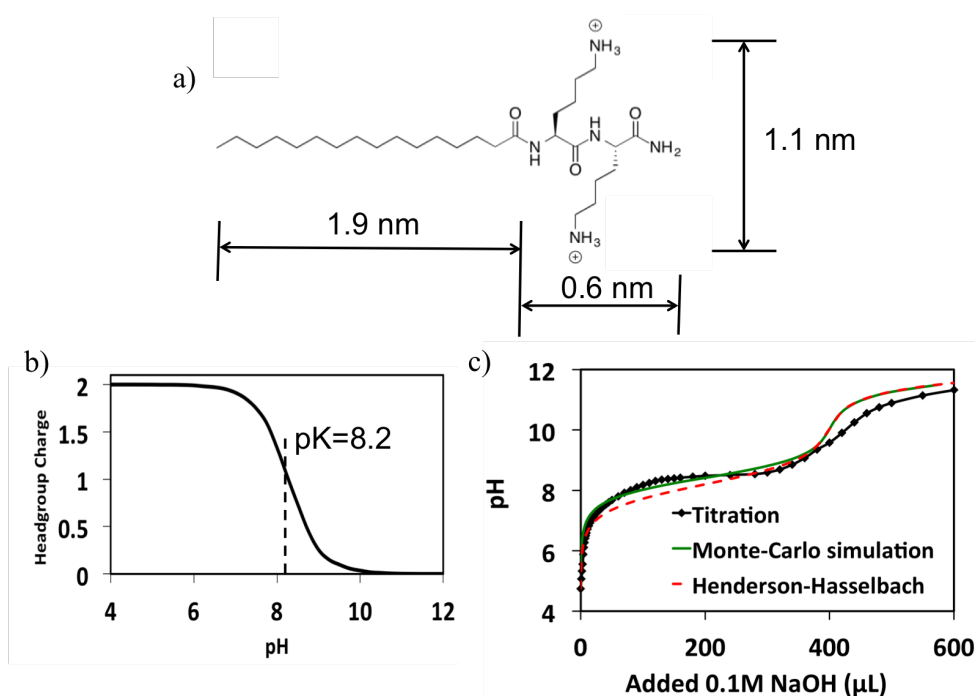


Figure 6.4. (a) Molecular structure of +2 charged  $C_{16}K_2$  peptide with estimates for the hydrophobic tail length and hydrophilic headgroup length and width. (b) Averaged  $C_{16}K_2$  headgroup charge as a function of pH in standard water environment obtained by Monte Carlo simulation, showing deprotonation around pH 8.2. (c)  $C_{16}K_2$  titration curve showing how pH changes as a function of the volume of NaOH added. For comparison, calculated titration curves based on a monoprotic acid with  $pK_a = 8.2$  (red, dashed) and Monte Carlo simulations (green) are shown.

added of NaOH, corresponding to an equivalent concentration of PA and NaOH (equivalence point; here,  $400 \mu L$  of NaOH). Thereafter, the added NaOH is assumed to only increase the solution pH. The second calculation, which reproduces the measured titration curve better up to  $pH \sim 9.5$  is based on the above-described Monte Carlo simulation that takes into account electrostatic correlations in the ionization process. Both of the calculations deviate from the measured titration curve in a regime where the solution became highly viscous. Nevertheless, these observations show that Monte Carlo simulations

can be used to estimate a priori the ionization tendency of molecules that are in close proximity. It should be noted that the observed titration curves vary slightly between synthetic batches of  $C_{16}K_2$  (see the original paper [104]). These differences could be due to variations in the concentration of the amphiphile or of residual salts after purification and lyophilization. Regardless, only one buffer region (plateau at  $\text{pH} \sim 8$ ) is observed in the titration curves for  $C_{16}K_2$ . According to Monte-Carlo simulation, it is because (1) the electrostatic interaction between charges in the same molecules is not strong enough; (2) the distance between two molecules is not far enough. Because morphological transformations such as the micelle to vesicle transition in fatty acids [131, 132] frequently occur at  $\text{pH} \sim \text{pK}$ , we hypothesized that a nano- or mesoscopic structural transformation would also occur at  $\text{pH} \sim 8$  in our system.

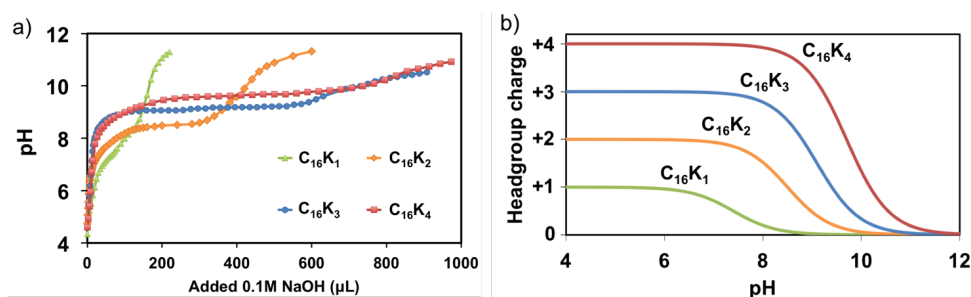


Figure 6.5. (a)  $C_{16}K_n$  titration curves showing how pH changes as function of the volume of NaOH added. All  $C_{16}K_n$  exhibit single buffer stage. (b) Averaged  $C_{16}K_n$  headgroup charge as a function of pH obtained through Henderson-Hasselbach equation of monoprotic acid (6.1).  $\text{pK}_a$  is determined from the titration curves.

Figure 6.5a shows the measured titration curves for 5 mL 4 mM  $C_{16}K_n$  with 100 mM NaOH solution. All the molecules are soluble over the studied pH range. We can observe that the titration curves for all  $C_{16}K_n$  molecules exhibit only one buffer stage, indicating that the fully ionized  $C_{16}K_n$  behave as monoprotic acid regardless of the number of lysines

(K) on the headgroup. Therefore, we are able to use Henderson-Hasselbach equation to derive the charge vs. pH curves for  $C_{16}K_n$ . The  $pK_a$  can be determined from the center positions on the buffer stages of the titration curves, the pKa for  $C_{16}K_1$ ,  $C_{16}K_2$ ,  $C_{16}K_3$  and  $C_{16}K_4$  are found to be 7.4, 8.3, 9.1, and 9.7 respectively. We notice that the  $pK_a$  for all four molecules are lower than the  $pK_a \sim 10.0$  expected for isolated lysine. This implies that in  $C_{16}K_n$  assemblies, the ionization tendency of lysines is reduced, because any arrangement of like-charged molecules in close proximity increases the overall electrostatic potential energy of the ionized state. This can also be proven by Monte-Carlo simulation of  $C_{16}K_2$  assembly showing a theoretical deionization curve with pKa  $\sim 8.2$ . Figure 6.5b shows the averaged headgroup charge vs. solution pH curves for  $C_{16}K_1$ ,  $C_{16}K_2$ ,  $C_{16}K_3$  and  $C_{16}K_4$  peptide amphiphiles from Henderson-Hasselbach equation (6.1). At low pH, the lysine groups are fully ionized and further increase in pH leads to a monotonic decrease in the headgroup charge for all four peptide amphiphiles. The significant decrease in headgroup charge occurs around the pKa of each  $C_{16}K_n$  molecule, therefore we hypothesized that nano- or mesoscopic structural transformations would also occur at  $\text{pH} \sim \text{pKa}$ . Following studies will focus on the structural transformation around  $\text{pH} \sim \text{pKa}$ , and explore the correlations between the electrostatic repulsion and self-assembly morphologies for different  $C_{16}K_n$  molecules.

### 6.3. Electrostatic control of nanoribbon-to-cochleate transition in a charged peptide amphiphile assembly

For the present work, the simplest possible charged peptide amphiphile (PA):  $C_{16}K_1$  was chosen, where a single ionizable amino acid lysine ( $K$ ) is covalently linked to a palmitoyl ( $C_{16}$ ) alkyl tail. This PA was chosen because our recent studies [104] on  $C_{16}K_2$  found spherical micelle to cylindrical micelle to a mixture of cylindrical micelle and nanoribbon transformations as the molecular charge was reduced by increasing the solution pH. Therefore, we hypothesized that removing one of the charged lysines from the headgroup could yield a macroscopic state consisting purely of nanoribbons. Second, the choice of this PA ensures that the inter-headgroup interactions are Coulombic. This is unlike the case of other PAs with multiple amino acids, where the assembly is strongly modulated by intermolecular hydrogen bonding.

To understand the effects of screening of intermolecular electrostatic interactions on the assembly morphology, we analyzed dispersions of  $C_{16}K_1$  in solutions containing NaCl at concentrations  $c$  ranging from 0 to 100 mM. Figure 6.6a-d show atomic force microscopy (AFM) images of  $C_{16}K_1$  assemblies at Si/NaCl solution interfaces for  $c = 0, 1, 3$  and 5 mM. Peakforce error images are shown because they deliver better 3D representation of the assembly morphologies. As the NaCl concentration is increased the aspect ratio of the ribbons decreases, and at  $c = 3$  mM, nearly isotropic sheets of  $1\text{-}3\mu\text{m}$  diameter are observed (Figure 6.6c). At or above this threshold concentration ( $c_{th}$ ), the sheets roll into scrolls or cochleates (Figure 6.6d). The multi-layered nature of the scrolls is better observed in cryo-transmission electron microscopy (cryo-TEM) images (Figure 6.6e-h). These cryo-TEM images (Figure 6.6f-h) further reveal that the interlayer spacing ( $D$ )

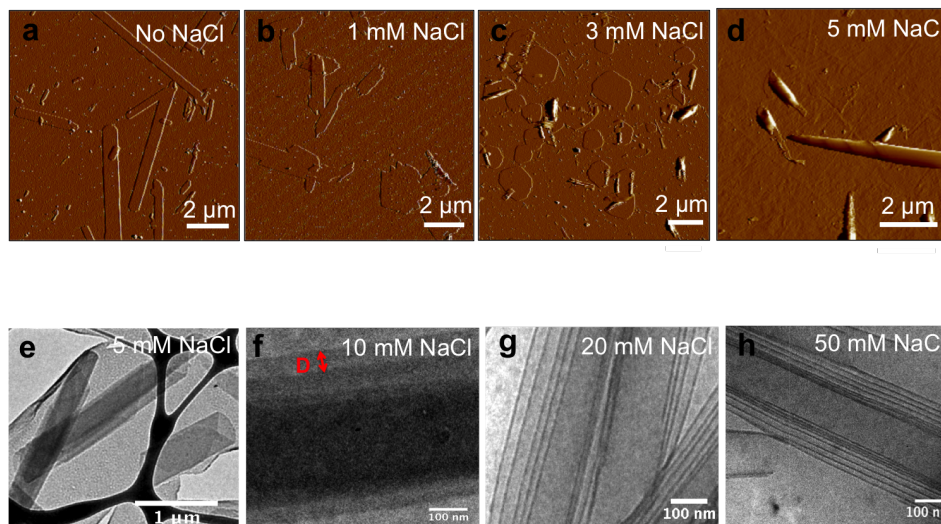


Figure 6.6. (a-d) AFM peakforce error images for  $C_{16}K_1$  membranes at Si/NaCl solution interfaces. As the NaCl concentration increases, nanoribbon to isotropic sheet and to rolled-up cochleate transformations are observed. (e-h) Cryogenic TEM images of cochleates exhibit scroll morphology and the internal multilayer features. It can be readily seen that the interbilayer spacing  $D$  within the cochleate structure decreases with increasing NaCl concentration.

within the cochleate structure monotonically decreases with increasing  $c$ . Overall, AFM and cryo-TEM show that for  $C_{16}K_1$ , increasing the solution ionic strength first induces the ribbon to cochleate transition, and thereafter, reduces the inter-lamellar spacing within the cochleates, see Figure 6.7.

To qualitatively understand the origins of the observed structural changes in the ribbon to cochleate transition from the perspective of interplay between various intermolecular interactions, and membrane bending and interfacial energies, we develop simple theoretical models. Three aspects are focused upon: (1) The decrease in the ribbon aspect ratio with increasing salt concentration, (2) The origin of curvature in the membranes, and (3)

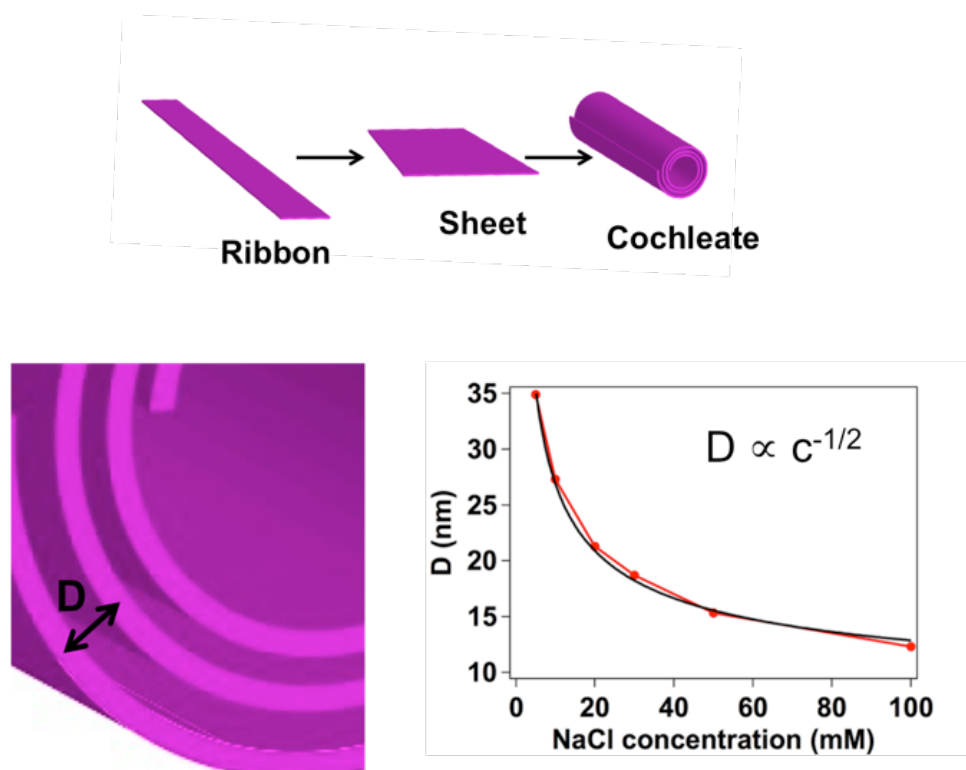


Figure 6.7. (upper) Illustration of nanoribbon-to-cochleate transition. (bottom) Interlayer distance decreases with increasing salt concentration.

the linear relationship between the interbilayer separation within the cochleates and the electrostatic screening length.

We first discuss the ribbon to sheet transformation. For this we model the membrane as a parallelepiped (Fig. 6.8a) with top and bottom faces uniformly charged, and formulate the membrane energy per unit volume as a sum of long-ranged electrostatic interaction energy and an interfacial energy term that accounts for the direct exposure of hydrophobic tails to water on the membranes side surfaces (Eq. 6.4, see 6.4 for details). Short ranged interactions such as intermolecular van der Waals interactions are neglected because the contribution of these interactions to the areal or volume normalized energies is expected to be a constant. Furthermore, we assume that the area of the membrane is independent

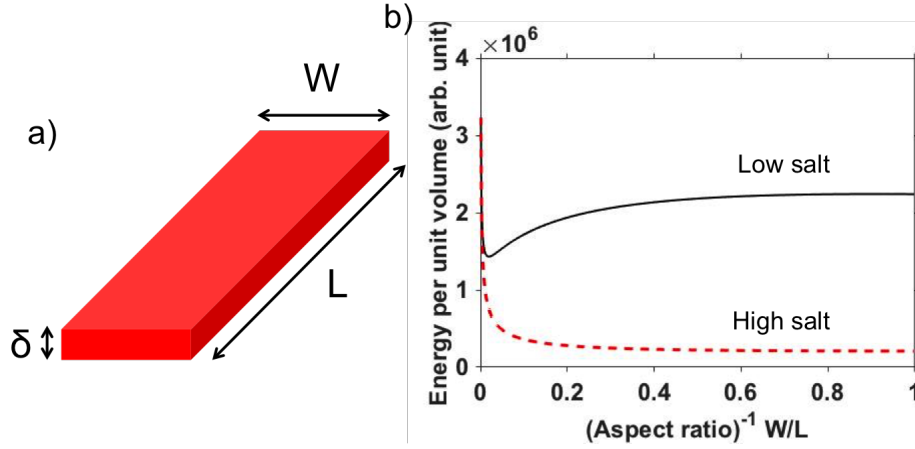


Figure 6.8. (a) Schematic representation of  $C_{16}K_1$  nanoribbon showing ribbon dimensions used for the energy calculation. (b) The membrane energy per unit area in equation (1) as a function of the inverse of membrane aspect ratio  $W/L$ . At low salt concentration, the minimum of the membrane energy indicates that elongated ribbon structure is the equilibrium morphology. As salt concentration increases, the membrane energy starts to decrease monotonically with  $W/L$  and drives the membrane to form low aspect ratio morphology.

of the salt concentration. This assumption is justified based on AFM images in Fig. 6.6, where membranes with areas in the range about  $1 \sim 5 \mu m^2$  are observed, regardless of the salt concentration. The membrane energy per unit volume is (see Appendix for derivation):

$$(6.4) \quad \frac{U_{electrostatic} + U_{interface}}{V} = 2\left(\frac{N_T^2}{VA}\right)k_B T l_B \int \int_{W,L} \frac{e^{-\sqrt{x^2+y^2}/\lambda_d}}{\sqrt{x^2+y^2}} dx dy + \frac{2\gamma(\sqrt{A/\chi} + \sqrt{A\chi})}{A}$$

where  $A$  and  $V$  are the area and volume of the membrane,  $N_T$  is the total membrane charge,  $\gamma$  is the interfacial tension for the membrane side surfaces,  $l_B$  is the Bjerrum length.  $\lambda_d$  is the electrostatic screening length, which is proportional to  $\sqrt{(1/c)}$ , where  $c$  is the salt concentration, and  $\chi = W/L$  is the inverse of membrane aspect ratio (Fig. 6.8a).

Eq. 6.4 shows that the interfacial energy term monotonically increases with increasing aspect ratio, whereas for a given  $c$ , the reverse is true for the electrostatic energy. This competition leads to an equilibrium aspect ratio, which minimizes the membrane energy per unit volume. At low salt concentrations, the equilibrium morphology is an elongated ribbon, as shown in Fig. 6.8b. Numerical values of the fixed parameters:  $A$ ,  $V$ ,  $l_B$ ,  $g$  and  $N_T$  that are used in the simulations in Fig. 6.8b are presented in Table 6.1 (Appendix). As the salt concentration increases, the equilibrium membrane aspect ratio decreases. In the limiting case of very high salt concentration (very small  $\lambda_d$ ), the electrostatic term becomes independent of the aspect ratio, and the interfacial energy term drives the membrane to the lowest possible aspect ratio:  $\chi = 1$  (Fig. 6.8b).

We further study the ribbon-to-sheet transition by numerically computing the integral in (6.14). The model contains total  $\sim 10000$  charge points (e.g.  $100 \times 100$  when the aspect ratio is 1). The separation between nearby charges is  $0.5nm$ , consistent with the distance between amphiphile molecules. We maintain the total area to be constant while changing the aspect ratio  $W/L$ , calculate total energy (electrostatic and interfacial) per molecule, see Figure 6.9(a). At small Debye length (high salt concentration), membrane favors to be sheets (aspect ratio  $W/L = 1$ ); at large Debye length (low salt concentration), membrane favors to be narrow ribbons (small aspect ratio). If we plot the equilibrium aspect ratio over different Debye lengths. It is clearly a first-order phase transition, from narrow ribbons to sheets. However, we do see intermediate aspect ratio structures or different aspect ratio structures at the same time in experiment, e.g. see Figure 6.6(b). Actually, this is expected because near the phase transition point, the energy difference between two phases is very small (see inset of Figure 6.9(b)), much smaller than  $1k_B T$ .

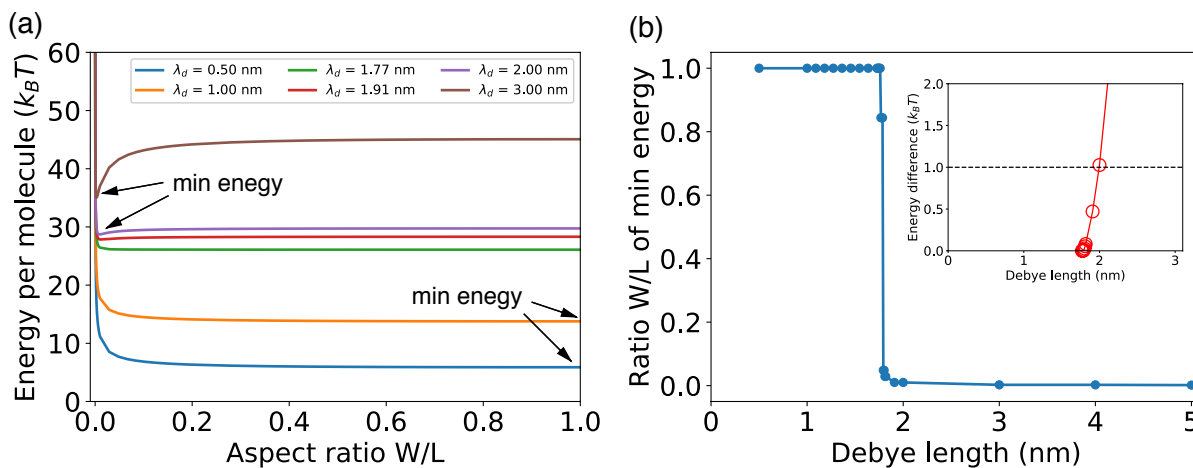


Figure 6.9. (a) Total energy per charged molecule vs. aspect ratio with total area of membrane being constant. At small Debye length (high salt concentration), membrane favors to be sheets (aspect ratio = 1); at large Debye length (low salt concentration), membrane favors to be narrow ribbons (small aspect ratio). (b) The equilibrium aspect ratio (minimum energy state) for different Debye length. It is a first order transition. (Inset) The energy difference between the equilibrium aspect ratio and the sheets (aspect ratio = 1). There energy difference near the transition point is much smaller than  $1k_B T$ .

Next, we consider the rolling of a flat membrane. This process involves a change in intermolecular electrostatic repulsion energy and the membrane elastic energy. When a thin membrane of a fixed perimeter length is bent, the intermolecular distances become shorter (Fig. 6.10a). This increases the overall membrane electrostatic energy. Furthermore, unless the membrane has an intrinsic curvature, external work must also be done to bend the membrane. To test whether the  $C_{16}K_1$  membranes possess an intrinsic curvature, we studied the self-assembly of  $C_{16}K_1$  at elevated pH (= 10) by adding excessive NaOH. In this scenario, the majority of the  $C_{16}K_1$  headgroups are expected to be unionized. Our result shows that under these conditions, the equilibrium morphology of  $C_{16}K_1$  assembly is a nanotube, see the original paper for details. Although counterintuitive, the

above observation shows that the symmetric  $C_{16}K_1$  bilayer has an intrinsic spontaneous curvature, and rolling of a flat membrane could in fact decrease the curvature energy. To further illustrate the membrane rolling, we use a simple model consisting of an array of charged species with pre- defined array length  $L_0$  and an intrinsic spontaneous curvature  $C_0$ , and calculate the total energy (electrostatic + curvature energy) as a function of curvature and salt concentration (Eq. 6.5, see Appendix for details).

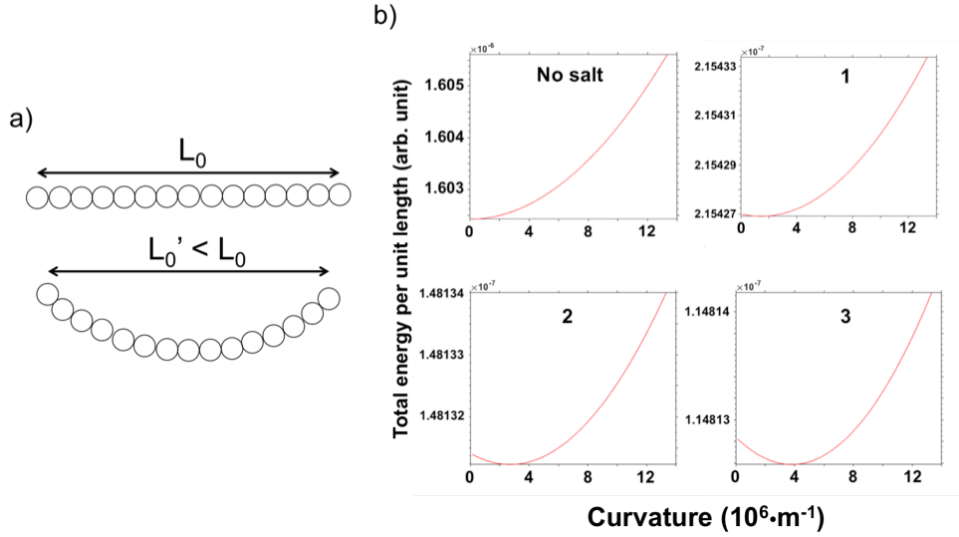


Figure 6.10. (a) An array of charged species with array length  $L_0$  and spontaneous curve  $C_0$ . This model is used to calculate the sum of electrostatic and curvature energy as a function of salt concentration and curvature. (b) Total energy per unit length (6.5) versus array curvature  $C_1$  at different salt concentrations ( $3 > 2 > 1 > \text{No salt}$ ).

$$(6.5) \quad \frac{U_{electrostatic} + U_{surface}}{L_0} = 2\rho^2 L_0 \int_{d_0}^{L_0} l_B \frac{e^{-\frac{2}{c_1} \sin(\frac{c_1 l}{2}) / \lambda_d}}{\frac{2}{c_1} \sin(\frac{c_1 l}{2})} dl + \frac{\kappa_c}{2} L_0 (C_1 - C_0)^2$$

where  $\rho$  is the membrane charge density,  $d_0$  is the nearest neighbor intermolecular distance,  $\kappa_c$  is the membrane bending stiffness,  $C_1$  is the curvature of the array and  $C_0$  is the intrinsic spontaneous curvature. For the limiting case of very high salt concentration

( $\lambda_d \rightarrow 0$ ). Eq. 6.5 shows that the electrostatic energy term is negligible, and the resulting morphology would possess the intrinsic membrane curvature ( $C_1 = C_0$ ). To elaborate, we present results from calculations of total array energy as a function of curvature for four salt concentrations in Fig. 6.10b. Numerical values for the fixed parameters ( $d_0$ ,  $C_0$ ,  $\kappa_c$ ,  $L_0$ ) are presented in Table 6.2 (Appendix). For the zero salt condition, the total energy increases with curvature (Fig. 6.10b, top left). Therefore, the flat membrane is the equilibrium shape. As the salt concentration is increased, the total energy shows a minimum for an optimal curvature value, which continues to increase towards the intrinsic membrane curvature with increasing salt concentration.

Finally, we investigate the relation between interbilayer separation within the rolled-up  $C_{16}K_1$  cochleate and salt concentration. We start with a theoretical model that is used to model the interactions in stacks of planar lipid bilayers. This model takes into account the interbilayer van der Waals attraction, short-range hydration repulsion and electrostatic repulsion between charged lipid bilayer membranes in solution. Specifically, the van der Waals attraction  $U_d(\delta, d)$ , the hydration  $U_h(d)$  and electrostatic repulsion energies per unit area are:

$$(6.6) \quad U_d(\delta, d) = -W \left[ \frac{1}{d^2} - \frac{2}{(d + \delta)^2} + \frac{1}{(d + 2\delta)^2} \right]$$

$$(6.7) \quad U_h(d) = H e^{-d/\Lambda_h}$$

$$(6.8) \quad U_e(d) = \frac{32\epsilon_0\epsilon_w(k_B T)^2}{q^2\lambda_d} \exp(-d/\lambda_d)$$

where  $\delta$  is the bilayer thickness and  $d$  is the thickness of the aqueous layer between the bilayers (Fig. 6.11a). Therefore,  $\delta + d = D$ , the interbilayer spacing.  $W$  is the Hamaker constant,  $H$  is the hydration repulsion pressure, and  $\Lambda_h$  is the decay length for the hydration pressure ( $\sim 0.2nm$ ).  $q$  is the electron charge,  $\epsilon_0$  is the vacuum permittivity,  $\epsilon_w$  is the dielectric constant of the aqueous solution, and  $k_B$  is the Boltzmann constant.

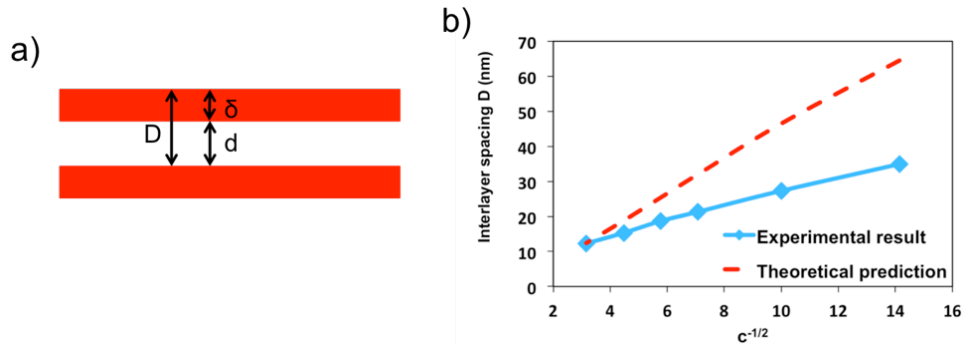


Figure 6.11. (a) The geometry of the lamellar stack. The thicknesses of membrane and interbilayer aqueous regions are  $\delta$  and  $d$ , respectively. (b) Theoretical prediction showing linear correlation between interbilayer spacing  $D$  and  $c^{-1/2}$ , where  $c$  is NaCl concentration with unit of mol/L. The deviation relative to experimental result is likely due to the assumption of planar stack rather than spiral geometry in the theoretical model.

Based on experiments, the aqueous layer thickness  $d$  varies between  $31 \sim 9nm$  when the salt concentration is varied between  $5 \sim 100mM$ . This thickness is much larger than decay length  $\Lambda_h$ . Therefore, the hydration energy term can be neglected in our theoretical model. The thickness  $d$  is also much larger than  $l_d$ , which varies from  $4.3nm$  to  $1nm$  when  $c$  is increased from 5 to 100 mM. Therefore, the use of the asymptotic form for the Debye-Huckel equation (Eq. 6.8) is valid.

In addition to the above energies in planar lipid bilayer stacks system, we also considered the curvature energy per unit area of cochleate spiral sheet, which turned out to

be independent of interbilayer spacing  $D$  (see Appendix). Therefore, equilibrium interbilayer spacing  $D$  is calculated at different salt concentrations  $c$  by minimizing the total free energy ( $U_d + U_e$ ) with respect to aqueous thickness  $d$ . The numerical values of all fixed parameters used in these calculations are summarized in Appendix, and Fig. 6.11b shows that the theoretical relationship between  $D$  and  $c$ . Similar to the experiments, the theoretical model also predicts that  $D$  varies linearly with  $c^{-1/2}$ , but with a slope that is  $2.5 \times$  larger than the experimentally determined slope for  $C_{16}K_1$  cochleates. This deviation is likely a result of the assumption of planar membrane stacks, and maybe corrected by deriving the correct form of van der Waals energy for a spiral sheet. Nevertheless, the above simplified theoretical model shows that the linear relationship between the interbilayer separation and the electrostatic screening length is not a result of system specific design, but a result of interplay between interbilayer van der Waals and electrostatic energies. Therefore, it is not a surprise that this linear relationship has been observed in other charged lamellar systems, such as clay mineral montmorillonite. It should however, be noted that the linear relationship does not appear to be generally valid in the presence of salts with multivalent ions. For example, traditional negatively charged phospholipid cochleates show little or no dependence of interbilayer spacing the concentration of  $CaCl_2$ . It is possible that the multivalent cations are covalently linked to the molecules. As such the resulting interbilayer electrostatic interactions cannot be parameterized by the screening length  $\lambda_d$ . By contrast, the use of monovalent salts to induce the  $C_{16}K_1$  cochleate structure leads to tunable interbilayer spacing over  $\sim 10 - 40$  nm. This structural feature may have potential application for controlled encapsulation and release of drug particles within specific size range.

## 6.4. Appendix: Theoretical models for ribbon-to-cochleate transition

### 6.4.1. Step 1: Ribbon-to-sheet transition

The bilayer ribbon is modeled as a parallelepiped of length  $L$ , which extends to  $\mu m$ , thickness  $\delta$ , which is roughly  $4nm$ , and width  $W$  (see Fig. 6.8a). The ribbon energy per volume can be written as a sum of electrostatic energy and interfacial energy, which accounts for the contact between the hydrophobic chains and water on the side faces of the ribbon.

$$(6.9) \quad U_{ribbon} = U_{electrostatic} + U_{surface}$$

The electrostatic energy is formulated as:

$$(6.10) \quad U_{electrostatic} = 2 \int u(r - r') d_r^3 d_{r'}^3 \rho(r) \rho(r')$$

where  $u(r - r')$  is the inter-particle electrostatic potential and is approximated as:

$$(6.11) \quad u(r - r') \propto l_B \frac{e^{-(r-r')/\lambda_d}}{|r - r'|}$$

Here, the Debye length  $\lambda \propto c^{-1/2}$ .  $\rho(r)$  is the charge density of the ribbon, and can be approximated as a constant  $\frac{N_T}{V}$ , where  $N_T$  is the ribbon charge and  $V$  is the ribbon volume. Therefore, we have

$$(6.12) \quad U_{electrostatic} = 2 \left( \frac{N_T}{V} \right)^2 k_B T \int l_B \frac{e^{-(r-r')/\lambda_d}}{|r - r'|} d_r^3 d_{r'}^3$$

Since for the  $C_{16}K_1$  ribbon, only the top and bottom surfaces are charged, the volume integral can first be thought of as a 2D integral. Let  $r - r' = \bar{r}$ .

$$(6.13) \quad U_{electrostatic} \propto 2\left(\frac{N_T}{V}\right)^2 V \delta k_B T \int \int_{W,L} l_B \frac{e^{-\bar{r}/\lambda_d}}{\bar{r}} d\bar{r}$$

or

$$(6.14) \quad U_{electrostatic} \propto 2\left(\frac{N_T}{V}\right)^2 V \delta k_B T l_B \int \int_{W,L} \frac{e^{-\sqrt{x^2+y^2}/\lambda_d}}{\sqrt{x^2+y^2}} dx dy$$

Here we distinguish between two conditions: low excess salt and high excess salt.

(1) At low excess salt condition,  $\lambda_d$  is very large,  $e^{-\sqrt{x^2+y^2}/\lambda_d} \approx 1 - \sqrt{x^2+y^2}/\lambda_d$ , thus

(6.14) becomes

$$(6.15) \quad U_{electrostatic} \propto 2\left(\frac{N_T}{V}\right)^2 V \delta k_B T l_B \int \int_{W,L} \left(\frac{1}{\sqrt{x^2+y^2}} - \frac{1}{\lambda_d}\right) dx dy$$

since

$$(6.16) \quad \int \int_{W,L} \frac{1}{\sqrt{x^2+y^2}} dx dy = \int_W \ln \left[ \frac{L}{x} + \sqrt{1 + \frac{L^2}{x^2}} \right] dx$$

So we have

$$(6.17) \quad U_{electrostatic} \propto 2\left(\frac{N_T}{V}\right)^2 V \delta k_B T l_B \left[ -\frac{WL}{\lambda_d} + \int_W \ln \left( \frac{L}{x} + \sqrt{1 + \frac{L^2}{x^2}} \right) dx \right]$$

(2) At high excess salt condition,  $\lambda_d$  is very small (sub nm). Therefore, electrostatic energy contributions are significant only over a small circle about the origin. Therefore,

the integral of  $\int \int_{W,L} \frac{e^{-\sqrt{x^2+y^2}/\lambda_d}}{\sqrt{x^2+y^2}} dx dy$ , it can be reformulated as,

$$(6.18) \quad \int \int_{W,L} \frac{e^{-\sqrt{x^2+y^2}/\lambda_d}}{\sqrt{x^2+y^2}} dx dy = \int_0^R \int_0^{2\pi} \frac{e^{-\frac{r}{\lambda_d}}}{r} r dr d\theta$$

The upper limit  $R$  can be chosen to be a few Debye Lengths such that the electrostatic energy term is negligible for  $r > R$ . The simplified integral here can be analytically solved, and the final result (6.19) shows that the electrostatic energy is independent of aspect ratio.

$$(6.19) \quad U_{electrostatic} \propto 4\left(\frac{N_T}{V}\right)^2 V \delta k_B T l_B \pi \lambda_d$$

Now we have the electrostatic part for our formulation. The interfacial energy part is simple,

$$(6.20) \quad U_{interface} = 2\gamma(L + W)\delta$$

Here  $\gamma$  is the surface tension for the hydrocarbon/water interface.

By combining Equation (6.20) with (6.17) and (6.19), we have the ribbon energy per unit volume in low and high salt conditions. Also based on AFM observations, we make a simplifying assumption that the total ribbon area  $A = WL$  is independent of aspect ratio  $\chi^{-1} = (L/W)$ . Thus we can substitute the  $W$  and  $L$  with ribbon area  $A$  and the inverse of aspect ratio  $\chi$ ,

$$(6.21) \quad \frac{U_{ribbon}}{V} = \left(\frac{2N_T^2}{VA}\right) k_B T l_B \left[ -\frac{A}{\lambda_d} + \int_0^{\sqrt{A\chi}} \ln \left( \frac{\sqrt{A/\chi}}{a} + \sqrt{1 + \frac{A}{\chi a^2}} \right) da \right] + \frac{2\gamma(\sqrt{A/\chi} + \sqrt{A\chi})}{A}$$

$$(6.22) \quad \frac{U_{ribbon}}{V} = \left(\frac{4N_T^2}{VA}\right)k_B T l_B \pi \lambda_d + \frac{2\gamma(\sqrt{A/\chi} + \sqrt{A\chi})}{A}$$

(6.21) (low salt) and (6.22) (high salt) are plotted in the main text to understand the relationship between ribbon energy and the ribbon aspect ratio  $\chi^{-1}$  different salt conditions.

The numerical values of parameters used in the calculation are listed below.

Table 6.1. Numerical values for the membrane model parameters in (6.21) and (6.22).

Parameter	Value	Notes
Ribbon area: $A$	$2 \times 10^{-12} m^2$	Estimated from AFM image
Ribbon thickness: $\delta$	$4 \times 10^{-9} m$	AFM scan and SAXS fitting
Ribbon volume: $V = A \times \delta$	$8 \times 10^{-21} m^3$	
Membrane charge density: $\rho$	$1.219 \times 10^{27} / m^3$	Estimated from WAXS results
Ribbon charge: $N_T = A \times \rho$	$1.56 \times 10^{-12} C$	
Bjerrum length: $l_B$	$0.7 nm$	
Surface tension: $\gamma$	$7.2 \times 10^{-2} J/m^2$	Hydrocarbon-water interfacial energy (ref [133])

#### 6.4.2. Step 2: Membrane rolling

In order to understand the rolling of the  $C_{16}K_1$  membrane, we used a simplified model of an array of charged species. The array was assumed to possess a spontaneous curvature  $C_0$ , and a contour length  $L_0$  that was independent of the curvature of the array (Fig. 6.10a). The array energy was assumed to be a sum of electrostatic repulsion energy and the curvature energy. The electrostatic repulsion energy for a straight array of charged species may be written as:

$$(6.23) \quad \frac{U_{electrostatic}}{L_0} = 2\rho^2 L_0 k_B T \int_{d_0}^{L_0} l_B \frac{e^{-l/\lambda_d}}{l} dl$$

Here,  $\rho$  is the membrane charge density and  $d_0$  is the nearest neighbor distance.

If the array had a curvature  $C_l$ , the intermolecular distances will become smaller, resulting in an increase in the electrostatic energy for the array. For instance, the distance between the two ends of the curved array  $L_0$  is smaller than  $L_0$ , and it can be written as

$$(6.24) \quad L'_0 = \frac{2}{c_1} \sin\left(\frac{c_1 L_0}{2}\right)$$

In particular, the electrostatic repulsion energy for case of curved array is

$$(6.25) \quad \frac{U_{electrostatic}}{L_0} = 2\rho^2 L_0 k_B T \int_{d_0}^{L_0} l_B \frac{e^{-\frac{2}{c_1} \sin(\frac{c_1 l}{2}) / \lambda_d}}{\frac{2}{c_1} \sin(\frac{c_1 l}{2})} dl$$

and the array curvature energy is

$$(6.26) \quad \frac{U_{curvature}}{L_0} = \frac{\kappa_c}{2} L_0 (C_1 - C_0)^2$$

where  $\kappa_c$  is the bending stiffness. Based on the nanotube diameter,  $C_0 \sim 1/(75nm)$ . Using Eq. 6.20 and 6.21, we calculated the total energy as a function of curvature  $C_1$  for different salt concentrations, which are discussed in the main text. The numerical values of model parameters are listed below.

### 6.4.3. Interbilayer separation in cochleates vs. salt concentration

In the main text, we used the sum of interlayer van der Waals attrac (6.6) and electrostatic repulsion (6.8) energy to calculate the equilibrium interlayer spacing  $D$  in the cochleates as a function of salt concentration  $c$ . The model parameters used in these calculations and their numerical values are listed below.

Table 6.2. Numerical values for the membrane model parameters in Eq. 6.20 and 6.21.

Parameter	Value	Notes
Molecular density along array: $\rho$	$2.438 \times 10^{11}/m$	Estimated from WAXS results
Bjerrum length: $l_B$	$0.7nm$	
Nearest neighbor distance: $d_0$	$5 \times 10^{-10}m$	Estimated from WAXS
Length of the charged array: $L_0$	$5 \times 10^{-8}m$	
Bending stiffness: $\kappa_c$	$2 \times 10^{-19}J$	DPPC crystalline bilayer membrane stiffness(ref[ <b>119</b> ])
Intrinsic curvature: $C_0$	$1/(75nm)$	Cryo-TEM image

Table 6.3. Numerical values for the membrane model parameters in (6.6) and (6.8).

Parameter	Value	Notes
Hamaker constant: $W$	$1.9 \times 10^{-22}J$	ref [ <b>134</b> ]
Temperature: $T$	$298K$	Room temperature
Bilayer thickness: $\delta$	$4 \times 10^{-9}m$	AFM and SAXS

#### 6.4.4. Curvature energy for cochleats

The curvature energy for a cylindrical bilayer membrane of area  $A$  and radius  $R_{cyl}$  is

$$(6.27) \quad U_{curvature} = \frac{\kappa_c}{2} \int_A (C_1 - C_0)^2 dA$$

where  $\kappa_c$  is the bending stiffness,  $C_1 = 1/R_{cyl}$  is the cylinder curvature, and  $C_0$  is the spontaneous curvature for the membrane. The above equation can be written as

$$(6.28) \quad U_{curvature} = \frac{\kappa_c}{2} L \int_l (C_1 - C_0)^2 dl$$

where  $L$  is the cochleate length, and  $l$  represents the contour length along the cochleate spiral. For a cochleate structure with interlayer spacing  $D$ , the radius of curvature at a

specific azimuthal angle  $\theta$  on the spiral takes the form

$$(6.29) \quad R_1 = \frac{D}{2\pi}\theta + R_i$$

where  $R_i$  is the internal radius of the cochleate. So we have

$$(6.30) \quad U_{curvature} = \frac{\kappa_c}{2}L \int_0^{\theta_o} \left(\frac{1}{\frac{D}{2\pi}\theta + R_i} - C_0\right)^2 \left(\frac{D}{2\pi}\theta + R_i\right) d\theta$$

where  $\theta_o$  is the azimuthal angle corresponding to the outermost end of the spiral, e.g. the outermost radius of cochleate  $R_o = \frac{D}{2\pi}\theta_o + R_i$ . Analytically solving Eq. 6.30 yields

$$(6.31) \quad U_{curvature} = \frac{\kappa_c L \pi}{2D} \left(2 \ln\left(\frac{R_o}{R_i}\right) - 4C_0(R_o - R_i) + (R_o^2 - R_i^2)C_0^2\right)$$

The cochleate membrane area  $A$  can be written as

$$(6.32) \quad A = \frac{\pi L}{D} (R_o^2 - R_i^2)$$

Therefore, the curvature energy per unit area

$$(6.33) \quad \frac{U_{curvature}}{A} = \frac{\kappa_c}{2(R_o^2 - R_i^2)} \left(2 \ln\left(\frac{R_o}{R_i}\right) - 4C_0(R_o - R_i) + (R_o^2 - R_i^2)C_0^2\right)$$

is dependent on the innermost and outermost radii of the cochleate, but does not depend on the interlayer spacing  $D$ . Therefore, for the purpose of calculating the equilibrium interlayer spacing  $D$  by minimization of the free energy, we neglect the effect of curvature energy.

## CHAPTER 7

**Ion dynamics in polyelectrolyte gels**

The content of this chapter is based on the following publication:

- Honghao Li, Aykut Erbas, Jos Zwanikken, and Monica Olvera de la Cruz. "Ionic conductivity in polyelectrolyte hydrogels." *Macromolecules* 49, no. 23 (2016): 9239-9246. [135]

**Abstract**

Transport of ionic species in heterogeneous polymeric media is highly dependent on the charge distributions and interactions between mobile and immobile groups. Here we perform coarsegrained molecular dynamics simulations to study the ion dynamics in swollen polyelectrolyte gels under external electric fields. A nonlinear response of the ionic conductivity to an applied electric field, for field strengths that are comparable to the ionic coupling strength, is observed. This behavior correlates to a broadening of the ionic distribution around the polymer backbone under an increasing electric field. Also, we find that the weak-field ionic mobility in gels increases with density, which is opposite to the behavior of simple electrolytes. This relates to the mean coupling between charges that decreases in gels, but increases in simple electrolytes, with increasing density. These results provide more insights into the electric response of polyelectrolyte gels to support the development of applications that combine electric and mechanical properties of polyelectrolyte gels for energy storage, sensing, selective transport, and signal transfer.

## 7.1. Introduction

As an important type of heterogeneous media, polyelectrolyte gels have already been used in applications in a broad range of fields such as drug delivery, superabsorbants, actuators, and artificial muscles [136, 137, 35, 138, 139, 140]. Polyelectrolyte gels are cross-linked polymer chains with charged groups covalently bonded to the backbones, while counterions dissolve into solvent as the only mobile charge species. The unique property as single-ion conductors has been used to synthesize ion-selective membranes which are especially important for applications mentioned above. For example, a practical and stable polyelectrolyte diode is reported by forming the interface of two hydrogel layers doped with oppositely charged polyelectrolytes, the oppositely charged counterions produce a nonlinear current response as a rectifying junction at the interface [29, 30]. In almost all practical electro dialysis processes, multiple electro dialysis cells with alternating anion and cation exchange membranes are arranged into an electro dialysis stack to remove ions. Anion (cation) membranes are polyelectrolyte gels with positively (negatively) charged groups, which rejects positively (negatively) charged ions and allows negatively (positively) charged ions to flow through.

Experimentally, ionic conductivity of polyelectrolyte gels has been measured in various conditions [141, 142, 143, 144, 145]. The ion dynamics in such heterogeneous media shows unique behaviors compared to other systems. For example, the concentration dependent ionic conductivity of polyelectrolyte gels is reported differently compared to polyelectrolytes solutions or binary electrolytes[146, 141]; while in electrolyte solutions, increasing concentration leads to a decrease in conductivity, for gels, a weak increase was observed with increasing monomer density. The conductivity can also be modulated by

counterion distribution by controlling the cross-linking density (i.e., the average molecular weight between crosslinkers) [147, 141]. Therefore, the morphology of polyelectrolyte gels at the nanometer scale is of paramount importance in improving membrane function and mechanical properties. However, usually only the relative amount of cross-linkers can be well controlled in experiments, leaving the chain lengths, entanglements, dangling ends almost impossible to determine. Hence, further design of such systems require theoretical determination of efficiency and the range of experimentally accessible parameters.

Here we use coarse-grained molecular dynamics (MD) simulations to investigate the ion dynamics in polyelectrolyte gels under external electric fields. We find a nonlinear response region where the molar ionic conductivity of polyelectrolyte gels increases with external fields. The counterion redistribution under electric fields is proposed as the driving mechanism. We also show that the ionic conductivity can be modulated by changing density of polyelectrolyte network particularly in the weak-field regime. A qualitative theory based on a field-induced weakening of binding energies can qualitatively describe the mobility of counterions for the range of external fields considered here. Our results also underline an essential difference between the ionic response in simple electrolyte solutions and that in polyelectrolyte gels. The simulations reveal underlying mechanisms that contribute to the average ionic response in charged polymeric systems, and suggest guidelines for tuning the conductivity in ion-conducting devices.

## 7.2. Model

Figure 7.1a illustrates the single cell of a defect-free cubic polyelectrolyte network that is used in simulations. The polymer segments connecting two network nodes are modelled

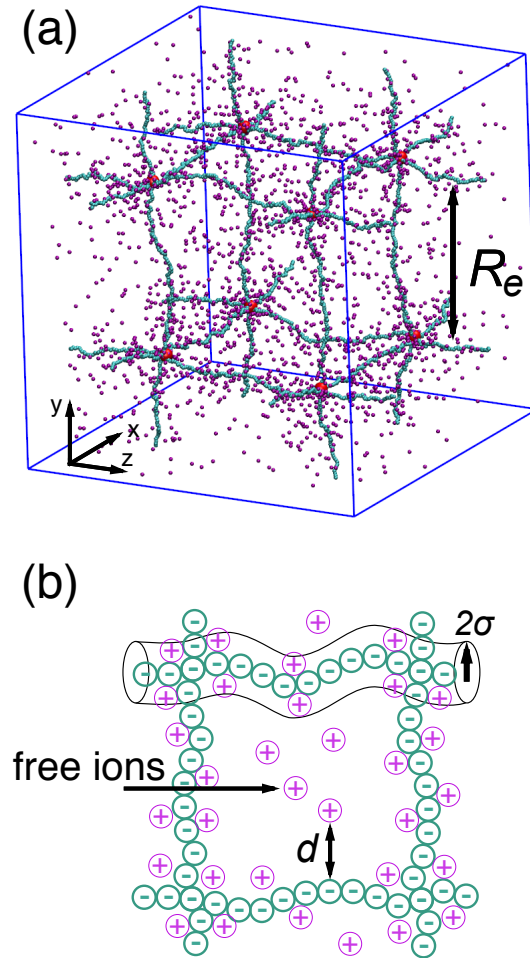


Figure 7.1. (a) Snapshot depicting a  $N = 100$  polyelectrolyte network structure. Monomers and counterions are denoted by cyan and purple spheres respectively. Every cross-linking node (drawn as oversized red spheres for illustration purpose) is attached by six polyelectrolyte chains, each of which has  $N$  monomers. Unit cell box in simulation typically has  $4 \times 4 \times 4$  cross-linking nodes ( $2 \times 2 \times 2$  shown here). (b) Illustration of the cell parameter that is used to determine condensed ion distributions. The distance from chain  $d$  is defined by the distance between an ion and its nearest monomer. The ion is considered as condensed ion when  $d \leq 2\sigma$ .

by bead-spring chains composed of  $N$  monomers. The steric and bonded interaction between monomers are calculated by the Lennard-Jones (LJ) and FENE (Finite Extension

Nonlinear Elastic) potentials in the forms of

$$U_{LJ}(r) = \begin{cases} 4\epsilon \left[ \left(\frac{\sigma}{r}\right)^{12} - \left(\frac{\sigma}{r}\right)^6 + \frac{1}{4} \right] & \text{for } r < r_c, \\ 0 & \text{for } r \geq r_c, \end{cases}$$

$$U_F(r) = \begin{cases} -\frac{1}{2}k_F r_F^2 \ln \left[ 1 - \left(\frac{r}{r_F}\right)^2 \right] & \text{for } r < r_F, \\ \infty & \text{for } r \geq r_F, \end{cases}$$

respectively. Here the LJ potential is shifted at the cutoff radius  $r = r_c$  to obtain a continuous potential profile.  $\sigma$  is the monomer diameter (LJ unit)<sup>1</sup>. Good solvent is modelled by  $r_c = 2^{1/6}\sigma$  and  $\epsilon = 1k_B T$ , leaving only the repulsive part of the interactions. This potential is employed for the mutual chain-counterion and counterion-counterion excluded volume interactions as well. For the FENE bond, the parameters are set to  $k_F = 10.0k_B T/\sigma^2$  and  $r_F = 1.5\sigma$  [148]. Periodic boundary conditions are applied in all direction in the simulation box. A typical cubic simulation box contains  $4 \times 4 \times 4$  cross-linking nodes in each direction. The sizes of simulation box for different gels are roughly in the range  $50\sigma - 200\sigma$ .

Each counterion has a valency of  $q = +1$  unit charge, while each backbone monomer of  $N$ -mer chains bears a unit charge of  $q = -1$ . Initially, counterions are added at random positions in the periodic simulations box. Due to the macroscopic requirements of electro-neutrality, number of counterions are set equal to the total number of charged backbone monomers. The short range pair-wise Coulomb interaction between two charges is  $U_C(r) = \epsilon l_B q_i q_j / r$ , where the Bjerrum length is  $l_B = e^2 / (4\pi\epsilon_0\epsilon_s\epsilon)$ . Here  $e$  is the unit

<sup>1</sup>In LJ unit, LAMMPS sets the fundamental quantities mass  $m$ , length  $\sigma$ , energy  $\epsilon$ , and the Boltzmann constant  $k_B$  equal to 1

charge,  $\epsilon_0$  and  $\epsilon_s$ : permittivity of the vacuum and the solvent respectively. The Bjerrum length is defined as the distance, at which two unit charges have an electrostatic interaction energy equivalent to thermal energy  $k_B T$ . As an example, for water  $l_B \approx 7.1 \text{ \AA}$  and is roughly equal to four adjacent carbon-carbon bonds. The long-range Coulomb interaction is calculated via the PPPM-algorithm [149], with a force accuracy of  $10^{-4}$ . The cut-off distance that determines the short and long range scheme in simulations is chosen to optimize the computation time between real and K-space. Typically, the range of the electrostatic cutoff distance ranges  $8\sigma - 20\sigma$  depending on the size of the system. [150]. Isothermal-isobaric ( $NPT$ ) ensemble is used to obtain equilibrium swelling size of gels by setting all pressure components to zero.

The non-equilibrium simulations are conducted by applying constant external electric field on each charged particle (i.e., the external force per monomer is  $\mathbf{F}_{ext} = q\mathbf{E}$ ) under  $NVT$  ensemble. The external electric fields are in the range of  $10^{-2} - 10^1 \epsilon/q\sigma$  and in the  $z$ -direction ( $\mathbf{E} = E\hat{z}$ ). The average drift velocity of all counterions relative to the polyelectrolyte network under the field is used to calculate the mobility of counterions as

$$(7.1) \quad \mu = \frac{\langle v_{ci} \rangle}{qE},$$

where the angular bracket  $\langle \dots \rangle$  refer to averaging over all the ions and time frames. The mobility of counterions can be related to the molar conductivity by  $\Lambda = q\mu$ . Additionally, diffusion coefficient of counterions at vanishing fields (i.e.,  $D \equiv k_B T \mu(E \rightarrow 0)$ ) is calculated from the simulation trajectories via

$$(7.2) \quad D = \lim_{t \rightarrow \infty} \frac{\langle [\mathbf{r}(t) - \mathbf{r}(0)]^2 \rangle}{6t},$$

where  $\mathbf{r}(t)$  is the position vector of ion at time  $t$ .

The molecular dynamics simulations were performed using LAMMPS software packages [151]. The Langevin (LGV) equation of motion are solved to iterate velocities and coordinates of particles. The equation of motion for particle  $i$

$$(7.3) \quad \dot{\mathbf{p}}_i = \mathbf{F}_i + \mathbf{F}_{ext,i} + \mathbf{F}_i^D + \mathbf{F}_i^R$$

where  $\mathbf{F}_i$  is the total bound and unbounded forces on the  $i$ th particle,  $\mathbf{F}_i^D = -\gamma\mathbf{v}_i$  is the dissipative force, where  $\gamma$  is the friction coefficient and  $\mathbf{v}_i$  is the particle velocity. The damping parameter is set to  $0.1\tau$  for all simulations in this work. Here  $\tau$  is the reduced time unit and defined as  $1\tau = (\frac{\epsilon}{m\sigma^2})^{1/2}t$ . Multiple values of damping factor are tested, and no qualitatively difference is found. The random force,  $\mathbf{F}_i^R$ , satisfies the fluctuation-dissipation theorem [152]. Typically  $10^6$  MD time steps ( $\Delta t = 0.005\tau$ ) are used to reach a steady state. Following, additional  $10^7$  time steps are run to obtain the data used in the analysis. The statistical errors of time-series data are analysed by using block averages as detailed in ref [153, 154]. Error bars of the order of the symbol size or smaller are not shown in the figures.

## 7.3. Results and Discussion

### 7.3.1. Polyelectrolyte gels in the absence of an external electric field

In polyelectrolyte networks, the osmotic pressure exerted by ionized counterions and the elastic response of the network chains determine the equilibrium size of the swelling ratio of network chains [155, 156]. The scaling theory [157, 158] gives the average end-to-end distance of the network chains in highly-swollen gels as  $R_e \simeq f^{1-\nu}N\sigma$ , where  $f$  is the

bear fraction of charge on backbone and  $\nu \approx 3/5$  is the Flory exponent for good solvent. In simulations, where we have strongly charged polyelectrolyte chains (i.e.,  $f = 1$ ),  $R_e$  linearly scales with  $N$  for various electrostatic strengths (Figure 7.2a). As the electrostatic strength (Bjerrum length) is increased, the polyelectrolyte gels are less swollen as a result of increasing attraction between backbone charges and counterions [159].

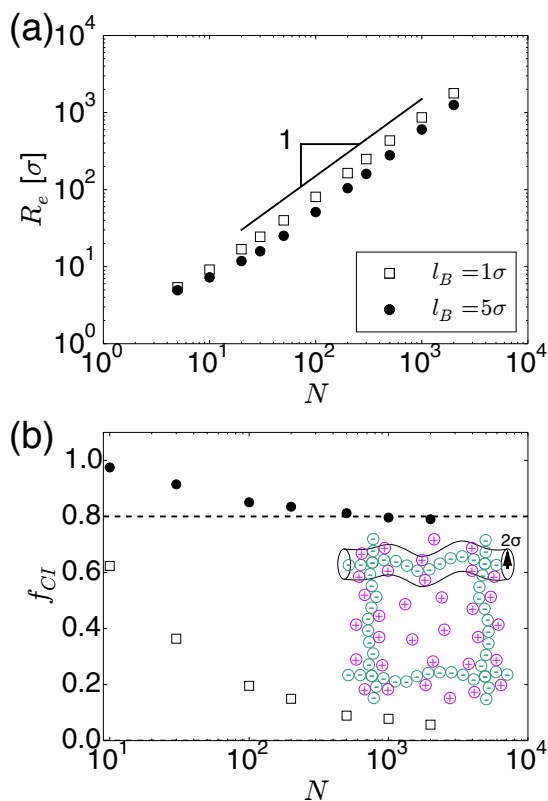


Figure 7.2. (a) Average end-to-end distance  $R_e$  of polyelectrolyte chains exhibit a linear scaling with  $N$  for both  $l_B = 1\sigma$  (empty square) and  $5\sigma$  (solid sphere). Due to the stronger electrostatic interaction,  $l_B = 5\sigma$  has a smaller  $R_e$  than its  $l_B = 1\sigma$  equivalence. A linear reference line is shown to guide the eye. (b) Fraction of condensed counterions  $f_{CI}$  at zero external electric field, all ions within a distance of  $2\sigma$  around the backbone chains are summed up. As  $N \rightarrow \infty$ , the counterion condensation ratio approaches the Manning theory (dashed line).

According to Manning's theory of condensation [147, 160], a single strongly charged and infinitely long charged rod attracts oppositely charged counterions to reduce its line charge density. Similar phenomena in polyelectrolyte gels has been reported in previous simulation studies [161, 159]. The simplified Manning model predicts the fraction of condensed counterions to be  $f_{CI} = 1 - 1/\xi$  for  $\xi > 1$ , where the Manning parameter  $\xi = l_B/l$  is defined as the Bjerrum length over the distance between two charges along the backbone chain, which is  $l = \sigma$  in our case.

An estimate for the fraction of condensed (non-free) counterions can be obtained by counting the ions confined in a cylindrical cell of radius  $2\sigma$  around each chain [162] (see also Figure 7.1b for the schematic definition). Figure 7.2b shows the calculated fraction of condensed counterions  $f_{CI}$  for various polyelectrolyte networks in the absence of external field. For dilute polyelectrolyte gels ( $N > 100$ ), the measured fraction of condensed counterions approaches the predicted Manning values,  $f_{CI} \rightarrow 0$  and  $f_{CI} = 0.8$ , for  $l_B = 1\sigma$  and  $l_B = 5\sigma$ , respectively (dashed line in Figure 7.2b). Although the counterion-condensation picture is valid for a single infinitely long chain, our results suggest that it is still qualitatively valid for ion distributions in gels in dilute limit. A more accurate method uses the inflection point based on Poisson-Boltzmann theory to estimate the counterion condensation around single chains [163, 164, 162], yet cannot be easily applied to arbitrary geometries such as networks in our simulations.

The transport properties of counterions are related to the fraction of condensed ions since electrostatic forces exerted on the counterions depends on their relative position with respect to the network chains. Figure 7.3 shows the counterion diffusion coefficient as a function of monomer concentration for  $l_B = 5\sigma$ . The diffusion coefficient decreases

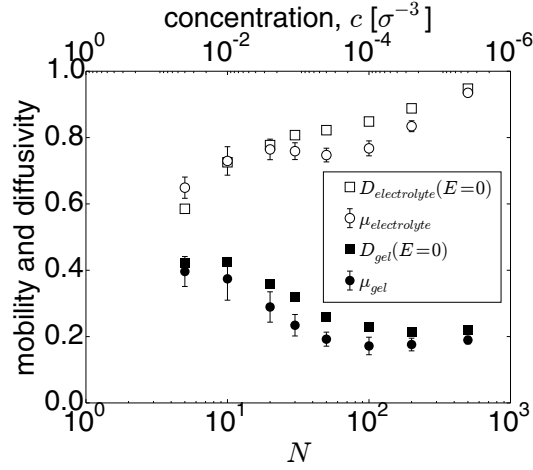


Figure 7.3. Comparison of linear-response mobilities  $\mu$  and equilibrium diffusivities  $D$  of counterions in gels and 1:1 simple electrolytes for an electrostatic strength of  $l_B = 5\sigma$ . The diffusion coefficients are calculated via mean square displacement of counterions (MSD) in Eq. 7.2 at zero field, whereas the mobilities are calculated via Eq. 7.1 at  $E = 0.1\epsilon/q\sigma$ . For comparison, polymerization degree  $N$  and monomer concentration  $c$  are related by using  $c \equiv N/R_e^3$  for gels and shown as an alternative x-axis (top axis).

as the size of the network chains is increased (i.e., monomer concentration is lowered). At low concentrations, the fraction of condensed ions converges to its Manning value (see Figure 7.2). Figure 7.3 also compares the diffusivity of ions in polyelectrolyte networks to that of 1 : 1 binary electrolytes with identical ionic concentrations. Unlike polyelectrolyte gels, in the electrolyte solution, diffusion of ions is faster for lower concentrations. At lower electrostatic strengths (i.e.,  $l_B = 1\sigma$ ), although the trend in diffusion coefficient is similar to  $l_B = 5\sigma$  case, the difference in mobilities at low and high concentrations are weaker (data not shown). This again indicates the dependence of averaged transport coefficients to the position of ions with respect to the backbone chains since, for  $l_B = 5\sigma$ , ions are more condensed onto network chains.

The equilibrium charge distribution and diffusion behavior in polyelectrolyte gels that we discuss so far is expected to be altered under external electric fields. In the following section, we discuss how the applied field alter the charge distribution and, in turn, mobility of mobile counterions in polyelectrolyte gels.

### 7.3.2. The effect of external field

Figure 7.4 shows counterion mobility in various polyelectrolyte networks  $N = 10, 30, 100$  for Bjerrum lengths  $l_B = 1\sigma, 5\sigma$ . To compare various cases on a single plot, all mobilities are normalized by their bulk value  $\mu_0 = 1/\gamma$ , where the Langevin friction term is  $\gamma$ .

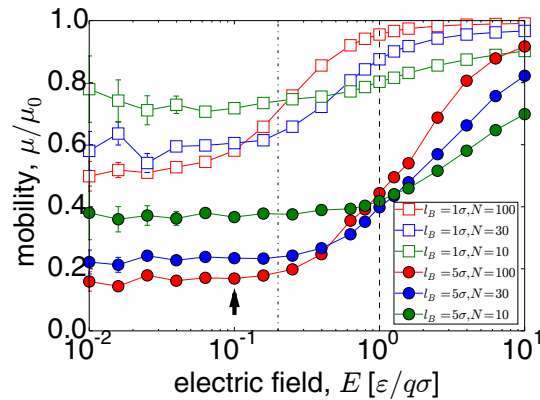


Figure 7.4. Mobility of counterions for various gels under external electric fields for both  $l_B = 1\sigma$  and  $l_B = 5\sigma$ . All the mobility values are rescaled by the Langevin damping parameter  $\mu_0 = 1/\gamma$ . Arrow indicates the value of the electric field ( $E = 0.1\epsilon/q\sigma$ ) that is used in Figure 7.3. Notice that this field is within the linear-response regime

Based on the data in Figure 7.4, for each polyelectrolyte network, the mobility of counterions under external an electric field  $E$  can be divided into three regimes. These regimes are

- (1) The mobility remains constant under the external electric fields of strength  $E < E^* \equiv \epsilon l_B / \sigma^2$ . This regime corresponds to the linear-response behavior for weak perturbations (e.g., Ohm's law is valid).
- (2) The linear-response regime ends at around  $E \simeq E^*$ , and a non-linear regime, where the mobility increases with increasing strength of electric field, sets in (Figure 7.4). The non-linear transition points are denoted by two dashed lines for  $l_B = 1\sigma$  and  $l_B = 5\sigma$ , respectively, and  $E_{l_B=5\sigma}^* / E_{l_B=1\sigma}^* \approx 5$ . Linear polyelectrolyte solutions also exhibit similar nonlinear response to external electric fields [165].
- (3) In the saturated regime, the external field  $E$  is strong enough and dominates over the Coulomb interactions. In this regime, the mobility of counterions becomes independent of the applied field and approaches its bulk value  $\mu \rightarrow \mu_0 = 1/\gamma$  for swollen gels.

In the linear regime, the electric field is not strong enough to alter the equilibrium distribution of charges and the related transfer properties significantly. This can be seen in Figure 7.3, where we compare the mobility values obtained at an electrical field strength within the linear regime,  $E = 0.1\epsilon/q\sigma$  (filled spheres in Figure 7.3) to the equilibrium diffusion coefficients (filled squares). Note that the diffusion coefficient and mobility are related via the Einstein relations,  $D = k_B T \mu$ . The linear-response mobility indeed converges to the equilibrium diffusion coefficients as  $E \rightarrow 0$ .

Within linear-response regime (i.e.,  $E < E^*$ ), interestingly the gels composed of shorter network chains exhibit slightly higher values of mobility (Figure 7.4). This is somewhat counter-intuitive since at high concentrations of charges (i.e., smaller values of  $N$ ), one can expect smaller values of mobilities similar to electrolyte solutions. However, the

distribution of free charges within the network of charged polymers alters the response to the external fields. In Figure 7.5a, we show the integrated distributions of counterions around the network chains as a function of the rescaled radial distance from the chain at  $E = 0.1\epsilon/q\sigma$  for various network chains. The data for  $l_B = 5\sigma$  are specifically chosen here to demonstrate the effect of condensation more clearly. Although the relative condensation volume, hence, condensation is more marked for networks of short chains (Figure 7.2), the counterion clouds near the chains are relatively more extended in the gels composed of short network chains due to mutual attraction by neighboring chains (Figure 7.5a). Indeed the average mobility of counterions is higher if they are away from the network chains as can be seen in the inset of Figure 7.5a): despite the noise in the data due to thermal fluctuations, the closer the counterions to the networks chains are, the slower they move. Hence, if the counterions are more scattered in the gel, the average mobility increases (Figure 7.5a).

The distance dependent mobility can be invoked by the distribution of electrostatic potential in polyelectrolyte gels. The electrostatic potential distribution of a polyelectrolyte network has been calculated using a two-dimensional stacking model [166], revealing the potential energy valleys around the polymer chains. The electrostatic potential for each counterion is calculated, and the results are shown in Figure 7.5b: these calculations also reveal the potential energy valleys around the polymer chains. Near the chains, deep potential wells are common in all networks. Away from the chains, the potentials decay to zero (Figure 7.5b). At intermediate distances between the backbone chains and counterions, the Coulomb potential is stronger for longer chains. This indicates that for a counterion located near, say  $N = 100$  network, escaping from the potential requires higher

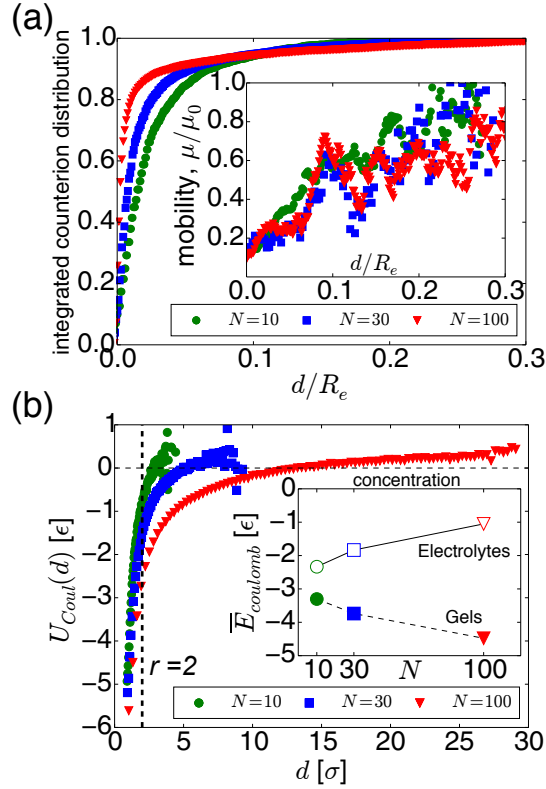


Figure 7.5. (a) Integrated ion distributions for various polyelectrolyte networks. The distance from chain  $d$  is normalized by the end-to-end distance  $R_e$ . Inset shows mobility of ions as a function of their distance from chains at  $E = 0.1\epsilon/q\sigma$  with  $l_B = 5\sigma$ . (b) The calculated electrostatic potentials for counterions as a function of the distance. Inset shows average Coulomb energy per counterion in various gels and 1:1 binary electrolytes at identical ionic concentrations at  $E = 0.1\epsilon/q\sigma$ .

forces compared to that in a  $N = 10$  network. Thus, the mobility of counterions can be smaller in dilute networks. Combined these results with the counterion distributions in various polyelectrolyte networks shown in Figure 7.5, the decrease in ionic mobility with increasing size of network chains in the linear-response regime can be related to distribution of counterions in dilute gels.

The linear regime ends when the strength of applied force approaches to that of the Coulomb forces between charged species (i.e.,  $qE \simeq l_B/\sigma^2$ ). To understand the underlying mechanism of the nonlinear mobility of counterions, the microscopic distribution of counterions is investigated at  $E > E^*$ . Indeed, strong electric fields are known to reduce the number of condensed counterions near the charged chains [165, 162]. In Figure 7.6a and b, we show the integrated distributions of counterions around chains of  $N = 100$  network as a function of the average radial distance from the chain for various electric field strengths. The values of the electric field correspond to both linear and non-linear regimes (Figure 7.4). For both  $l_B = 1\sigma$  and  $l_B = 5\sigma$  cases, at vanishing values of electric fields, the distributions are weakly affected by the external field as expected. However, at  $E > E^*$  the counterion distributions are broader as a result of the counterions departed away from the network chains. This can be seen more clearly in the 2D concentration profiles shown in Figure 7.6c for two different external fields,  $E = 0.1\epsilon/q\sigma$  and  $E = 1\epsilon/q\sigma$ . At the higher field, more ions occupy spaces between the network chains (notice the light and darker blue regions in Figure 7.6c). Indeed, there is an excellent correlation between the fraction of free ions and the mobility values for a wide range of external fields as shown in the inset of Figure 7.6a and b: the fraction of the free counterion as a function of external field overlaps with mobility data remarkably well.

Finally, in the saturation regime under strong fields, most of the condensed ions are stripped off the network chains, and dragged by the field. Indeed, when  $E$  is strong enough (i.e.,  $E \gg E^*$ ), the resulting mobility is expected to be independent of network properties and electrostatic coupling for highly swollen gels. Indeed, this is what we observe in the simulations (Figure 7.4). However, we should note that in the cases of dense gels (i.e., the

end-to-end distance does not obey the scaling  $R_e \sim N$ ) [167], the counterion diffusion can be coupled to chain motion. Thus, the final saturation values can be a function of crosslinking density or chains sizes.

Since the main contribution to the mobility in polyelectrolyte gels are from uncondensed (free) ions that can move through the network structure away from the chains, the mobility can be expressed as the sum of contributions from the free and condensed ions as

$$(7.4) \quad \mu = \mu_{nf}f_{CI} + \mu_{free}(1 - f_{CI}),$$

where  $\mu_{free}$  is mobility of free ions and  $\mu_{nf}$  is mobility of condensed ions. As a simple estimate, the fraction of condensation is  $f_{CI} \simeq 0.8$  for  $l_B = 5\sigma$ , thus Eq. 7.4 gives a value of mobility  $\mu \simeq 0.2\mu_0$ . However, Eq. 7.4 is less accurate for weak electrostatic strengths (e.g.,  $l_B \approx 1\sigma$  since a distinction between "condensed" and "free" ions is hard to establish due to weaker interactions between the ions and the backbone charges (e.g., on the order of thermal energy)).

### 7.3.3. Comparison: simple electrolytes versus polyelectrolyte gels

In 1 : 1 electrolytes in the dilute limit, according to Debye-Huckel theory, the molar conductivity  $\Lambda$  (which is proportional to diffusivity) decreases linearly with the square root of concentration,  $\Lambda = \Lambda^0 - K\sqrt{c}$  (Kohlrausch's law), where  $K$  is a constant, and  $\Lambda^0$  is the molar conductivity at infinite dilution (or limiting molar conductivity). Accordingly, a single diffusing ion feels a drag friction due to the surrounding ionic atmosphere of oppositely charged ions. The drag force increases with increasing concentration. Thus,

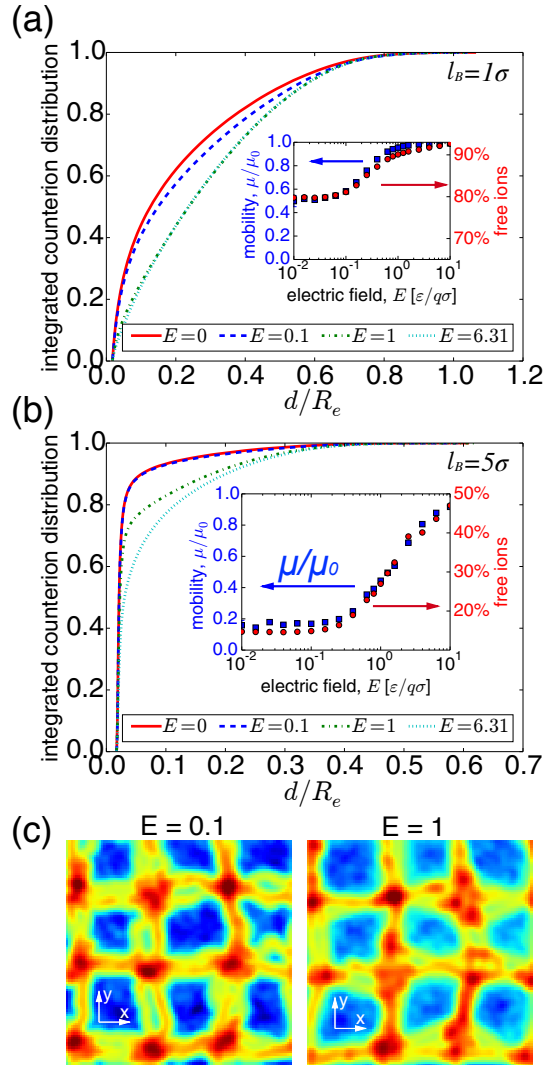


Figure 7.6. Integrated ion distribution around the chains of  $N = 100$  polyelectrolyte networks for various external electric fields (a)  $l_B = 1\sigma$  and (b)  $l_B = 5\sigma$ . The distance is normalized by the end-to-end distance  $R_e$ . Insets show mobility and number of free ions on a single plot. Blue squares denote the mobility values respect to left y axis, while red dots denote the fraction of free ions respect to right y axis. (c) 2D plots of counterions-concentration profiles are shown for  $E = 0.1\epsilon/q\sigma$  (left) and  $E = 1\epsilon/q\sigma$  (right), external field is in z-direction. The red regions refer to high local concentration of counterions around the network chains, whereas blue color refers to the low local concentration.

the ion diffusivity decreases with increasing concentration. In contrast, the ion diffusivity in polyelectrolyte gels increases with increasing concentration (Figure 7.3). Indeed, this distinct concentration dependence of ionic conductivity in gels and electrolytes were also observed experimentally [141].

A scaling argument can be made to invoke the difference between simple electrolytes and PE gels. In electrolytes, the average distance between two ions in solution can be estimated as  $\sim c^{-1/3}$ , where  $c$  is the concentration. Hence, the average distance decreases with increasing concentration (assuming no charge pairs are formed), resulting in stronger repulsions between like-charged ions and stronger attractions between oppositely charged ions. The inset of Figure 7.5b compares the average Coulomb energy per counterion in a 1:1 electrolyte solution in implicit solvent to those in various gels at  $E = 0.1\epsilon/q\sigma$ . For the electrolytes, the absolute value of the Coulomb energy increases with increasing concentration. In contrast, in polyelectrolyte gels, the absolute value of Coulomb energy decreases with increasing concentration. This behavior indicates an essential difference in ion distributions, which results in different ion dynamics in electrolytes and polyelectrolyte gels.

#### 7.3.4. Theoretical arguments for mobility

In order to rationalize the behavior of the mobility from a different perspective, we develop a theoretical model to refine equation (7.4) and the notion of 'free' and 'condensed'. We assume simple reaction equilibria, set by reaction constants  $K_i$ , connected to different states  $i$  of an ion. This rate constant is calculated from a single-ion partition function that depends on a mean binding (Gibbs) energy  $\Delta G(E)$ , depending on the external field

$E$ , and a volume  $V$  in which a single ion interacts with a site on the backbone,

$$(7.5) \quad K_i = V_i e^{\Delta G_i(E)}.$$

In addition, we distinguish three regions: 1) the region where the ions are 'free' ( $\Delta G_1 = 0$ ), 2) the region where the ions are close to the chain but still mobile ( $\Delta G_2 \sim 1k_B T$ ), and 3) the region where the ions are condensed and immobile ( $\Delta G_3 \gg 1k_B T$ ). The number of ions in each region,  $n_i$ , is determined by a reaction equilibrium,

$$(7.6) \quad n_i = n \frac{K_i}{K_1 + K_2 + K_3}.$$

We use an equation similar to equation (7.4) to estimate the total mobility, but now with three types of ions, corresponding to the three regions. Before we can make a comparison to the simulation results, many assumptions are required about the scaling behavior of  $V_i$  (the volume of region  $i$ ) and the mean free energy of binding, and in principle also the mobility in region 2, although this parameter appeared of little influence. The predictions of the model depend sensitively on these assumptions, especially on the scaling behavior of  $V_i$  and  $\Delta G_i(E)$ , and also on the input parameters. However, regardless of the specific assumptions, we find general trends that largely coincide with the simulation results, namely that the mobility increases with increasing field  $E$ , because a larger  $E$  shifts the reaction equilibria in favor of region 1 (the 'free' region), with a transition in the region where  $E$  has the same order of magnitude as the Coulomb pair interaction. The remarkable behavior in Figure 7.4a at small electric fields is, in contrast, only predicted for rather specific assumptions. An important assumption is that  $\Delta G$  in a dilute gel needs to be larger than in a more dense gel. That is, ions stick more strongly in dilute

networks. This assumption is confirmed by the simulation results in Figure 7.5b. The results are shown in Figure 7.7, under the assumption that the length of the chains scale linearly with  $N$ , and  $\Delta G$  linearly with  $E$ , for  $l_B = 5$ . We can draw two main conclusions from the perspective of this model. Firstly, the nonlinear response can be rationalized as a general consequence of ions breaking free from the polymer backbone, that are being less impeded by the interactions with the polymer chains as the electric field increases. Secondly, we conclude that the density-dependence of the mobility at low electric fields is not easily captured in a simple model, and only reproduced under very specific assumptions for the scaling behaviour of the gel volume and the binding energy of the ions. These assumptions are in line with the simulation results in the previous section. However, considering the simplifications in our theoretical models, and number of unknown parameters, the molecular dynamics simulations are necessary for conclusive results. The model highlights qualitative trends and suggests conditions for the required scaling behavior of the binding energy and gel swelling.

#### 7.4. Conclusion

We have analysed the ion dynamics in polyelectrolyte gels with molecular dynamics simulations, and invoked theoretical models to rationalize results. Regardless of the gel characteristics, we find a nonlinear response of the conductivity to an applied electric field, for field strengths that are comparable to the ionic coupling strength. This behavior correlates to a broadening of the ionic distribution around the polymer backbone under an increasing electric field. The weak-field mobility for dilute gels can be directly estimated from the fraction of free ions, using Manning's theory, if the ionic coupling is larger than

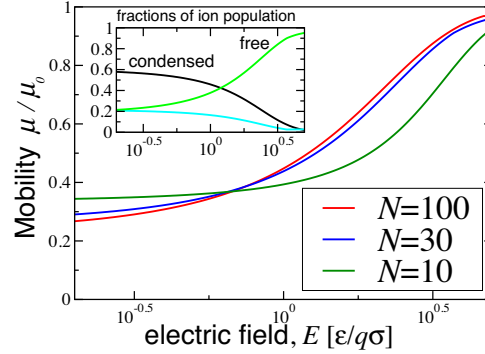


Figure 7.7. Mobility as a function of the applied electric field. The mobility increases with the electric field, as the reaction equilibria shift toward the region where ions move freely (i.e. ions break free from the gel backbone). The contrast in the mobility is larger for dilute gels ( $N = 100$ ). Under specific assumptions, the (relative) mobility at zero field is lower in dilute gels than the more dense gels. The simulations were required to confirm these assumptions, and to show the same qualitative trend without these assumptions. The inset shows the fraction of the ion population in each of the three regions as a function of  $E$ , for  $N = 30$ .

the thermal energy,  $l_B/\sigma > 1$ . For dense gels, the mobility is not easily estimated due to the complicated interplay of Coulomb interactions and steric repulsions. We find that the ion mobility in dilute gels shows a larger transition than in denser gels, and we connected the behavior to a larger binding energy of the ions to the polymer backbone. Remarkably, we find that the small-field ion mobility in polyelectrolyte gels increases with increasing concentration, which is opposite to the behavior observed in simple electrolytes. This is related to the mean coupling between charges, which decreases in polyelectrolyte gels and increases in simple electrolytes, with increasing concentration. These results provide more insight into the electric response of polyelectrolyte gels, to support the development of applications that combine electric and mechanical properties of polyelectrolyte gels for energy storage, sensing, selective transport, and signal transfer.

## CHAPTER 8

**Summary and Outlook****8.1. Summary**

Electrostatic interactions are of fundamental importance for understanding the relationships between structure and function in many biological and physical systems. There are great challenges in solving electrostatics problem in complex electrolytes computationally. In this thesis, I first extend previous variational formulations to solve polarization for multiple interfaces. I develop a molecular dynamics simulation package from scratch and this package is used by Meng Shen and me to study the surface polarization effects on ion-containing emulsions [1]. Using explicit calculation of induced charges and separation of electrostatic inter-droplet interaction, our work provides a clear understanding behind the intertwined relation between surface polarization and ion distribution. Besides finding strong attractions between droplets with multivalent ions in agreement with all-atom metalloamphiphile extraction studies [20], we find the orientation of the charges in the droplets is strongly affected by the surface polarization and hence the ion-ion interaction between the droplets; these interactions decrease as the ion size and valency decreases. Our studies reveal the role of dielectric mismatch on inter-droplet interactions. While ion-containing oil aggregates in aqueous solutions interact very weakly with each other, much weaker than in the case of simulations that do not include surface polarization, in organic solvents the interactions between water droplets are strongly enhanced due to

surface polarization. This understanding helps building meaningful models for analyzing interactions between ion containing emulsions and microcompartments [43], and paves the way for understanding self-assembly of mixed phases for multiple applications.

Then I work with Trung D. Nguyen to implement our variational method in to the well-known open-source molecular dynamics simulator (LAMMPS). We use this module to study the ion distribution near structured polarizable surface. Together with Huanxin Wu in professor Erik Luijten's group, We find the local curvature of the surface always induces effective surface polarization and net ion charge accumulation in the presence of asymmetric electrolytes. The effect should be observable not only on surfaces that bound an electrolyte, but also at the surface of electrolyte-immersed colloids. Our findings can be applied to the design of surfaces with useful physicalchemical properties. I also further investigate the case where there are charged amphiphile molecules at the interface.

I develop a Monte-Carlo simulation package to capture the dynamical dissociation of charges of molecules. Collaborated with experiments (Mitchell Miller in professor Pulak Dutta's group), we study the intra-lanthanide selectivity during solvent extraction. This study shows that strong elemental selectivity in the solvent extraction process occurs at the interface between aqueous and organic phases. Erbium (the heavier and smaller lanthanide) is attracted to a Langmuir monolayer of extractant-like molecules even at much lower bulk concentrations than neodymium. When both metals are present in the solution, erbium is the dominant surface adsorbant even when much more neodymium is present in the bulk. Using a theoretical model and Monte Carlo simulations, we find that electrostatic effects arising from the inhomogeneity of the interfacial medium and small differences between ions are responsible for this strong selectivity between these

two chemically similar ions. Our results imply that the interface plays the essential role in separating lanthanides during solvent extraction. We therefore suggest that efforts to understand, modify and improve lanthanide (and perhaps also actinide) separations processes should focus on the unusual chemical environment of the interface.

Collaborated with Changrui Gao in professor Michael J. Bedzyk's group, We use Monte-Carlo simulations and pH titration measurements to reveal that ionic correlations in the PA assemblies shift the ionizable amine  $\text{pK} \sim 8$  from  $\text{pK} \sim 10$  in the lysine headgroup. We also use simplified theoretical models explain that that the reduction in the range of electrostatic interactions is the driving force for high aspect ribbons isotropic sheets membrane rolling transformations. The linear relationship between the interbilayer separation and the screening length was qualitatively explained by considering the interplay between attractive van der Waals' and the repulsive electrostatic energies. These results suggest that the salt-induced structural transitions in the  $C_{16}K_1$  system should also be observable in other charged bilayer membranes that possess a spontaneous curvature. Our combined experimental and theoretical study yields insight into attaining the cochleate structures and controlling their internal architecture. The results presented here should be useful for optimizing the structure and function of cochleates in many applications, including drug delivery and photocatalytic production of hydrogen.

At last, I discuss ion dynamics simulations. We have analysed the ion dynamics in polyelectrolyte gels with molecular dynamics simulations, and invoked theoretical models to rationalize results. Regardless of the gel characteristics, we find a nonlinear response of the conductivity to an applied electric field, for field strengths that are comparable to the ionic coupling strength. This behavior correlates to a broadening of the ionic

distribution around the polymer backbone under an increasing electric field. The weak-field mobility for dilute gels can be directly estimated from the fraction of free ions, using Manning’s theory, if the ionic coupling is larger than the thermal energy,  $l_B/\sigma > 1$ . For dense gels, the mobility is not easily estimated due to the complicated interplay of Coulomb interactions and steric repulsions. We find that the ion mobility in dilute gels shows a larger transition than in denser gels, and we connected the behavior to a larger binding energy of the ions to the polymer backbone. Remarkably, we find that the small-field ion mobility in polyelectrolyte gels increases with increasing concentration, which is opposite to the behaviour observed in simple electrolytes. This is related to the mean coupling between charges, which decreases in polyelectrolyte gels and increases in simple electrolytes, with increasing concentration. These results provide more insight into the electric response of polyelectrolyte gels, to support the development of applications that combine electric and mechanical properties of polyelectrolyte gels for energy storage, sensing, selective transport, and signal transfer.

## 8.2. Ongoing project: Comparison of different polarization solvers

As mentioned, it is very important to develop a fast and efficient polarization solver for many problems. Currently, our variational method implemented LAMMPS can deal with systems with thousands of discretized interface patches for a typical molecular dynamics simulation ( $> 10^7$  timesteps), even without perfect parallelization. However, for significant larger system. It is necessary to make the code parallel computable. Also, it is a good practice to compare different methods and find the best one for different scenarios.

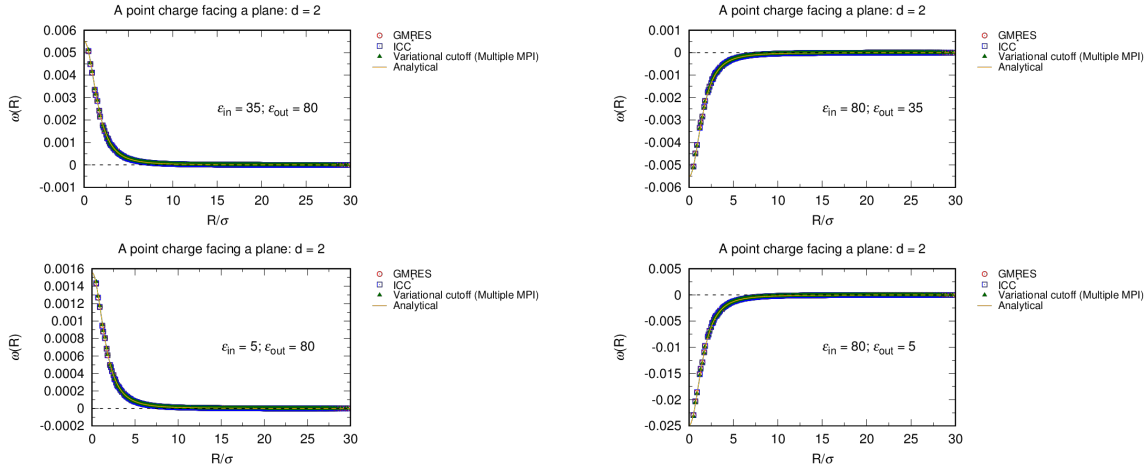


Figure 8.1. Induced charge of plane.

Here are the preliminary results Trung D. Nguyen has done to compare three different polarization solvers (ICC [168], GMRES [12], variational method [15]) for three different simple geometries (plane, cylinder and sphere) which with analytical results. The curves “Variational cutoff” are his new implementation of the direct optimization (inverse matrix calculation) adopted from implementation which use full sized matrices (“Variational  $M^2$ ”), cutoff =  $20\sigma$  for these tests. For a point charge inside the sphere and  $\epsilon_{in} \gg \epsilon_{out}$ , the discrepancy between the numerical results from the solvers and analytical results can be reduced by increasing the number of mesh points.

### 8.3. Promising project: Ion dynamics in dielectric media

Combined what we have investigated, it is meaningful to study the ion dynamics in media with inhomogeneous dielectrics. Here I propose to study the ionic transport in nanochannels (Figure 8.4) with different concentrations, channel sizes, ion sizes and dielectric constants. From my previous test, such system would need lots of discretization points of interface ( $> 6000$  for a tube with 5nm diameter) to get an accurate result of

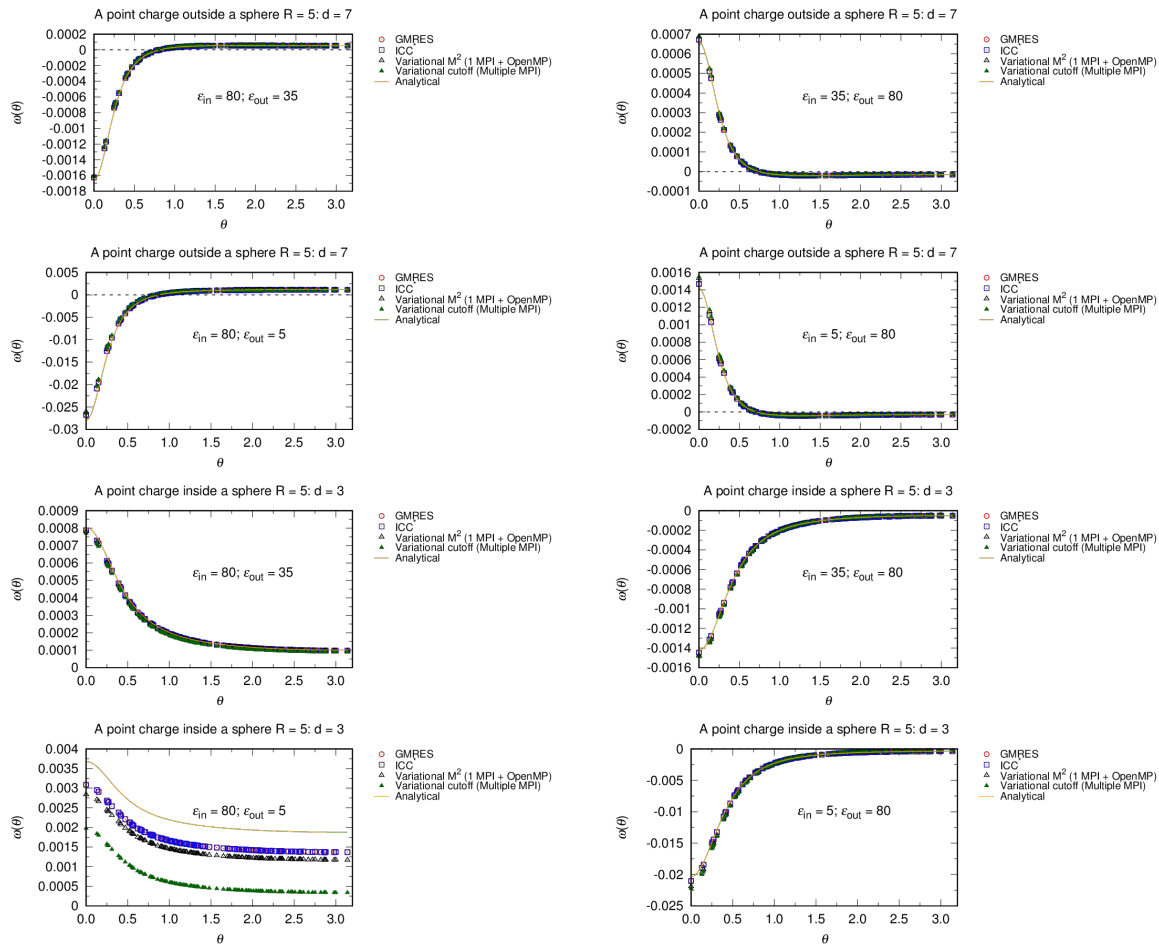


Figure 8.2. Induced charge of sphere.

induced charge. It is only possible after we find the most efficient method/implementation mentioned in previous section. There are several problems we could study.

First, the equilibrium ion distribution in nanochannel could be studied. Various ion sizes, nanochannel sizes, dielectric mismatches will be considered. Note asymmetric salt, such as  $MgCl_2$  and  $AlCl_3$ , appears widely in chemical or biological systems. Because the magnitude of dielectric effects scales as  $z^2$ , where  $z$  is the valence of an ion, multivalent ions experience much stronger image repulsion/attraction than monovalent ions. This would

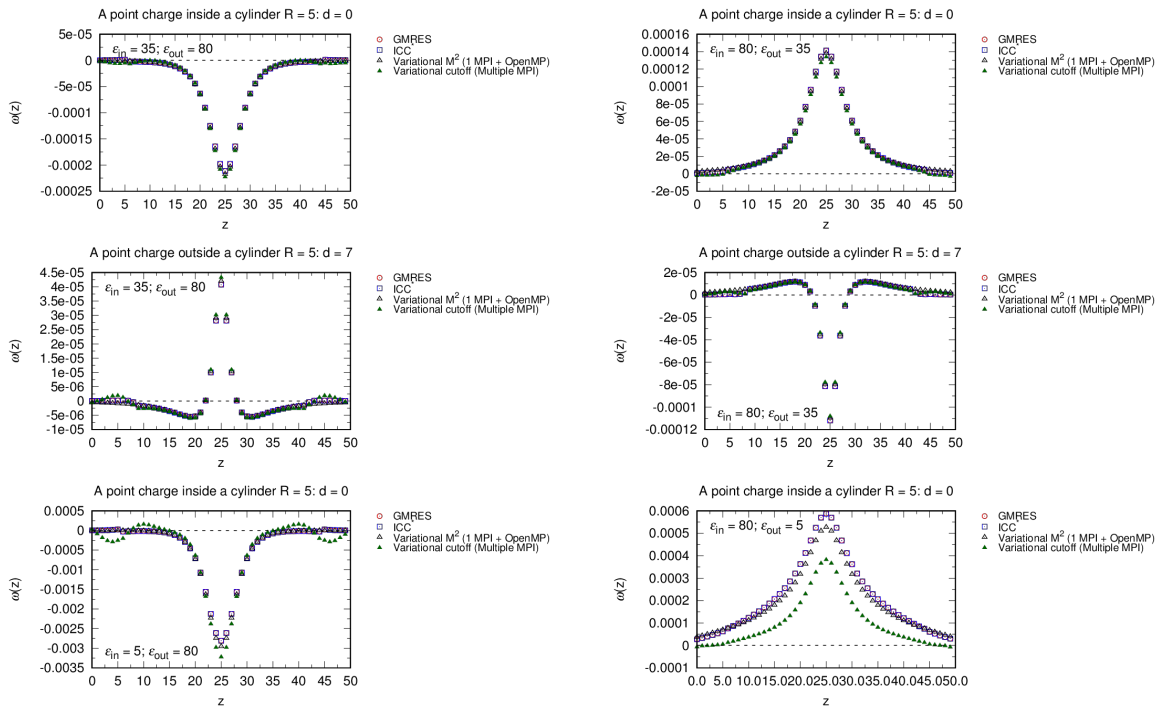


Figure 8.3. Induced charge of cylinder.

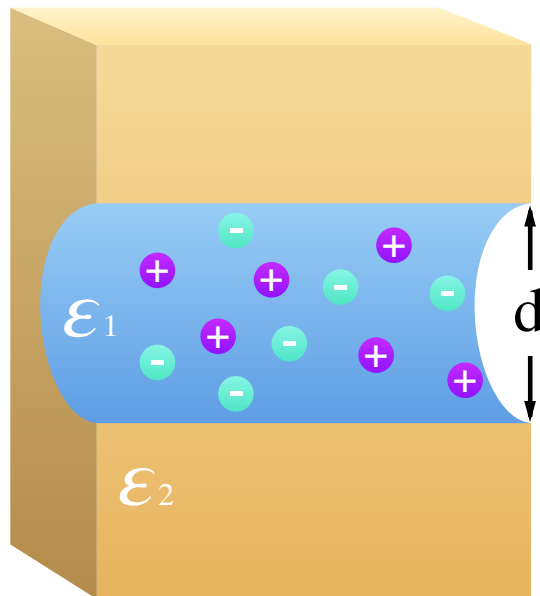


Figure 8.4. System we are going to study: Ionic transport in nanchannel.

cause different ion distribution for monovalent ion and divalent/trivalent ion, especially for interface with curvatures. We could also charge the interface with a gate voltage, the net charge distribution on the interface would greatly tune free ions distribution in nanochannel.

Then, by applying an external electric field along the nanochannel. The electric field is known to alter the ion distribution thus result in non-trivial ion dynamics according to the previous chapter. Moreover, the interaction between free ions and polarized charge on the interface would greatly expand our knowledge in ion dynamics and nanofuidics.

Finally, more geometries other than cylindrical channel, such as conical channels and curved tubes could be studied. Conical shaped pores have application in ion pumps [169], which could bring novel phenomenal to this system.

## References

- [1] Meng Shen, Honghao Li, and Monica de la Cruz. Surface Polarization Effects on Ion-Containing Emulsions. *Phys. Rev. Lett.*, 119(13):138002, sep 2017.
- [2] B Honig and A Nicholls. Classical electrostatics in biology and chemistry. *Science*, 268(5214):1144–1149, 1995.
- [3] MF Perutz. Electrostatic effects in proteins. *Science*, 201(4362):1187–1191, 1978.
- [4] David E Clapham. Calcium signaling. *Cell*, 131(6):1047–1058, 2007.
- [5] Yan Levin. Strange electrostatics in physics, chemistry, and biology. *Physica A: Statistical Mechanics and its Applications*, 352(1):43–52, 2005.
- [6] Frank H. J. van der Heyden, Derek Stein, Koen Besteman, Serge G. Lemay, and Cees Dekker. Charge inversion at high ionic strength studied by streaming currents. *Phys. Rev. Lett.*, 96:224502, Jun 2006.
- [7] Francisco J. Solis, Graziano Vernizzi, and Monica Olvera de la Cruz. Electrostatic-driven pattern formation in fibers, nanotubes and pores. *Soft Matter*, 7:1456–1466, 2011.
- [8] Graziano Vernizzi and Monica Olvera de la Cruz. Faceting ionic shells into icosahedra via electrostatics. *Proceedings of the National Academy of Sciences*, 104(47):18382–18386, 2007.
- [9] S. Sacanna, W. K. Kegel, and A. P. Philipse. Thermodynamically stable pickering emulsions. *Phys. Rev. Lett.*, 98:158301, Apr 2007.
- [10] Jörg Rottler and A. C. Maggs. Local molecular dynamics with coulombic interactions. *Phys. Rev. Lett.*, 93:170201, Oct 2004.
- [11] Kipton Barros and Erik Luijten. Dielectric effects in the self-assembly of binary colloidal aggregates. *Physical review letters*, 113(1):017801, 2014.

- [12] Kipton Barros, Daniel Sinkovits, and Erik Luijten. Efficient and accurate simulation of dynamic dielectric objects. *The Journal of chemical physics*, 140(6):064903, 2014.
- [13] Xikai Jiang, Jiyuan Li, Xujun Zhao, Jian Qin, Dmitry Karpeev, Juan Hernandez-Ortiz, Juan J de Pablo, and Olle Heinonen. An  $O(N)$  and parallel approach to integral problems by a kernel-independent fast multipole method: Application to polarization and magnetization of interacting particles. *The Journal of Chemical Physics*, 145(6):064307, 2016.
- [14] Jian Qin, Jiyuan Li, Victor Lee, Heinrich Jaeger, Juan J de Pablo, and Karl F Freed. A theory of interactions between polarizable dielectric spheres. *Journal of colloid and interface science*, 469:237–241, 2016.
- [15] Vikram Jadhao, Francisco J Solis, and Monica Olvera de la Cruz. Simulation of charged systems in heterogeneous dielectric media via a true energy functional. *Physical review letters*, 109(22):223905, 2012.
- [16] Vikram Jadhao, Francisco J Solis, and Monica Olvera De La Cruz. A variational formulation of electrostatics in a medium with spatially varying dielectric permittivity. *The Journal of chemical physics*, 138(5):054119, 2013.
- [17] Satoshi Ogawa, Eric A Decker, and D Julian McClements. Influence of environmental conditions on the stability of oil in water emulsions containing droplets stabilized by lecithin- chitosan membranes. *Journal of Agricultural and Food Chemistry*, 51(18):5522–5527, 2003.
- [18] David Gauthier, Pierre Baillargeon, Marc Drouin, and Yves L Dory. Self-assembly of cyclic peptides into nanotubes and then into highly anisotropic crystalline materials. *Angewandte Chemie International Edition*, 40(24):4635–4638, 2001.
- [19] Feng Xie, Ting An Zhang, David Dreisinger, and Fiona Doyle. A critical review on solvent extraction of rare earths from aqueous solutions. *Minerals Engineering*, 56:10–28, 2014.
- [20] Baofu Qiao, Geoffroy Ferru, Monica Olvera de la Cruz, and Ross J Ellis. Molecular origins of mesoscale ordering in a metalloamphiphile phase. *ACS central science*, 1(9):493, 2015.
- [21] Baofu Qiao, John V Muntean, Monica Olvera de la Cruz, and Ross J Ellis. Ion transport mechanisms in liquid–liquid interface. *Langmuir*, 33(24):6135–6142, 2017.

- [22] Baofu Qiao, Thomas Demars, Monica Olvera de la Cruz, and Ross J Ellis. How hydrogen bonds affect the growth of reverse micelles around coordinating metal ions. *The journal of physical chemistry letters*, 5(8):1440–1444, 2014.
- [23] J Rey, S Dourdain, L Berthon, J Jestin, S Pellet-Rostaing, and T Zemb. Synergy in extraction system chemistry: combining configurational entropy, film bending, and perturbation of complexation. *Langmuir*, 31(25):7006–7015, 2015.
- [24] C Fritzmann, J Löwenberg, T Wintgens, and T Melin. State-of-the-art of reverse osmosis desalination. *Desalination*, 216(1):1–76, 2007.
- [25] H Strathmann. Electrodialysis, a mature technology with a multitude of new applications. *Desalination*, 264(3):268–288, 2010.
- [26] AH Heuer, DJ Fink, VJ Laraia, JL Arias, PD Calvert, K Kendall, GL Messing, J Blackwell, PC Rieke, DH Thompson, and al. et. Innovative materials processing strategies: a biomimetic approach. *Science*, 255(5048):1098, 1992.
- [27] Mohsen Shahinpoor. Ionic polymer–conductor composites as biomimetic sensors, robotic actuators and artificial muscles: a review. *Electrochimica Acta*, 48(14):2343–2353, 2003.
- [28] Rohit Karnik, Rong Fan, Min Yue, Deyu Li, Peidong Yang, and Arun Majumdar. Electrostatic control of ions and molecules in nanofluidic transistors. *Nano letters*, 5(5):943–948, 2005.
- [29] Olivier J Cayre, Suk Tai Chang, and Orlin D Velev. Polyelectrolyte diode: nonlinear current response of a junction between aqueous ionic gels. *Journal of the American Chemical Society*, 129(35):10801–10806, 2007.
- [30] Hyung-Jun Koo, Suk Tai Chang, and Orlin D Velev. Ion-current diode with aqueous gel/sio2 nanofilm interfaces. *Small*, 6(13):1393–1397, 2010.
- [31] Rong Fan, Seong Huh, Ruoxue Yan, John Arnold, and Peidong Yang. Gated proton transport in aligned mesoporous silica films. *Nature materials*, 7(4):303–307, 2008.
- [32] Hirofumi Daiguji, Peidong Yang, and Arun Majumdar. Ion transport in nanofluidic channels. *Nano Letters*, 4(1):137–142, 2004.
- [33] Sung-Wook Nam, Michael J Rooks, Ki-Bum Kim, and Stephen M Rosnagel. Ionic field effect transistors with sub-10 nm multiple nanopores. *Nano letters*, 9(5):2044–2048, 2009.

- [34] Niels Boon and Monica Olvera de la Cruz. softamplifier circuits based on field-effect ionic transistors. *Soft matter*, 11(24):4793–4798, 2015.
- [35] Christoph Keplinger, Jeong-Yun Sun, Choon Chiang Foo, Philipp Rothemund, George M Whitesides, and Zhigang Suo. Stretchable, transparent, ionic conductors. *Science*, 341(6149):984–987, 2013.
- [36] Can Hui Yang, Baohong Chen, Jing Jing Lu, Jian Hai Yang, Jinxiong Zhou, Yong Mei Chen, and Zhigang Suo. Ionic cable. *Extreme Mechanics Letters*, 3:59 – 65, 2015.
- [37] Michel Armand. The history of polymer electrolytes. *Solid State Ionics*, 69(3):309 – 319, 1994.
- [38] Francisco J Solis, Vikram Jadhao, and Monica Olvera De La Cruz. Generating true minima in constrained variational formulations via modified lagrange multipliers. *Physical Review E*, 88(5):053306, 2013.
- [39] Edward Y Kim and Danielle Tullman-Ercek. A rapid flow cytometry assay for the relative quantification of protein encapsulation into bacterial microcompartments. *Biotechnology journal*, 9(3):348–354, 2014.
- [40] Cui Zhang, Francois Gygi, and Giulia Galli. Strongly anisotropic dielectric relaxation of water at the nanoscale. *The Journal of Physical Chemistry Letters*, 4(15):2477–2481, 2013.
- [41] Nicolas Giovambattista, Peter J Rossky, and Pablo G Debenedetti. Effect of pressure on the phase behavior and structure of water confined between nanoscale hydrophobic and hydrophilic plates. *Physical Review E*, 73(4):041604, 2006.
- [42] Mike P Allen and Dominic J Tildesley. *Computer simulation of liquids*. Oxford university press, 1989.
- [43] Todd O Yeates, Cheryl A Kerfeld, Sabine Heinhorst, Gordon C Cannon, and Jessup M Shively. Protein-based organelles in bacteria: carboxysomes and related microcompartments. *Nature Reviews Microbiology*, 6(9):681–691, 2008.
- [44] Patrice Simon and Yury Gogotsi. Materials for electrochemical capacitors. 7(11):845–854, 2008.
- [45] Osamu Shirai, Sorin Kihara, Yumi Yoshida, and Masakazu Matsui. Ion transfer through a liquid membrane or a bilayer lipid membrane in the presence of sufficient electrolytes. 389(1-2):61–70, 1995.

- [46] C Wagner. Die Oberflächenspannung verdünnter Elektrolytlösungen. 25:474–477, 1924.
- [47] Lars Onsager and Nicholas N T Samaras. The Surface Tension of Debye-Hückel Electrolytes. 2(8):528–536, 1934.
- [48] Jean-Pierre Hansen and Hartmut Löwen. Effective interactions between electric double layers. 51(1):209–242, 2000.
- [49] David C Grahame and Roger Parsons. Components of charge and potential in the inner region of the electrical double layer: aqueous potassium chloride solutions in contact with mercury at 25. 83(6):1291–1296, 1961.
- [50] Marco Favaro, Beomgyun Jeong, Philip N Ross, Junko Yano, Zahid Hussain, Zhi Liu, and Ethan J Crumlin. Unravelling the electrochemical double layer by direct probing of the solid/liquid interface. 7, 2016.
- [51] Luc Belloni. Ionic condensation and charge renormalization in colloidal suspensions. *Colloids and Surfaces A: Physicochemical and Engineering Aspects*, 140(1):227–243, 1998.
- [52] A Y Grosberg, T T Nguyen, and B I Shklovskii. The physics of charge inversion in chemical and biological systems. 74:329–345, 2002.
- [53] Yan Levin. Electrostatic correlations: from plasma to biology. 65:1577–1632, 2002.
- [54] Otto Stern. Zur Theorie der elektrolytischen Doppelschicht. *Berichte der Bunsengesellschaft für Physikalische Chemie*, 30(21-22):508–516, 1924.
- [55] Kurt Andresen, R Das, Hye Yoon Park, H Smith, Lisa W Kwok, Jessica S Lamb, E J Kirkland, D Herschlag, K D Finkelstein, and Lois Pollack. Spatial distribution of competing ions around DNA in solution. 93(24):248103, 2004.
- [56] J E B Randles. Structure at the free surface of water and aqueous electrolyte solutions. *Physics and Chemistry of Liquids*, 7(1-2):107–179, 1977.
- [57] Guangming Luo, Sarka Malkova, Jaesung Yoon, David G Schultz, Binhua Lin, Mati Meron, Ilan Benjamin, Petr Van\`ysek, and Mark L Schlossman. Ion distributions near a liquid-liquid interface. 311(5758):216–218, 2006.
- [58] Itamar Borukhov, David Andelman, and Henri Orland. Steric effects in electrolytes: A modified poisson-boltzmann equation. *Physical review letters*, 79(3):435, 1997.

- [59] Douglas Henderson. Recent progress in the theory of the electric double layer. *Progress in Surface Science*, 13(3):197–224, 1983.
- [60] Marcelo Lozada-Cassou, Rafael Saavedra-Barrera, and Douglas Henderson. The application of the hypernetted chain approximation to the electrical double layer: Comparison with Monte Carlo results for symmetric salts. 77(10):5150–5156, 1982.
- [61] Mingnan Ding, Bing-Sui Lu, and Xiangjun Xing. Charged plate in asymmetric electrolytes: One-loop renormalization of surface charge density and Debye length due to ionic correlations. 94(4):42615, 2016.
- [62] Yan Levin. Polarizable ions at interfaces. *Physical review letters*, 102(14):147803, 2009.
- [63] Tamás Pajkossy. Impedance of rough capacitive electrodes. 364(1-2):111–125, 1994.
- [64] LI Daikhin, AA Kornyshev, and M Urbakh. Double-layer capacitance on a rough metal surface. *Physical Review E*, 53(6):6192, 1996.
- [65] Eric M Vrijenhoek, Seungkwan Hong, and Menachem Elimelech. Influence of membrane surface properties on initial rate of colloidal fouling of reverse osmosis and nanofiltration membranes. *Journal of Membrane Science*, 188(1):115–128, 2001.
- [66] Subir Bhattacharjee, Chun-Han Ko, and Menachem Elimelech. Dlvo interaction between rough surfaces. *Langmuir*, 14(12):3365–3375, 1998.
- [67] W Richard Bowen and Teodora A Doneva. Atomic force microscopy studies of membranes: effect of surface roughness on double-layer interactions and particle adhesion. *Journal of colloid and interface science*, 229(2):544–549, 2000.
- [68] W Richard Bowen, Teodora A Doneva, and J Austin G Stoton. The use of atomic force microscopy to quantify membrane surface electrical properties. *Colloids and Surfaces A: Physicochemical and Engineering Aspects*, 201(1-3):73–83, 2002.
- [69] Scott A Bradford and Saeed Torkzaban. Colloid interaction energies for physically and chemically heterogeneous porous media. *Langmuir*, 29(11):3668–3676, 2013.
- [70] R Messina, E González-Tovar, M Lozada-Cassou, and C Holm. Overcharging: The crucial role of excluded volume. 60:383–389, 2002.
- [71] Alexandre P dos Santos, Amin Bakhshandeh, and Yan Levin. Effects of the dielectric discontinuity on the counterion distribution in a colloidal suspension. *The Journal of chemical physics*, 135(4):044124, 2011.

- [72] Leo Lue and Per Linse. Macroion solutions in the cell model studied by field theory and monte carlo simulations. *The Journal of chemical physics*, 135(22):224508, 2011.
- [73] Yufei Jing, Vikram Jadhao, Jos W Zwanikken, and Monica Olvera de la Cruz. Ionic structure in liquids confined by dielectric interfaces. *The Journal of chemical physics*, 143(19):194508, 2015.
- [74] Hanne S Antila and Erik Luijten. Dielectric modulation of ion transport near interfaces. *Physical review letters*, 120(13):135501, 2018.
- [75] Alireza Mashaghi, P Partovi-Azar, Tayebah Jadidi, Nasser Nafari, Philipp Maass, M Reza Rahimi Tabar, Mischa Bonn, and Huib J Bakker. Hydration strongly affects the molecular and electronic structure of membrane phospholipids. 136(11):114709, 2012.
- [76] J P Dilger, S G McLaughlin, T J McIntosh, and S A Simon. The dielectric constant of phospholipid bilayers and the permeability of membranes to ions. 206(4423):1196–1198, 1979.
- [77] Pu Tian. Computational protein design, from single domain soluble proteins to membrane proteins. *Chemical Society Reviews*, 39(6):2071–2082, 2010.
- [78] Zecheng Gan, Huanxin Wu, Kipton Barros, Zhenli Xu, and Erik Luijten. Comparison of efficient techniques for the simulation of dielectric objects in electrolytes. *Journal of Computational Physics*, 291:317–333, 2015.
- [79] Kenneth L Nash. A review of the basic chemistry and recent developments in trivalent f-elements separations. *Solvent Extraction and Ion Exchange*, 11(4):729–768, 1993.
- [80] KL Nash and JC Sullivan. Kinetics of complexation and redox reactions of the lanthanides in aqueous solutions. *Handbook on the Physics and Chemistry of Rare Earths*, 15:347–391, 1991.
- [81] B Weaver. Solvent extraction in the separation of rare earths and trivalent actinides. *Ion Exchange and Solvent Extraction*, 6:189–277, 1974.
- [82] John H Forsberg, Yizhak Marcus, Therald Moeller, Ulrich Krüerke, and Edith Schleitzer-Rust. *Gmelin Handbook of Inorganic Chemistry. Sc, Y, La-Lu-Rare Earth Elements. Pt. D 6. Ion Exchange and Solvent Extraction Reactions, Organometallic Compounds: System-number 39*. Springer, 1983.

- [83] Tatsuya Sekine. Studies of the liquid-liquid partition systems. iii. the solvent extraction of americium (iii) and europium (iii) thiocyanate complexes with tributylphosphate. *Bulletin of the Chemical Society of Japan*, 38(11):1972–1978, 1965.
- [84] Pier Roberto Danesi, Renato Chiarizia, and Charles F Coleman. The kinetics of metal solvent extraction. 1980.
- [85] Geoffroy Ferru, Benjamin Reinhart, Mrinal K Bera, Monica Olvera de la Cruz, Baofu Qiao, and Ross J Ellis. The lanthanide contraction beyond coordination chemistry. *Chemistry—A European Journal*, 22(20):6899–6904, 2016.
- [86] Mark R Antonio, Daniel R McAlister, and E Philip Horwitz. An europium (iii) diglycolamide complex: insights into the coordination chemistry of lanthanides in solvent extraction. *Dalton Transactions*, 44(2):515–521, 2015.
- [87] A Matthew Wilson, Phillip J Bailey, Peter A Tasker, Jennifer R Turkington, Richard A Grant, and Jason B Love. Solvent extraction: the coordination chemistry behind extractive metallurgy. *Chemical society reviews*, 43(1):123–134, 2014.
- [88] Alexander D Braatz, Mark R Antonio, and Mikael Nilsson. Structural study of complexes formed by acidic and neutral organophosphorus reagents. *Dalton Transactions*, 46(4):1194–1206, 2017.
- [89] PR Smirnov and OV Grechin. Coordination of ions in aqueous solutions of erbium chloride from x-ray diffraction data. *Russian Journal of Coordination Chemistry*, 39(9):685–688, 2013.
- [90] Mrinal K Bera and Mark R Antonio. Polynuclear speciation of trivalent cations near the surface of an electrolyte solution. *Langmuir*, 31(19):5432–5439, 2015.
- [91] Mrinal K Bera, Guangming Luo, Mark L Schlossman, L Soderholm, Sungsik Lee, and Mark R Antonio. Erbium (iii) coordination at the surface of an aqueous electrolyte. *The Journal of Physical Chemistry B*, 119(28):8734–8745, 2015.
- [92] Guangming Luo, Wei Bu, Miroslav Mihaylov, Ivan Kuzmenko, Mark L Schlossman, and L Soderholm. X-ray reflectivity reveals a nonmonotonic ion-density profile perpendicular to the surface of ercl<sub>3</sub> aqueous solutions. *The Journal of Physical Chemistry C*, 117(37):19082–19090, 2013.
- [93] Wei Bu, Hao Yu, Guangming Luo, Mrinal K Bera, Binyang Hou, Adam W Schuman, Binhua Lin, Mati Meron, Ivan Kuzmenko, Mark R Antonio, et al. Observation of a rare earth ion–extractant complex arrested at the oil–water interface during solvent extraction. *The Journal of Physical Chemistry B*, 118(36):10662–10674, 2014.

- [94] Wei Bu, Miroslav Mihaylov, Daniel Amoanu, Binhua Lin, Mati Meron, Ivan Kuzmenko, L Soderholm, and Mark L Schlossman. X-ray studies of interfacial strontium–extractant complexes in a model solvent extraction system. *The Journal of Physical Chemistry B*, 118(43):12486–12500, 2014.
- [95] Mitchell Miller, Miaoqi Chu, Binhua Lin, Wei Bu, and Pulak Dutta. Atomic number dependent structural transitions in ordered lanthanide monolayers: Role of the hydration shell. *Langmuir*, 33(6):1412–1418, 2017.
- [96] C Mingotaud, J-P Chauvet, and LK Patterson. Stability of chlorophyll a at the gas-water interface in pure and mixed monolayers. an evaluation of interfacial ph. *The Journal of Physical Chemistry*, 100(47):18554–18561, 1996.
- [97] Alexander Schlaich, Ernst W Knapp, and Roland R Netz. Water dielectric effects in planar confinement. *Physical review letters*, 117(4):048001, 2016.
- [98] Douwe Jan Bonthuis, Stephan Gele, and Roland R Netz. Dielectric profile of interfacial water and its effect on double-layer capacitance. *Physical review letters*, 107(16):166102, 2011.
- [99] Yan Levin, Alexandre P Dos Santos, and Alexandre Diehl. Ions at the air-water interface: an end to a hundred-year-old mystery? *Physical review letters*, 103(25):257802, 2009.
- [100] Guillermo Ivan Guerrero Garcia and Monica Olvera de la Cruz. Polarization effects of dielectric nanoparticles in aqueous charge-asymmetric electrolytes. *The Journal of Physical Chemistry B*, 118(29):8854–8862, 2014.
- [101] Yaohua Li, Martin Girard, Meng Shen, Jaime Andres Millan, and Monica Olvera De La Cruz. Strong attractions and repulsions mediated by monovalent salts. *Proceedings of the National Academy of Sciences*, 114(45):11838–11843, 2017.
- [102] RR Netz. Charge regulation of weak polyelectrolytes at low-and high-dielectric-constant substrates. *Journal of Physics: Condensed Matter*, 15(1):S239, 2002.
- [103] Cheuk-Yui Leung, Liam C Palmer, Bao Fu Qiao, Sumit Kewalramani, Rastko Sknepnek, Christina J Newcomb, Megan A Greenfield, Graziano Vernizzi, Samuel I Stupp, Michael J Bedzyk, et al. Molecular crystallization controlled by ph regulates mesoscopic membrane morphology. *ACS nano*, 6(12):10901–10909, 2012.
- [104] Changrui Gao, Honghao Li, Yue Li, Sumit Kewalramani, Liam C. Palmer, Vinayak P. Dravid, Samuel I. Stupp, Monica Olvera de la Cruz, and Michael J.

- Bedzyk. Electrostatic control of polymorphism in charged amphiphile assemblies.(report). *Journal of Physical Chemistry B*, 121(7):1623–1628, February 2017.
- [105] S Dourdain, I Hofmeister, O Pecheur, JF Dufreche, R Turgis, A Leydier, J Jestin, F Testard, S Pellet-Rostaing, and T Zemb. Synergism by coassembly at the origin of ion selectivity in liquid–liquid extraction. *Langmuir*, 28(31):11319–11328, 2012.
- [106] Michael S Arnold, Mustafa O Guler, Mark C Hersam, and Samuel I Stupp. Encapsulation of carbon nanotubes by self-assembling peptide amphiphiles. *Langmuir*, 21(10):4705–4709, 2005.
- [107] Honggang Cui, Matthew J Webber, and Samuel I Stupp. Self-assembly of peptide amphiphiles: From molecules to nanostructures to biomaterials. *Peptide Science: Original Research on Biomolecules*, 94(1):1–18, 2010.
- [108] Frank Versluis, Hana Robson Marsden, and Alexander Kros. Power struggles in peptide-amphiphile nanostructures. *Chemical Society Reviews*, 39(9):3434–3444, 2010.
- [109] IW Hamley. Self-assembly of amphiphilic peptides. *Soft Matter*, 7(9):4122–4138, 2011.
- [110] Ashkan Dehsorkhi, Valeria Castelletto, and Ian W Hamley. Self-assembling amphiphilic peptides. *Journal of Peptide Science*, 20(7):453–467, 2014.
- [111] John B Matson, R Helen Zha, and Samuel I Stupp. Peptide self-assembly for crafting functional biological materials. *Current Opinion in Solid State and Materials Science*, 15(6):225–235, 2011.
- [112] Shuming Zhang, Megan A Greenfield, Alvaro Mata, Liam C Palmer, Ronit Bitton, Jason R Mantei, Conrado Aparicio, Monica Olvera De La Cruz, and Samuel I Stupp. A self-assembly pathway to aligned monodomain gels. *Nature materials*, 9(7):594, 2010.
- [113] Faifan Tantakitti, Job Boekhoven, Xin Wang, Roman V Kazantsev, Tao Yu, Jiahe Li, Ellen Zhuang, Roya Zandi, Julia H Ortony, Christina J Newcomb, et al. Energy landscapes and functions of supramolecular systems. *Nature materials*, 15(4):469, 2016.
- [114] Juan F Miravet, Beatriu Escuder, Maria Dolores Segarra-Maset, Marta Tena-Solsona, Ian W Hamley, Ashkan Dehsorkhi, and Valeria Castelletto. Self-assembly of a peptide amphiphile: transition from nanotape fibrils to micelles. *Soft Matter*, 9(13):3558–3564, 2013.

- [115] Elia Beniash, Jeffery D Hartgerink, Hannah Storrie, John C Stendahl, and Samuel I Stupp. Self-assembling peptide amphiphile nanofiber matrices for cell entrapment. *Acta biomaterialia*, 1(4):387–397, 2005.
- [116] Yuri S Velichko, Samuel I Stupp, and Monica Olvera De La Cruz. Molecular simulation study of peptide amphiphile self-assembly. *The journal of physical chemistry B*, 112(8):2326–2334, 2008.
- [117] Stefan Tsonchev, Krista L Niece, George C Schatz, Mark A Ratner, and Samuel I Stupp. Phase diagram for assembly of biologically-active peptide amphiphiles. *The Journal of Physical Chemistry B*, 112(2):441–447, 2008.
- [118] Roman V Kazantsev, Adam J Dannenhoffer, Adam S Weingarten, Brian T Phelan, Boris Harutyunyan, Taner Aytun, Ashwin Narayanan, Daniel J Fairfield, Job Boekhoven, Hiroaki Sai, et al. Crystal-phase transitions and photocatalysis in supramolecular scaffolds. *Journal of the American Chemical Society*, 139(17):6120–6127, 2017.
- [119] Atmaram Pawar, C Bothiraja, Karimunnisa Shaikh, and Ashwin Mali. An insight into cochleates, a potential drug delivery system. *RSC Advances*, 5(99):81188–81202, 2015.
- [120] Kalpa Nagarsekar, Mukul Ashtikar, Frank Steiniger, Jana Thamm, Felix Schacher, and Alfred Fahr. Understanding cochleate formation: insights into structural development. *Soft matter*, 12(16):3797–3809, 2016.
- [121] D Papahadjopoulos, WJ Vail, K Jacobson, and G Poste. Cochleate lipid cylinders: formation by fusion of unilamellar lipid vesicles. *Biochimica et Biophysica Acta (BBA)-Biomembranes*, 394(3):483–491, 1975.
- [122] Valeria Castelletto, Ian W Hamley, Javier Perez, Ludmila Abezgauz, and Dganit Danino. Fibrillar superstructure from extended nanotapes formed by a collagen-stimulating peptide. *Chemical Communications*, 46(48):9185–9187, 2010.
- [123] Honggang Cui, Takahiro Muraoka, Andrew G Cheetham, and Samuel I Stupp. Self-assembly of giant peptide nanobelts. *Nano letters*, 9(3):945–951, 2009.
- [124] Honggang Cui, Andrew G Cheetham, E Thomas Pashuck, and Samuel I Stupp. Amino acid sequence in constitutionally isomeric tetrapeptide amphiphiles dictates architecture of one-dimensional nanostructures. *Journal of the American Chemical Society*, 136(35):12461–12468, 2014.

- [125] Eli D Sone, Eugene R Zubarev, and Samuel I Stupp. Semiconductor nanohelices templated by supramolecular ribbons. *Angewandte Chemie International Edition*, 41(10):1705–1709, 2002.
- [126] Zhenwei Yao and Monica Olvera De La Cruz. Electrostatics-driven hierarchical buckling of charged flexible ribbons. *Physical review letters*, 116(14):148101, 2016.
- [127] Jozef Adamcik and Raffaele Mezzenga. Adjustable twisting periodic pitch of amyloid fibrils. *Soft Matter*, 7(11):5437–5443, 2011.
- [128] Adam S Weingarten, Roman V Kazantsev, Liam C Palmer, Mark McClendon, Andrew R Koltonow, Amanda PS Samuel, Derek J Kiebala, Michael R Wasielewski, and Samuel I Stupp. Self-assembling hydrogel scaffolds for photocatalytic hydrogen production. *Nature chemistry*, 6(11):964, 2014.
- [129] Adam S Weingarten, Roman V Kazantsev, Liam C Palmer, Daniel J Fairfield, Andrew R Koltonow, and Samuel I Stupp. Supramolecular packing controls h2 photocatalysis in chromophore amphiphile hydrogels. *Journal of the American Chemical Society*, 137(48):15241–15246, 2015.
- [130] Jessica A. Lehrman, Honggang Cui, Wei-wen Tsai, Tyson J. Moyer, and Samuel I. Stupp. Supramolecular control of self-assembling terthiophenepeptide conjugates through the amino acid side chain. *Chemical Communications*, 48(78):9711–9713, September 2012.
- [131] PierreAlain Monnard and David W. Deamer. Membrane selfassembly processes: Steps toward the first cellular life. *Anatomical Record*, 268(3):196–207, November 2002.
- [132] Alicja J. Dzieciol and Stephen Mann. Designs for life: protocell models in the laboratory, December 2011.
- [133] Vladimir P. Torchilin. Recent advances with liposomes as pharmaceutical carriers. *Nature Reviews Drug Discovery*, 4(2), February 2005.
- [134] Annette Rösler, Guido WM Vandermeulen, and Harm-Anton Klok. Advanced drug delivery devices via self-assembly of amphiphilic block copolymers. *Advanced drug delivery reviews*, 64:270–279, 2012.
- [135] Honghao Li, Aykut Erbas, Jos Zwanikken, and Monica Olvera de la Cruz. Ionic conductivity in polyelectrolyte hydrogels. *Macromolecules*, 49(23):9239–9246, 2016.

- [136] KS Kazanskii and SA Dubrovskii. Chemistry and physics of agricultural hydrogels. In *Polyelectrolytes Hydrogels Chromatographic Materials*, pages 97–133. Springer, 1992.
- [137] Gary M. Eichenbaum, Patrick F. Kiser, Andrey V. Dobrynin, Sidney A. Simon, and David Needham. Investigation of the swelling response and loading of ionic microgels with drugs and proteins: the dependence on cross-link density. *Macromolecules*, 32(15):4867–4878, 1999.
- [138] Toshikazu Ono, Takahiro Sugimoto, Seiji Shinkai, and Kazuki Sada. Lipophilic polyelectrolyte gels as super-absorbent polymers for nonpolar organic solvents. *Nature materials*, 6(6):429–433, 2007.
- [139] H. Brett Schreyer, Nouvelle Gebhart, Kwang J. Kim, and Mohsen Shahinpoor. Electrical activation of artificial muscles containing polyacrylonitrile gel fibers. *Biomacromolecules*, 1(4):642–647, 2000. PMID: 11710194.
- [140] Han Il Kim, Sang Jun Park, Sun I. Kim, Nam Gyun Kim, and Seon Jeong Kim. Electroactive polymer hydrogels composed of polyacrylic acid and poly(vinyl sulfonic acid) copolymer for application of biomaterial. *Synthetic Metals*, 155(3):674 – 676, 2005.
- [141] J P Gong, N Komatsu, T Nitta, and Y Osada. Electrical conductance of polyelectrolyte gels. *The Journal of Physical Chemistry B*, 101(5):740–745, 1997.
- [142] J Travas-Sejdic, R Steiner, J Desilvestro, and P Pickering. Ion conductivity of novel polyelectrolyte gels for secondary lithium-ion polymer batteries. *Electrochimica acta*, 46(10):1461–1466, 2001.
- [143] Maria Forsyth, Jiazeng Sun, F Zhou, and DR MacFarlane. Enhancement of ion dissociation in polyelectrolyte gels. *Electrochimica acta*, 48(14):2129–2136, 2003.
- [144] Bryce E Kidd, Scott J Forbey, Friedrich W Steuber, Robert B Moore, and Louis A Madsen. Multiscale lithium and counterion transport in an electrospun polymer-gel electrolyte. *Macromolecules*, 48(13):4481–4490, 2015.
- [145] P Pissis and A Kyritsis. Electrical conductivity studies in hydrogels. *Solid State Ionics*, 97(1):105–113, 1997.
- [146] Ralph H. Colby, David C. Boris, Wendy E. Krause, and Julia S. Tan. Polyelectrolyte conductivity. *Journal of Polymer Science Part B: Polymer Physics*, 35(17):2951–2960, 1997.

- [147] Gerald S Manning. Limiting laws and counterion condensation in polyelectrolyte solutions i. colligative properties. *The journal of chemical Physics*, 51(3):924–933, 1969.
- [148] Qiliang Yan and Juan J. de Pablo. Monte carlo simulation of a coarse-grained model of polyelectrolyte networks. *Phys. Rev. Lett.*, 91:018301, Jul 2003.
- [149] Steve Plimpton, Roy Pollock, and Mark Stevens. Particle-mesh ewald and rrespa for parallel molecular dynamics simulations. In *PPSC*. Citeseer, 1997.
- [150] Prateek K Jha, Rastko Sknepnek, Guillermo Ivan Guerrero-Garcia, and Monica Olvera de la Cruz. A graphics processing unit implementation of coulomb interaction in molecular dynamics. *Journal of chemical theory and computation*, 6(10):3058–3065, 2010.
- [151] Steve Plimpton. Fast parallel algorithms for short-range molecular dynamics. *Journal of Computational Physics*, 117(1):1 – 19, 1995.
- [152] Philippe H. Hünenberger. *Thermostat Algorithms for Molecular Dynamics Simulations*, pages 105–149. Springer Berlin Heidelberg, Berlin, Heidelberg, 2005.
- [153] Daan Frenkel and Berend Smit. *Understanding molecular simulation: from algorithms to applications*, volume 1. Academic press, 2001.
- [154] Henrik Flyvbjerg and Henrik Gordon Petersen. Error estimates on averages of correlated data. *The Journal of Chemical Physics*, 91(1):461–466, 1989.
- [155] Frederick George Donnan. The theory of membrane equilibria. *Chemical Reviews*, 1(1):73–90, 1924.
- [156] A Katchalsky, S Lifson, and H Exsenberg. Equation of swelling for polyelectrolyte gels. *Journal of Polymer Science*, 7(5):571–574, 1951.
- [157] Jean-Louis Barrat, Jean-François Joanny, and Phil Pincus. On the scattering properties of polyelectrolyte gels. *Journal de Physique II*, 2(8):1531–1544, 1992.
- [158] B. A. Mann, R. Everaers, C. Holm, and K. Kremer. Scaling in polyelectrolyte networks. *Europhys. Lett.*, 67(5):786–792, 2004.
- [159] Aykut Erbaş and Monica Olvera de la Cruz. Energy Conversion in Polyelectrolyte Hydrogels. *ACS Macro Letters*, pages 857–861, August 2015.
- [160] Fumio Oosawa. Polyelectrolytes. In *Polyelectrolytes*. Marcel Dekker, 1971.

- [161] Bernward A. Mann, Christian Holm, and Kurt Kremer. Swelling of polyelectrolyte networks. *The Journal of Chemical Physics*, 122(15):154903, 2005.
- [162] Kai Grass and Christian Holm. Polyelectrolytes in electric fields: measuring the dynamical effective charge and effective friction. *Soft Matter*, 5:2079–2092, 2009.
- [163] Markus Deserno, Christian Holm, and Sylvio May. Fraction of condensed counterions around a charged rod: Comparison of poisson-boltzmann theory and computer simulations. *Macromolecules*, 33(1):199–206, 2000.
- [164] Markus Deserno and Christian Holm. Theory and simulations of rigid polyelectrolytes. *Molecular Physics*, 100(18):2941–2956, 2002.
- [165] R. R. Netz. Nonequilibrium unfolding of polyelectrolyte condensates in electric fields. *Phys. Rev. Lett.*, 90:128104, Mar 2003.
- [166] Jianping Gong and Yoshihito Osada. Presence of electrostatic potential wells in the ionic polymer network. *Chemistry Letters*, 24(6):449–450, 1995.
- [167] Prateek K Jha, Jos W Zwanikken, François A Detcheverry, Juan J de Pablo, and Monica Olvera de la Cruz. Study of volume phase transitions in polymeric nanogels by theoretically informed coarse-grained simulations. *Soft Matter*, 7(13):5965–5975, 2011.
- [168] Sandeep Tyagi, Mehmet Szen, Marcello Sega, Marcia Barbosa, Sofia S. Kantorovich, and Christian Holm. An iterative, fast, linear-scaling method for computing induced charges on arbitrary dielectric boundaries. *The Journal of Chemical Physics*, 132(15), April 2010.
- [169] Zuzanna Siwy, Elizabeth Heins, C. Chad Harrell, Punit Kohli, , and Charles R. Martin\*. Conical-nanotube ion-current rectifiers: the role of surface charge. *Journal of the American Chemical Society*, 126(35):10850–10851, 2004. PMID: 15339163.